UNIVERSITY OF CALIFORNIA, SAN DIEGO

Dynamics of Gas-Phase Transient Species Studied by Dissociative Photodetachment of Molecular Anions

A dissertation submitted in partial satisfaction of the

requirement for the degree Doctor of Philosophy

in

Chemistry

by

Zhou Lu

Committee in Charge:

Professor Robert E. Continetti, Chair
Professor Seth Cohen
Professor Amitabha Sinha
Professor Clifford Surko
Professor Peter Wolynes

2007

The dissertation of Zhou Lu is approved, and it is acceptable in quality and for publication on microfilm:

_____

_____

_____

_____

_____

Chair

University of California, San Diego

2007

To my parents, Qinhua and Haodong.

TABLE OF CONTENTS

LIST OF FIGURES

LIST OF TABLES

ACKNOWLEDGEMENTS

First I would like to thank Professor Continetti for being a great advisor and giving me all the opportunities. This thesis work would not have been done without his insightful advice and constant support. I especially appreciate his extreme patience with me. Six years of working with him are really my lifetime fortune. My gratitude to him is beyond the words.

It is my pleasure to work with so many talented scientists in this lab. Dr. Leah Alconcel was the first who showed me how to run "machine A". Dr. Todd Clements was the master of computer coding. Even years after his graduation, I still benefit everyday from the numerous IDL routines written by Todd. Dr. Chris Laperle had worked on every machine in the lab and I learned a lot from him about trouble-shooting of the experimental apparatus as well as mechanical designing.

I would like to take this opportunity to thank the whole "machine A" team that I have worked with. Dr. Shane Bowen shared the machine with me for three years and taught me a lot about laser. Kevin Early and Katie Sanchez were the main team to install the 8000 l/s diffusion pump for the source region. Dr. Qichi Hu and Jonathan Oakman joined the "machine A" team when I was collecting the HOCO/DOCO data and took some shifts for me when I was running overnight experiments. Jonathan also helped make several figures that are used in Chapter 6.

I would also like to thank other members in the lab: Jenny Mann, John Savee, Silvia DeDea, and Chirs Johnson. I wish them success in the graduate school. The special acknowledgement should be given to our permanent visiting scientist, Dr. Morton

Fineman, who invested a lot of time and effort to read my manuscripts and discuss scientific questions with me. I sincerely appreciate his help.

I must thank my family. My parents are willing to do anything they can to provide the best education to me. Without their support, it would have been impossible for me to come across the Pacific Ocean for graduate school. Finally and most importantly, I am very grateful for my lovely wife Yimin, who kept encouraging me and being the source of my strength no matter how busy she was with her own graduate study. I would like to share this important moment with her.

Chapter Three, in full, is a reproduction of the material as it appears in Z. Lu and R.E. Continetti, "Dynamics of the Acetyloxyl Radical Studied by Dissociative Photodetachment of the Acetate Anion," J. Phys. Chem. A **108**, 9962-9969 (2004). Copyright 2004 American Chemical Society. The dissertation author was the investigator for this paper.

Chapter Four, in full, is a reproduction of the material as it appears in Z. Lu, Q. Hu, J.E. Oakman and R.E. Continetti, "Dynamics on the HOCO potential energy surface studied by dissociative photodetachment of $HOCO^-$ and $DOCO^-$," J. Chem. Phys. **126**, 194305-1 − 11 (2007). Copyright 2007 American Institute of Physics. The dissertation author was the investigator for this paper

Chapter Five, in full, is a reproduction of the material as it appears in Z. Lu and R.E. Continetti, "Alignment of a molecular anion via a shape resonance in near-threshold photodetachment," Phys. Rev. Lett. in press (2007). Copyright 2007 American Physical Society. The dissertation author was the investigator for this paper.

VITA

1978	Born, Changshu, China
2001	B.S. in chemistry,
	University of Science and Technology of China
2002	Teaching Assistant, Department of Chemistry and Biochemistry,
	University of California, San Diego
2001 – 2007	Research Assistant, Department of Chemistry and Biochemistry,
	University of California, San Diego
2003	M.S. in chemistry, University of California, San Diego
2007	Ph.D. in chemistry, University of California, San Diego

PUBLICATIONS

Z. Lu and R.E. Continetti, "Alignment of a molecular anion via a shape resonance in Near-threshold photodetachment," Phys. Rev. Lett. in press (2007).

Z. Lu, Q. Hu, J.E. Oakman and R.E. Continetti, "Dynamics on the HOCO potential energy surface studied by dissociative photodetachment of $HOCO^-$ and $DOCO^-$," J. Chem. Phys. **126**, 194305-1 − 11 (2007).

Z. Lu and R.E. Continetti, "Dynamics of the Acetyloxyl Radical Studied by Dissociative Photodetachment of the Acetate Anion," J. Phys. Chem. A **108**, 9962-9969 (2004).

FIELD OF STUDY

Major Field: Chemistry

Studies in Physical Chemistry
Professor Robert E. Continetti

ABSTRACT OF THE DISSERTATION

Dynamics of Gas-Phase Transient Species Studied by Dissociative Photodetachment of Molecular Anions

by

Zhou Lu

Doctor of Philosophy in Chemistry

University of California, San Diego, 2007

Professor Robert E. Continetti, Chair

Gas-phase transient species, such as the CH_3CO_2 and HOCO free radicals, play important roles in combustion and environment chemistry. In this thesis work, the dynamics of these two radicals were studied by dissociative photodetachment (DPD) of the negative ions, $CH_3CO_2^-$ and $HOCO^-$, respectively. The experiments were carried out with a fast-ion-beam photoelectron-photofragment coincidence (PPC) spectrometer. Mass-selected molecular anions in a fast ion beam were intercepted by a linearly polarized laser pulse. Three dimensional velocities of the resulting photoelectron and photofragments were measured in coincidence by time- and position-sensitive detectors, providing complete kinematic descriptions of the DPD dynamics.

The energetics and dynamics of CH_3CO_2 were studied by the DPD of acetate anion at photon energy of E_{hv} = 3.49 eV and 4.82 eV. Evidence for several low-lying electronic states of the $CH_3CO_2\cdot$ radical were observed. While a stable CH_3CO_2 channel

(~10%) was found, most CH_3CO_2 radicals (~90%) lead to a dissociation channel forming CH_3 + CO_2 products with ~72% of the available energy partitioned into translational degrees of freedom at $E_{h\nu}$ = 3.49 eV.

The potential energy surface of HOCO and the dynamics of the OH + CO $\rightarrow$ H + CO_2 reaction were explored by DPD of $HOCO^-$ and $DOCO^-$ at a photon energy of $E_{h\nu}$ = 3.21 eV. The PPC experiments allow the identification of photodetachment processes leading to the production of stable HOCO free radicals and both the H + CO_2 and OH + CO dissociation channels. The PPC spectra and branching ratio analysis are consistent with a role for a tunneling mechanism in the production of H + CO_2. Evidence was also shown that vibrationally excited $HOCO^-$ anions play a role in the observed DPD process.

The near-threshold one- and two-photon photodetachment dynamics of $HOCO^-$ at $E_{h\nu}$ = 1.60 eV was also studied. An anisotropic photoelectron angular distribution (PAD) consistent with a strong molecular alignment was observed in the two-photon process. A quantitative analysis of the PAD reveals this is associated with a temporary anion formed by a *p*-wave shape resonance and the PAD in the two-photon signal is a result of interfering *s*- and *d*-partial waves within the atomic approximation.

Finally, the photoelectron-photofragment angular correlations in the one- and two-photon DPD of $HOCO^-$ and $DOCO^-$ were investigated. The results show a transition dipole in the plane of symmetry for the DPD of $HOCO^-$. The HOCO and DOCO lifetimes were examined as a function of the orientation of transition dipole and were estimated to be less than 9×10^{-13} sec and 1.3×10^{-12} sec, respectively. Measurement of the two-photon photofragment angular distribution in the OH + CO channel confirmed the alignment of $HOCO^-$ inferred from the two-photon PADs.

Chapter 1

Introduction

Ever since the birth of the modern chemistry, the desire to pursue a detailed understanding of the dynamical course of chemical transformations has never diminished for chemists. All chemical reactions, no matter whether they are initiated by molecular collisions or the interaction with electromagnetic radiation, and no matter whether their final products are simply the isomers of the reagents or have completely new chemical constituents, are essentially rearrangements of the molecular structure driven by energy redistribution on the reactive potential energy surfaces (PES). Therefore, a comprehensive picture of a chemical reaction not only describes the structural and energetic information of the reactants and products, but also shows how the molecular properties change during the course of the reaction.[1]

During the last century, the field of chemical kinetics and dynamics witnessed remarkable revolutions following the advent of quantum mechanics and a number of new techniques such as fast computers, ultrahigh vacuum, powerful lasers, and modern spectroscopy. As a result, knowledge of chemical reactions has reached the microscopic and quantum level, [2,3] with the recognition that even the simplest macroscopic chemical reactions consists of a series of elementary processes[4] and that a wide range of reactive intermediates may play important roles in the determination of the reaction rates, the energy partitioning among the degrees of freedom of the products, product angular distributions, and the branching ratios of the competing reaction channels. [2-10] Such

reactive intermediates, including free radicals and transition states, are collectively called transient species.

The investigation of transient species has both scientific and practical significance. In addition to providing information about the reaction mechanisms, characterization of the structure, energetics, and decay dynamics of the transient species benefit those who want to manipulate the rate of a certain reaction, to control the product branching ratios, and/or to harness the energy released from a chemical process.

This thesis focuses on the dynamics and energetics of two important gas-phase transient species in combustion and atmospheric chemistry, the HOCO and CH_3CO_2 free radicals. These free radicals are optically prepared by the photodetachment of corresponding anion precursors, $HOCO^-$ and $CH_3CO_2^-$, using linearly polarized laser pulses. The technique of photoelectron-photofragment coincidence (PPC) spectroscopy was applied in these experiments. The observed photoelectron spectra reveal how nascent neutral HOCO and CH_3CO_2 potential energy surfaces are populated by photoejection of the excess electron from the negative ions, while measurement of the photofragment translational energy *in coincidence* elucidates the subsequent dissociation dynamics of the energy-selected HOCO and CH_3CO_2 free radicals. In addition to a full kinematic description of energy partitioning, our detection method also allows the measurement of the photoelectron and photofragment angular distributions in coincidence, yielding valuable information such as the life-time of nascent transient species before fragmentation and the nature of the photodetachment dynamics.

In this chapter, the roles played by gas-phase transient species in combustion and atmospheric chemistry will be briefly reviewed, with an emphasis on the HOCO and

CH_3CO_2 free radicals. The following section will describe how the dynamics and PES of transient species can be studied by the photodetachment of negative ions and will compare this approach with other experimental methods. General discussions of photoelectron-photofragment coincidence spectroscopy and angular correlations will then be presented. Finally in the conclusion of this chapter, the remainder of this thesis will be outlined.

1.1 Transient Species in Combustion and Atmospheric Chemistry

At a fundamental level, combustion is the process of exothermic oxidation. Numerous chemical kinetics studies have revealed that a seemingly simple combustion processes such as $H_2 + O_2$ often involves a chain of elementary reactions, including chain initiation, branching, propagation, and termination.[11] To achieve a full understanding of a combustion process, knowledge about each of these individual elementary steps, such as the rate constants, and temperature/pressure-dependence of the reactivity, is required.[12] The study of the dynamics of reactive intermediates will help reveal the mechanisms that determine these important chemical properties, and consequently have practical importance. For example, since the stability of transient species is related to the activation energy, the relevant information about transient species may assist one to determine appropriate reaction conditions, such as temperature, pressure, and the concentrations of fuel mixtures, to improve the efficiency of combustion.

One of the transient species investigated in this thesis is the HOCO free radical, an intermediate that plays an essential role in hydrocarbon combustion. In the presence of sufficient oxygen, burning hydrocarbons will finally convert into carbon dioxide and

water. During this process, one of the most important elementary reactions is that between hydroxyl radical and carbon monoxide:[11,12]

$$OH + CO \rightarrow [HOCO]^* \rightarrow H + CO_2, \quad (1\text{-}1)$$

In this reaction, the HOCO radical is bound intermediate. This reaction is considered as the nearly exclusive source of CO_2 production in combustion.[11] In addition, the enthalpy change of -1.05 eV (-24.1 kcal/mol) at 0 K calculated from the available thermodynamic data,[13] indicates the significant contribution of this elementary reaction to the heat released during hydrocarbon combustion.

A large number of experimental and theoretical studies have been carried out for reaction (1-1). It has been reported that the HOCO PES has a deep potential well and a high-energy transition state leading to the $H + CO_2$ products, while the OH + CO reaction forming the HOCO free radical only experience a negligible barrier.[14-17] A consequence of this PES shape is that after the formation of HOCO transient species, there exist three competing product channels, the forward direction forming $H + CO_2$, the decomposition of HOCO back to the entrance channel OH + CO, and the relaxation of excited HOCO radical by colliding with a third body to form stable HOCO species trapped in the potential well. The fate of the HOCO transient species thus plays an important role in the energy released in the combustion.

The reactive HOCO intermediate also takes part in several important chemical cycles in the atmosphere.[18] As mentioned above, the dissociation of HOCO into $H + CO_2$ is the dominant source of carbon dioxide in hydrocarbon combustion and therefore is related to global warming. In addition, the reaction (1-1) also serves as one of the major sinks of hydroxyl radicals in the troposphere, and as a result indirectly affects the ozone

concentrations in the stratosphere.[18] Some chemists also believe this reaction directly participates in smog-related formation and destruction processes of atmospheric ozone.[19] In summary, in addition to its importance in providing energy during hydrocarbon combustion, the HOCO transient species also has a significant environmental impact through atmospheric oxidation processes.

In addition to the HOCO radical, this thesis also investigates the dynamics and energetics of another gas-phase transient species, the CH_3CO_2 free radical. As a typical member in the carboxyl radical family, CH_3CO_2, the acetyloxyl radical, is a possible intermediate of the bimolecular reaction:[20,21]

$$CH_3O + CO \rightarrow CH_3 + CO_2. \quad (1\text{-}2)$$

It is straightforward to see that this reaction is analogous to reaction (1-1) involving HOCO, with the substitution of the methyl radical, CH_3, for the H atom. It may also be involved in the atmospheric reaction of acetylperoxy radical $CH_3CO{\cdot}O_2$: [18]

$$CH_3CO{\cdot}O_2 + NO \rightarrow CH_3CO{\cdot}O + NO_2 \quad (1\text{-}3)$$

$$CH_3CO{\cdot}O \rightarrow CH_3 + CO_2 \quad (1\text{-}4)$$

Further background on the CH_3CO_2 and HOCO radicals will be presented in the Chapters 3 and 4, respectively.

1.2 Using Negative Ions to Study Transient species

The spectroscopic characterization of a highly reactive and short-lived transient species is a significant challenge for the experimentalist. Given the example of the HOCO radical, collision of OH + CO, in the normal 'entrance channel' for this reaction, generates highly excited HOCO intermediates that can decompose rapidly. One approach

to this problem is to trap reactive intermediates in cryogenic matrices. In such experiments, free radical reactions are usually initiated by photolysis or electric discharge, generating reactive transient species that will be further isolated and stabilized in an inert rare gas matrix. Conventional infrared or microwave spectroscopy is often employed to study the vibrational and rotational structures of the trapped transient species.[22-24]

Several other experimental methods are available for studying the dynamics of gas-phase transient species. With the emergence of ultrafast lasers, it is now possible to take "snap-shots" of transient species in gas phase.[25] Typically, the transient species of interest is prepared by photoexcitation or photodissociation of a stable precursor molecule, e.g., a van de Waals complex, by a pump laser. A probe laser pulse fired at a time delay after the pump laser is then used to excite or ionize one of the dissociation fragments. The dynamical course of bond breaking is recorded by scanning delay time between the pump and probe lasers and measuring the time-evolution of laser-induced-fluorescence (LIF) intensity, photoelectron/photoion yields, or photoelectron kinetic energy.[25-28] More recently, a new time-resolved technique called ultrafast electron diffraction has emerged. In this approach, the probe laser is replaced by an ultrafast electron pulse. By measuring the temporal change of the electron diffraction pattern, the geometry of the transient species during a reaction can be directly probed.[29,30]

The dynamics of a reaction intermediate can also be studied by the energy and angular distributions of the final products. Benefiting from the advances in laser techniques, one now can select well-defined quantum states of bimolecular or unimolecular reactants, while the product states can be measured precisely by translational or optical spectroscopy, making the exploration of state-to-state dynamics

possible. These results then can be compared with theoretical predictions of the reaction dynamics to reveal the behavior of transient species that causes the experimental observations. This asymptotic approach, however, only provides indirect examination of the transient species. [2,3,31]

In this thesis, dissociative photodetachment of negative ions is used to probe the dynamics of reactive intermediates. When a neutral molecule or free radical combines with one electron to form a negative ion, the system energy will usually be lowered. The energy released during the electron attachment is called electron affinity (EA). As a result, in contrast to the high reactivity and the consequent short lifetime of a transient neutral species, the negative ions are often more stable than their neutral counterparts. As a result of this, a number of unstable transient species can be generated by photoejection of the excess election from the corresponding negative ion if the photon is sufficiently energetic and a non-zero Franck-Condon overlap exists between the negative ion and the neutral species. This approach has been widely used as a unique and powerful method to prepare gas-phase transient species in the past few decades.[32-36]

Besides the ease of producing transient neutral species, anion photodetachment has several other advantages. One is that because the spin quantum number of electron is ½, the photoejection of an electron makes it possible to access optically forbidden electronic states of neutral transient species. An example of this is the observation of several low-lying singlet and triplet states of neutral O_3 in the photodetachment of doublet ground state O_3^-.[37] Additionally, the molecular geometry of a negative ion may differ from that of the neutral counterpart. Therefore if the photon energy is large enough, the Franck-Condon overlap between the anion and neutral may place the nascent neutral

species at a geometry away from its local energetic minimum, allowing the exploration of internally excited states of the neutral transient species.

The energetics of neutral transient species can be characterized in different ways in photodetachment experiments. With a tunable laser, one can record the cross section for photon absorption as an action spectrum by recording photoelectron, neutral photofragment or photoion yields as a function of the laser wavelength, obtaining the resonant transition energy between the anion and neutral species.[38] Alternatively, photoelectron spectroscopy measures the photoelectron kinetic energy (eKE) at a given laser wavelength. The second approach has been widely used in the study of photoionization and photodetachment dynamics, providing rich chemical information, e.g., electron affinities or ionization potentials, and electronic and vibrational structures of ions and neutral molecules.[38-41] Recently, photoelectron spectroscopy combined with anion photodetachment has been extended to study the transition states of the bimolecular reactions or isomerization processes.[32,35,36]

The shape of a photoelectron spectrum depends on the nature of the photodetachment process. Figure 1-1 shows three categories of simple photodetachment in the diatomic limit, sorted by the PES of electronic states of the nascent neutral products. When photodetachment generates a stable neutral molecule in a bound state as illustrated in Figure 1-1 (a):

$$AB^- + h\nu \rightarrow AB + e^-, \tag{1-5}$$

the eKE distribution is expected to exhibit resolved structures corresponding to the vibrational states of the neutral products. The relative intensity of each eKE peak is determined by the Franck-Condon overlap between the initial anion state and final neutral

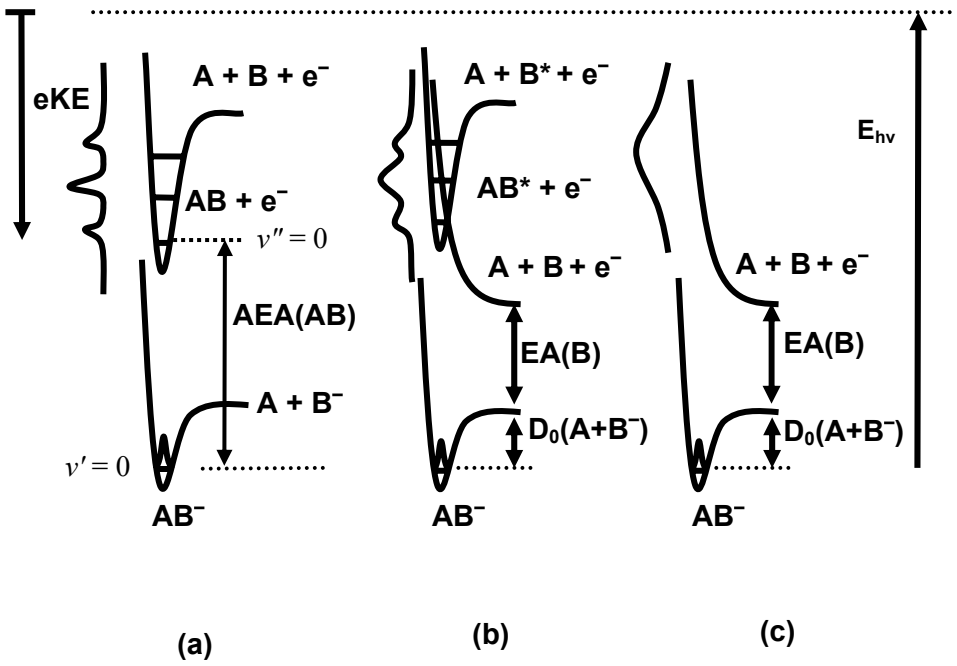

Figure 1-1: Schematic potential energy surfaces and photoelectron spectra of photodetachment under the diatomic limit. The photons interact with the vibrational ground states of diatomic anions, eject the photoelectrons, and place the resulting neutral species on one of three types of potential energy surfaces: (a) a stable bound state of a neutral molecule, (b) a bound state crossed with a repulsive potential, and (c) a purely repulsive neutral potential.

PES. From the photoelectron spectra, one can obtain the vertical detachment energies (VDE) by:

$$E_{hv} = eKE + VDE, \tag{1-6}$$

while the VDE is related to AEA by:

$$VDE = AEA + E_{int}(neutral) - E_{int}(anion). \tag{1-7}$$

Here E_{int}(neutral) and E_{int}(anion) represent the internal energies of neutral and anion with respect to their own ground states.

In Figure 1-1 (b), the bound neutral AB state is crossed by a repulsive potential that leads to dissociations into the fragments A and B:

$$AB^- + h\nu \rightarrow AB^* + e^- \rightarrow A + B + e^-. \quad (1\text{-}8)$$

This type of dissociative photodetachment (DPD) process proceeds by predissociation of the excited neutral, and is an *indirect* DPD. In this case, because the nascent neutral species has a finite lifetime, the resulting photoelectron spectrum will have broader peaks compared with the case in Figure 1-1 (a). Nevertheless, the eKE distribution can still be resolved if the metastable transient species has a sufficiently long lifetime.

The third type of photodetachment process is called *direct* DPD, defined by a purely repulsive PES of the nascent neutral product as illustrated in Figure 1-1 (c):

$$AB^- + h\nu \rightarrow A + B + e^-. \quad (1\text{-}9)$$

Since fragmentation of the AB molecule occurs instantaneously, the resulting eKE distribution is a featureless broad peak.

Actual photodetachment experiments can be much more complicated than the simple examples as shown in Figure 1-1, especially for those direct or indirect DPD experiments targeting polyatomic transient species. Equations (1-5), (1-8) and (1-9) can still be used to describe general categories of photodetachment processes of polyatomic anions, except that now one or both of the products A and B may consist of more than one atom. Such complications bring both advantages and disadvantages to photoelectron spectroscopy studies of DPD processes. For instance, only one vibrational mode, the stretching along the bond dissociation direction, is involved in the DPD of diatomic anions. However, in the DPD of a polyatomic anion, there will be 3N-6 for the nonlinear and 3N-5 normal vibrational modes for the linear molecule. Therefore, even for a direct

DPD, a resolved photoelectron spectrum may still be obtained to provide the vibrational frequencies of these normal modes perpendicular to the reaction coordinate.[42,43] But the larger number of degrees of freedom among which the internal energy can be partitioned, the greater possibility that the eKE peaks will be entangled together to generate a photoelectron spectrum lacking resolved structure. In addition, sometimes it is difficult to prepare vibrationally "cold" anion precursors, leading to "hot bands" that reduce the spectral resolution and complicates the assignment of the spectrum. On the other hand, if the instrumental resolution is good enough, the "hot bands" can be used to help characterize the vibrational structure of the parent anions.

Photoelectron spectroscopy examines the energetics of nascent neutral transient species generated by the photodetachment. In a DPD process described by Figure 1-1 (b) and (c), the neutral species will dissociate into the photofragments A and B, releasing a certain amount of kinetic energy. For a diatomic DPD process, the internal energy released during bond breaking will be partitioned solely into electronic and translational degrees of freedom of A and B in the way governed by energy and momentum conservation and the dynamics. For DPD of a polyatomic molecule, the available energy can also be deposited into vibrations and rotations of the photofragments. Therefore the kinetic energy release (KER) among the photofragments will yield complementary information to photoelectron spectroscopy, revealing the ultimate fate of the transient species. [44-46]

The measurement of the photofragment KER has been widely used in the study of molecular photodissociation. In most experiments, one of the neutral photofragments is ionized by electron impact or using the laser-based resonant-multi-photon-ionization

(REMPI) technique, followed by the measurement of its mass and velocities using a time-of-flight, or more recently, a two-dimensional imaging detector.[47-52] The velocities and translational energy of the other photofragment are then calculated by the conservation of linear momentum with the assumption of an infinitely small laser-molecule interaction region. Fast-beam techniques to examine photodissociation and charge-exchange processes in simple molecules by coincidence detection of the photofragments were pioneered by Los and co-workers.[53] More recently, Neumark and coworkers developed a fast beam translational spectrometer for neutral free radicals that uses a two-photon scheme. Using the first laser pulse, a state-selected neutral is prepared by photodetachment of the parent negative ion near threshold in a fast (keV) ion beam. The resulting fast beam of free radicals is then intercepted by a second laser pulse, leading to photodissociation. The pair of photofragments recoils within a small solid angle along the original fast ion beam in the laboratory frame and impinges on the microchannel plate-based time- and position-sensitive detector.[54,55] In this approach, the three-dimensional velocities of both photofragments are measured in coincidence and there is no necessity to ionize the neutral fragments for the detection. The next section of this chapter describes how this technique is combined with the photoelectron spectroscopy to efficiently study the dynamics of gas-phase transient species through the DPD of negative ions.

1.3 Photoelectron-Photofragment Coincidence Spectroscopy

The above discussions have demonstrated that photoelectron spectroscopy and fast-beam photofragment translational spectroscopy are suitable techniques to study the

DPD dynamics and the involved transient species. An even more powerful tool is to measure the correlation of photoelectron and photofragment translational energy partitioning, which requires detection in coincidence of the photoelectron and all of the neutral photofragments produced in a single DPD event. This technique, analogous to photoelectron-photoion coincidence (PEPICO) studies of dissociative photoionization,[56,57] is called photoelectron-photofragment coincidence (PPC) spectroscopy.

The experiments presented in this thesis were conducted with a fast-ion-beam photoelectron-photofragment coincidence spectrometer designed and constructed in our laboratory.[33,34,45,58] Although a number of modifications have been made in recent years, the basic ideas of the experiments have remained unchanged. A fast beam of negative ions are mass-selected by time-of-flight (TOF) and perpendicularly intercepted by a laser pulse. An electron is ejected from the negative ion, forming the neutral transient species of interest that can either remain as a stable free radical or further dissociate. Since the mass of the electron is negligible compared with a molecule and the original beam energy is far larger than the translational energy partitioned into the photoelectron and neutral photofragments during photodetachment, the stable or dissociated neutral species will carry the majority of the linear momentum of the fast ion beam and will be efficiently registered by the microchannel-plate photofragment detector. Both the photoelectron and photofragment detectors used in this research are time- and position-sensitive, allowing direct measurements of three dimensional velocity distributions. Conservation of linear momentum is used to determine the mass ratio and center-of-mass KER partitioning between the neutral photofragment pair. Most importantly, the experiment is run in an

event-wise fashion, allowing the measurement of photoelectron and photofragments in coincidence, providing a complete kinematic description of the DPD dynamics.[59,60]

To carry out a successful PPC measurement, several technical problems have to be considered. In general, a high data acquisition count rate is desired to obtain statistically significant data within a reasonable time, as the detection efficiency for each particle is limited (≈ 50%). However, the count rate per laser shot must be limited. Occurrence of more than one DPD event per laser shot may result in the photoelectron and photofragments arising from two different DPD events being detected in a false coincidence. Therefore one has to make a compromise to maintain a reasonable data collection rate and a low false coincidence level at the same time.[33] To solve this problem, a high-repetition rate of the photodetachment laser (1 kHz in this thesis work) and fast-responding electronics are used in our experimental set-up. Furthermore, a space-focusing assembly is employed to collect the full 4π solid angle of photoelectrons, and the ion beam is accelerated up to 10 keV to improve the detector acceptance of the neutral photofragment with light mass.[61,62] On the other hand, the photodetachment event rate was typically limited to less than 0.1 event per laser shot and examination of linear momentum conservation of the photofragments is employed during data analysis to eliminate most false coincidences.[33]

A PPC spectrum records the scalar correlation of photoelectron and photofragment kinetic energies in a two-dimensional histogram where the intensity of each point represents the number of events corresponding to a given eKE and KER value.[59] Figure 1-2 shows the schematics of an indirect DPD of a diatomic anion and a resulting PPC spectrum. In this case, the eKE and KER are correlated by:

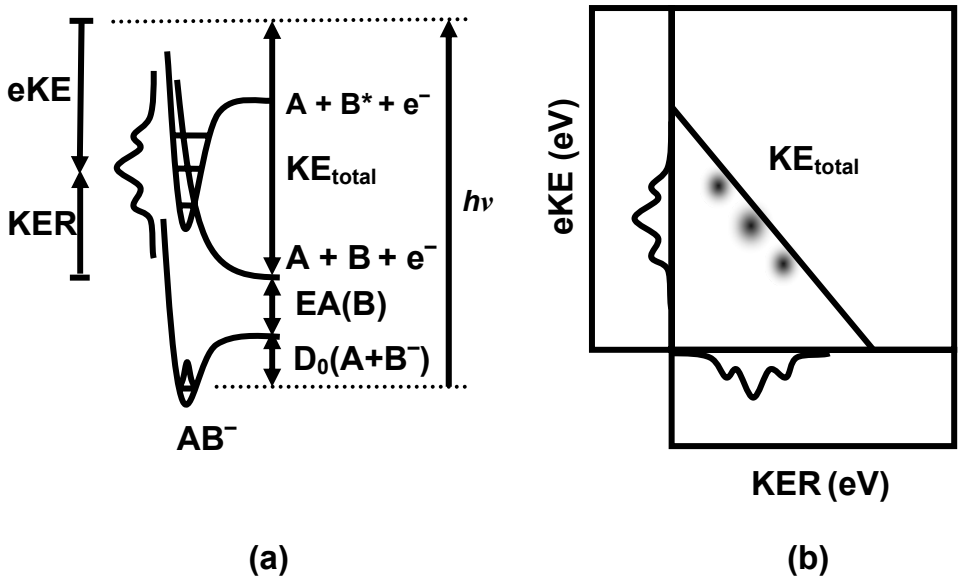

Figure 1-2: Schematics of (a) the potential energy surface, and (b) the photoelectron-photofragment coincidence spectrum for an indirect dissociative photodetachment of a diatomic anion AB^-, assuming only ground electronic state atoms A and B are produced.

$$E_{hv} + E_{int}(AB^-) = eKE + KER + D_0(A\text{-}B^-) + EA\ (B) \qquad (1\text{-}10)$$

where $D_0(A\text{-}B^-)$ is the dissociation energy of AB^- forming A and B^-, and it is assumed that no excited atomic electronic states are available. In Figure 1-2, we further assume that AB^- is in the rotational and vibrational ground state. Since all the AB* species end up as A and B atoms, each vibrational state in AB* that is accessed by the photodetachment corresponds to a specific eKE and KER. The total kinetic energy partitioned into the photoelectron and photofragments, defined by KE_{total} = eKE + KER, is a constant and can be described by a diagonal line in the PPC spectra.

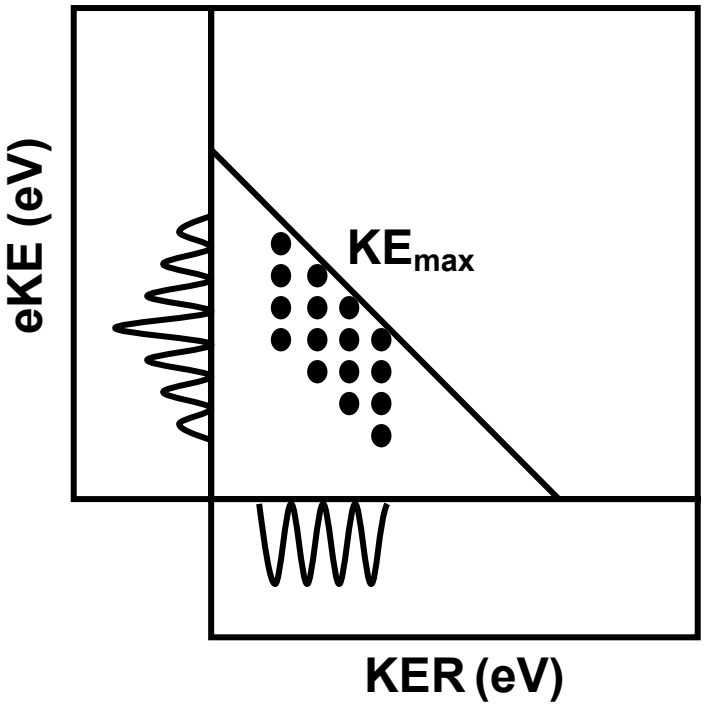

Figure 1-3: Schematic photoelectron-photofragment coincidence spectrum for an indirect dissociative photodetachment of a polyatomic anion. In this case it is assumed that vibrational spacing in the nascent neutral is similar to the vibrational spacing in one of the neutral products, as seen in an earlier study of HCO_2^-.[46]

In the case of indirect DPD of a polyatomic anion, the correlation between the eKE and KER is more complicated because at least one of the final photofragments, A and B, can be internally (vibrationally, rotationally or electronically) excited:

$$E_{h\nu} + E_{int}(AB^-) = eKE + KER + D_0(A\text{-}B^-) + EA\ (B) + E_{int}(A) + E_{int}(B) \qquad (1\text{-}11)$$

If the resolution is good enough, the resulting PPC spectrum will have a form as shown in Figure 1-3, enabling the measurement of state-to-state dynamics from the neutral

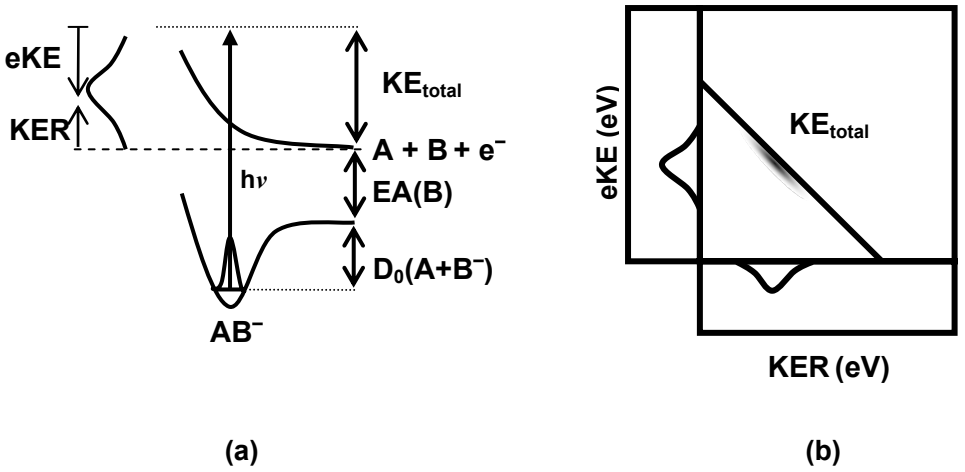

Figure 1-4: Schematics of (a) the potential energy surface, and (b) the photoelectron-photofragment coincidence spectrum for a direct dissociative photodetachment of a diatomic anion AB^-.

transient species to the final dissociation fragments. In this case, the KE_{total} is no longer a constant. Instead, each set of $E_{int}(A) + E_{int}(B)$ will correspond to a specific KE_{total} value that can be represented by a separate diagonal line in the PPC spectra. One very important term in PPC spectroscopy is KE_{max}, defined as the maximum of KE_{total} as shown in Figure 1-3 and can be calculated by the following equation:

$$KE_{max} = E_{h\nu} - D_0(A\text{-}B^-) + EA\ (B) \qquad (1\text{-}12)$$

with the assumption of $E_{int}(AB^-) = 0$.

PPC spectroscopy can also be used to study the dynamics of a direct DPD process as demonstrated in Figure 1-4 (a). Figure 1-4 (b) shows such a PPC spectrum for the diatomic limit. Because of the nature of the repulsive potential, the nascent neutral

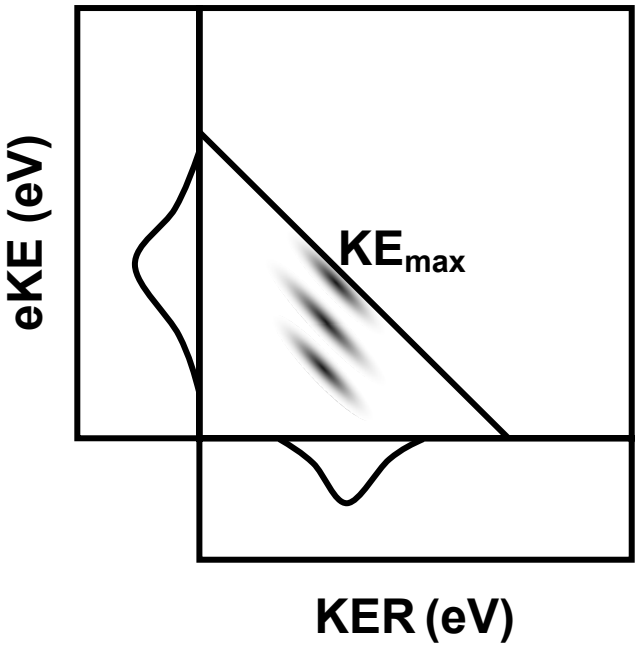

Figure 1-5: Schematic photoelectron-photofragment coincidence spectrum for direct dissociative photodetachment of a polyatomic anion.

species formed by photodetachment will quickly dissociate into the fragments A and B, resulting in broad distributions in the PPC spectra. The equation (1-10) is still valid for the direct DPD of a diatomic anion.

Similarly, the direct DPD of a polyatomic anion will result in a less resolved PPC spectrum compared with the indirect DPD case. However, unlike the diatomic case, in the polyatomic anion photodetachment, the energy of the final neutral products can be distributed among a range of product states that correspond to a set of $KE_{total.}$ values. The resulted PPC spectra can have diagonal structures as shown in Figure 1-5, most clearly

seen in studies of the DPD of O_4^-.[63,64] The equations (1-11) and (1-12) are also valid for the direct DPD process of polyatomic anions.

In addition to providing a complete kinematic picture of a single-channel DPD process as discussed above, in the case of a multi-channel photodetachment process, the coincidence detection method may resolve the contributions from different DPD channels as well as the photoelectron spectra in coincidence with the undissociated neutral product.[62,65] Therefore, for a reactive intermediate [ABC]* involved in the bimolecular reaction,

$$AB + C \leftrightarrow [ABC]^* \leftrightarrow A + BC, \qquad (1\text{-}13)$$

the photodetachment of the negative ion $[ABC]^-$ and the PPC spectroscopy are ideal approaches to unravel the reaction dynamics:

$$\begin{array}{c} [ABC]^- + h\nu \\ \downarrow \\ AB + C + e^- \leftarrow [ABC]^* + e^- \rightarrow A + BC + e^-. \end{array} \qquad (1\text{-}14)$$

The studies of the $HOCO^-$ and $CH_3CO_2^-$ anions that are the focus of much of this thesis are an example of this type of multi-channel DPD process.

1.4 Photoelectron-Photofragment Angular Correlations

In addition to the scalar energetic correlations discussed above, rich information on the DPD dynamics is contained in the product (photoelectron and photofragment) angular correlations. In laser photodetachment experiments, the photoelectron and photofragment angular distributions can provide new insights into the transient species and the dynamics of the DPD process that are complementary to measurements in the

kinetic energy domain. The photoelectron angular distribution (PAD) can be interpreted as the interference of partial waves of outgoing electrons, which in turn is dictated by the nature of the dipole transitions during the photodetachment process and the interactions between the departing electron and neutral molecular core.[66-68] The photofragment angular distributions, on the other hand, can be a measure of the DPD dynamics using the molecular rotations as a "clock".[69] Traditionally, angular distributions of the photoelectron and photofragments are measured in the laboratory frame (LF). However, a great portion of the dynamics information is lost in the measurement of LF-PAD owing to averaging effect by the randomly oriented negative ions before the photodetachment. In the case of direct DPD, or a rapid indirect process, where the atomic framework breaks up promptly on the time scale of molecular rotation, molecular or recoil-frame (MF or RF)-PADs can be recorded since the product recoil direction encodes the location of the recoil axis at the moment of photoabsorption in the case of diatomic or polyatomic anions, respectively. In the case of DPD processes, this was first demonstrated in the study of O_4^- reported in 1996.[63]

In this thesis work, both the photoelectron and photofragments are recorded by time- and position-sensitive imaging detector, directly yielding the three-dimensional velocities for the photoelectron and neutral photofragments. Therefore the angular distributions of the photoelectron and photofragments are straightforward to determine in the current experimental set-up. Furthermore, the coincidence detection approach employed in this thesis makes it possible to study not only the correlations of the kinetic energy partitioning, but also the photoelectron-photofragment angular correlations.[63,64] As a result, one can efficiently measure the PAD in the photofragment recoil frame (RF),

obtaining more chemical insights than the LF angular distribution measurements. This will be used in the studies of the DPD of $HOCO^-$ reported in this thesis, and discussed in more detail later.

1.5 Conclusion

In this chapter, the motivations, background and experimental approach of this thesis work have been introduced. It has been shown that using dissociative photodetachment of negative ions and equipped with photoelectron-photofragment coincidence spectroscopy, the dynamics of gas-phase transient species can be studied in detail. The remainder of this thesis is divided into five chapters. Chapter 2 focuses on the experimental apparatus and data analysis procedure. In Chapter 3, the dynamics and energetics of the acetyloxyl radical studied by the DPD of acetate anion at $E_{h\nu}$ = 3.50 and 4.81 eV will be discussed. In Chapter 4, the dynamics on the PES of OH + CO → HOCO → H + CO_2 reaction is unraveled by the DPD study of $HOCO^-$ and its deuterated form $DOCO^-$ at $E_{h\nu}$ = 3.21 eV. The near-threshold one- and two-photon photodetachment of $HOCO^-$ will be presented in Chapter 5, with the emphasis on a novel way to align $HOCO^-$, a molecular anion, through a shape resonance. Finally in Chapter 6, the photoelectron-photofragment angular correlations in the DPD of $HOCO^-$ and $DOCO^-$ will be discussed, providing insight into the lifetime of HOCO and DOCO radicals.

References

[1] H. Eyring and M. Polanyi, Z. Phys. Chem. Abt. B **12**, 279 (1931).

[2] J. C. Polanyi, Science **236**, 680 (1987).

[3] Y. T. Lee, Science **236**, 793 (1987).

[4] J. H. Sullivan, J. Chem. Phys. **46**, 73 (1967).

[5] L. J. Butler, Annu. Rev. Phys. Chem. **49**, 125 (1998).

[6] I. W. M. Smith and A. R. Ravishankara, J. Phys. Chem. A **106**, 4798 (2002).

[7] I. W. M. Smith, Chem. Soc. Rev. **31**, 137 (2002).

[8] F. Fernandez-Alonso and R. N. Zare, Annu. Rev. Phys. Chem. **53**, 67 (2002).

[9] B. K. Carpenter, J. Phys. Org. Chem. **16**, 858 (2003).

[10] R. T. Skodje and X. M. Yang, Int. Rev. Phys. Chem. **23**, 253 (2004).

[11] I. Glassman, *Combustion*, 3rd ed. (Academic Press, San Diego, CA, USA, 1996).

[12] J. A. Miller, R. J. Kee, and C. K. Westbrook, Annu. Rev. Phys. Chem. **41**, 345 (1990).

[13] X. L. Song, J. C. Li, H. Hou, and B. S. Wang, J. Chem. Phys. **125**, 094301 (2006).

[14] M. J. Frost, P. Sharkey, and I. W. M. Smith, Faraday Discuss. **91**, 305 (1991).

[15] B. Ruscic and M. Litorja, Chem. Phys. Lett. **316**, 45 (2000).

[16] H. G. Yu, J. T. Muckerman, and T. J. Sears, Chem. Phys. Lett. **349**, 547 (2001).

[17] M. J. Lakin, D. Troya, G. C. Schatz, and L. B. Harding, J. Chem. Phys. **119**, 5848 (2003).

[18] R. P. Wayne, *Chemistry of Atmospheres*, 2nd ed. (Clarendon, Oxford, 1991).

[19] H. S. Johnston, Annu. Rev. Phys. Chem. **43**, 1 (1992).

[20] E. A. Lissi, G. Massiff, and A. E. Villa, J. Chem. Soc. Faraday Trans. **69**, 346 (1973).

[21] B. S. Wang, H. Hou, and Y. S. Gu, J. Phys. Chem. A **103**, 8021 (1999).

[22] D. E. Milligan and M. E. Jacox, J. Chem. Phys. **54**, 927 (1971).

[23] M. E. Jacox, J. Chem. Phys. **88**, 4598 (1988).

[24] D. Forney, M. E. Jacox, and W. E. Thompson, J. Chem. Phys. **119**, 10814 (2003).

[25] A. H. Zewail, J. Phys. Chem. **100**, 12701 (1996).

[26] A. H. Zewail, J. Phys. Chem. A **104**, 5660 (2000).

[27] A. Stolow, Annu. Rev. Phys. Chem. **54**, 89 (2003).

[28] O. Gessner, A. M. D. Lee, J. P. Shaffer, H. Reisler, S. V. Levchenko, A. I. Krylov, J. G. Underwood, H. Shi, A. L. L. East, D. M. Wardlaw, E. T. Chrysostom, C. C. Hayden, and A. Stolow, Science **311**, 219 (2006).

[29] H. Ihee, V. A. Lobastov, U. M. Gomez, B. M. Goodson, R. Srinivasan, C. Y. Ruan, and A. H. Zewail, Science **291**, 458 (2001).

[30] R. Srinivasan, J. S. Feenstra, S. T. Park, S. J. Xu, and A. H. Zewail, Science **307**, 558 (2005).

[31] L. J. Butler and D. M. Neumark, J. Phys. Chem. **100**, 12801 (1996).

[32] P. G. Wenthold, D. A. Hrovat, W. T. Borden, and W. C. Lineberger, Science **272**, 1456 (1996).

[33] R. E. Continetti, Int. Rev. Phys. Chem. **17**, 227 (1998).

[34] R. E. Continetti, Annu. Rev. Phys. Chem. **52**, 165 (2001).

[35] D. M. Neumark, Phys. Chem. Chem. Phys. **7**, 433 (2005).

[36] D. M. Neumark, J. Chem. Phys. **125**, 132303 (2006).

[37] M. C. Garner, K. A. Hanold, M. S. Resat, and R. E. Continetti, J. Phys. Chem. A **101**, 6577 (1997).

[38] R. R. Corderman and W. C. Lineberger, Annu. Rev. Phys. Chem. **30**, 347 (1979).

[39] H. Massey, *Negative Ions*, 3rd ed. (Cambridge University, Cambridge, 1976).

[40] J. H. D. Eland, *Photoelectron Spectroscopy: An Introduction to ultraviolet Spectroscopy in Gas Phase*, 2nd ed. (Butterworths, London, 1984).

[41] P. Chen, in *Unimolecular and Bimolecular Ion-Molecule Reaction Dynamics*, edited by C. Y. Ng, T. Baer, and I. Powis (John Wiley & Sons, West Sussex, 1994).

[42] S. E. Bradforth, D. W. Arnold, R. B. Metz, A. Weaver, and D. M. Neumark, J. Phys. Chem. **95**, 8066 (1991).

[43] E. De Beer, E. H. Kim, D. M. Neumark, R. F. Gunion, and W. C. Lineberger, J. Phys. Chem. **99**, 13627 (1995).

[44] C. R. Sherwood, M. C. Garner, K. A. Hanold, K. M. Strong, and R. E. Continetti, J. Chem. Phys. **102**, 6949 (1995).

[45] C. R. Sherwood, K. A. Hanold, M. C. Garner, K. M. Strong, and R. E. Continetti, J. Chem. Phys. **105**, 10803 (1996).

[46] T. G. Clements and R. E. Continetti, J. Chem. Phys. **115**, 5345 (2001).

[47] A. M. Wodtke and Y. T. Lee, in *Molecular Photodissociation Dynamics*, edited by M. N. R. Ashfod and J. E. Braggott (The Royal Society of Chemistry, London, 1987).

[48] D. W. Chandler and P. L. Houston, J. Chem. Phys. **87**, 1445 (1987).

[49] D. H. Parker and A. Eppink, J. Chem. Phys. **107**, 2357 (1997).

[50] R. N. Dixon, D. W. Hwang, X. F. Yang, S. Harich, J. J. Lin, and X. Yang, Science **285**, 1249 (1999).

[51] A. J. R. Heck and D. W. Chandler, Annu. Rev. Phys. Chem. **46**, 335 (1995).

[52] M. N. R. Ashfold, N. H. Nahler, A. J. Orr-Ewing, O. P. J. Vieuxmaire, R. L. Toomes, T. N. Kitsopoulos, I. A. Garcia, D. A. Chestakov, S. M. Wu, and D. H. Parker, Phys. Chem. Chem. Phys. **8**, 26 (2006).

[53] D. P. Debruijn and J. Los, Rev. Sci. Instrum. **53**, 1020 (1982).

[54] D. R. Cyr, D. J. Leahy, D. L. Osborn, R. E. Continetti, and D. M. Neumark, J. Chem. Phys. **99**, 8751 (1993).

[55] R. E. Continetti, D. R. Cyr, D. L. Osborn, D. J. Leahy, and D. M. Neumark, J. Chem. Phys. **99**, 2616 (1993).

[56] J. H. D. Eland, J. Chem. Phys. **70**, 2926 (1979).

[57] M. Takahashi, J. P. Cave, and J. H. D. Eland, Rev. Sci. Instrum. **71**, 1337 (2000).

[58] K. A. Hanold, C. R. Sherwood, M. C. Garner, and R. E. Continetti, Rev. Sci. Instrum. **66**, 5507 (1995).

[59] K. A. Hanold, C. R. Sherwood, and R. E. Continetti, J. Chem. Phys. **103**, 9876 (1995).

[60] H. J. Deyerl, T. G. Clements, A. K. Luong, and R. E. Continetti, J. Chem. Phys. **115**, 6931 (2001).

[61] J. A. Davies, J. E. LeClaire, R. E. Continetti, and C. C. Hayden, J. Chem. Phys. **111**, 1 (1999).

[62] Z. Lu, Q. C. Hu, J. E. Oakman, and R. E. Continetti, J. Chem. Phys. **126**, 194305 (2007).

[63] K. A. Hanold, M. C. Garner, and R. E. Continetti, Phys. Rev. Lett. **77**, 3335 (1996).

[64] K. A. Hanold and R. E. Continetti, Chem. Phys. **239**, 493 (1998).

[65] T. G. Clements, R. E. Continetti, and J. S. Francisco, J. Chem. Phys. **117**, 6478 (2002).

[66] J. Cooper and R. N. Zare, J. Chem. Phys. **48**, 942 (1968).

[67] J. Cooper and R. N. Zare, in *Lectures in Theoretical Physics* (Gordon and Breach, Inc., New York, 1969), Vol. XI, pp. 317.

[68] K. L. Reid, Annu. Rev. Phys. Chem. **54**, 397 (2003).

[69] R. N. Zare, Mol. Photochem. **4**, 1 (1972).

Chapter 2

Experimental Methods and Data Analysis

Experiments reported in this thesis were carried out with a fast-ion-beam photoelectron-photofragment coincidence (PPC) spectrometer. The details of the experimental apparatus and techniques have been described elsewhere.[1-4] Therefore, this chapter will only review the essential aspects of the PPC spectrometer and then focus on several major modifications that were carried out during this thesis work, including the improvement of the vacuum system and the construction of a new generation of the neutral photofragment detector using a fast-crossed-delay-line (FXDL) anode. In section 2.1, an overview of the experimental apparatus, including the generation and manipulation of the fast negative ion beam, the important elements of the laser system, as well as the basic procedure of a PPC measurement, are presented. The improvements of the vacuum system are summarized in section 2.2. Section 2.3 briefly describes the photoelectron detector, while section 2.4 discusses the construction, operation, and calibration of the neutral photofragment detector in detail. Finally, a conclusion of this chapter is provided by section 2.5.

2.1 Overview of the Experimental Apparatus

The fast-ion-beam PPC spectrometer consists of four differentially pumped regions, as shown in Figure 2-1. The negative ions studied in this thesis were generated in the source region by two different methods. The acetate anions, $CH_3CO_2^-$, are produced

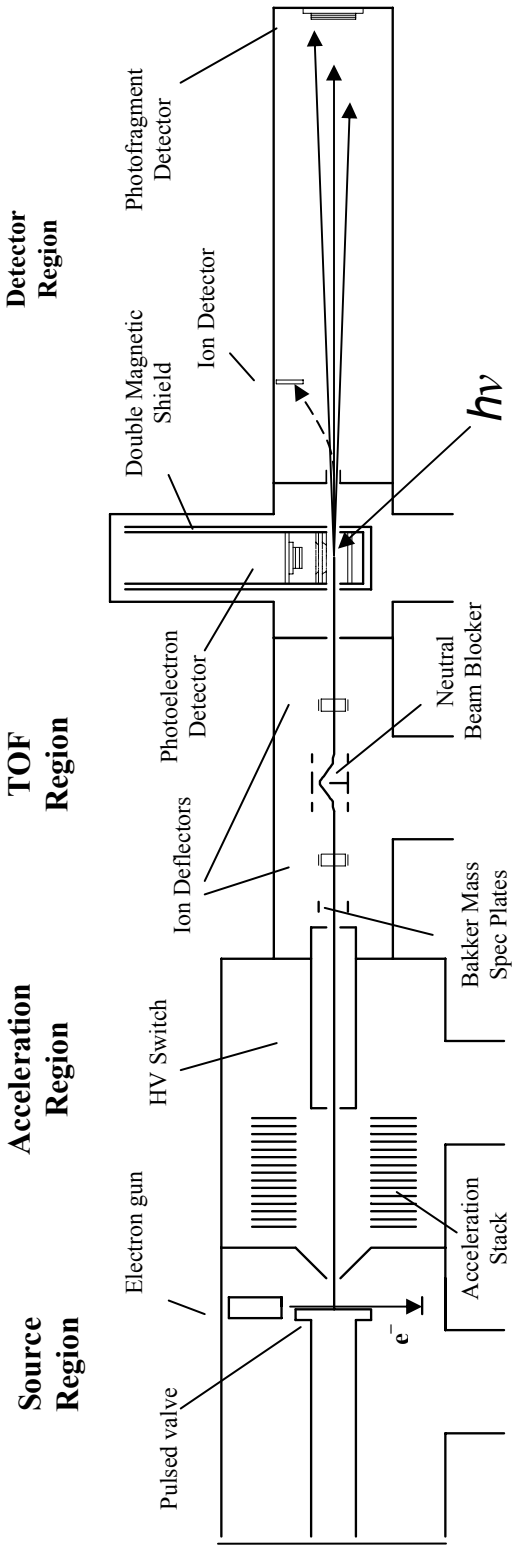

Figure 2-1: Schematic of the experimental apparatus.

by passing acetic acid (CH_3CO_2H) seeded in N_2O/Ar gas mixture through a pulsed discharge ion source operated at 1 kHz.[5] The dissociative electron attachment of N_2O in the discharge forms O^-, which in turn abstracts the acidic proton from CH_3CO_2H and consequently produces $CH_3CO_2^-$. Alternatively, the $HOCO^-$ is produced by electron impact on a supersonic expansion of a $CO/N_2O/CH_4/N_2$ mixture. An electron beam with 1 keV energy ionizes molecules by collisions, generating slow secondary electrons that attach to neutral molecules to form negative ions. In the production of $HOCO^-$, O^- generated by the electron impact on N_2O abstracts an H atom from CH_4, forming OH^- which combines with CO in the free-jet expansion to produce the $HOCO^-$.

The anions created in the source region are skimmed into the second differentially pumped region (acceleration region), accelerated to 3 – 10 keV by a stack of monotonically increasing positive potential plates with 5 cm diameter holes centered along the ion beam axis, and travel into a metal cylinder that is initially floated at the acceleration potential. Once the anions are inside the cylinder, the high voltage potential is rapidly switched to zero in order to re-reference the anions to ground potential. Here the rapid change of potential is accomplished by a 1 kHz high voltage switch (Behlke HTS 221-06), with a falling edge transition of less than 40 ns when switching from an 8 kV potential to ground.

The anions with different masses exiting from the acceleration region often have significant overlap with each other. To solve this problem, a time-of-flight (TOF) mass spectrometer described by Bakker is employed which first selects a short packet of ions by a rapidly changing potential with the electric field perpendicular to the ion beam.[6] Ions within this packet are then mass-selected by TOF since they all have the same beam

energy. The TOF region also contains two sets of four-way deflectors positioned perpendicular to the beam propagation that are used to guide the ion beam, and a neutral beam blocker to stop any neutral particles remaining in the negative ion beam.[1]

The mass-selected negative ions are perpendicularly crossed by a linearly polarized laser that is focused on the interaction volume by a 0.5 m focal lens. Several laser wavelengths were employed in this thesis work. The fundamental (772 nm, $E_{h\nu}$ = 1.60 eV) and second harmonic (386 nm, $E_{h\nu}$ = 3.21 eV) of a picosecond Ti:Sapphire laser (FWHM ~ 1.8 ps, CPA 2000, Clark MXR, Inc.) were used in the dissociative photodetachment (DPD) study of $HOCO^-$. The third harmonic (257 nm, $E_{h\nu}$ = 4.82 eV) from the same Ti:Sapphire laser and the third harmonic (355 nm, $E_{h\nu}$ = 3.49 eV) of a Nd:YAG laser (FWHM ~ 100 ps, Quantronix Model 116) were employed to photodetach the $CH_3CO_2^-$ anion. To obtain the product angular distributions, a half-wave plate is used to rotate the linear polarization of the laser before it enters the PPC spectrometer through a quartz window.

The photoelectrons generated by photodetachment are recorded by a time- and position-sensitive electron detector that is placed parallel to the plane of the laser and ion beams. Undetached anions are deflected out of the ion beam by an electrostatic field and collected by an ion detector. The neutral photofragments recoil from the center of mass (CM) and propagate over a 1.4 m flight path to impinge on another time- and position-sensitive detector. The details of the photoelectron and neutral photofragment detectors will be discussed in sections 2.3 and 2.4, respectively.

A successful PPC experiment requires the synchronization of different parts of the spectrometer. The pulsed laser is used as the “clock” for the PPC spectrometer. The

timing between the mass spectrometer and laser pulse is set according to the anion TOF from the mass spectrometer to the laser interaction region, typically on the order of several microseconds depending on the beam energy and the mass of anion. The timing of the potential switch in the acceleration region and the pulsed valve in the source region are set to be ~1 μs and ~ 300 – 500 μs before the mass spectrometer, respectively. These timings may be varied during the experiment to optimize the ion intensities. In a DPD experiment, every laser pulse is used to trigger the operations of pulsed valve, potential switch, and mass spectrometer in the next data acquisition cycle. The firing of the laser shot is also used as the timing reference for photoelectron and photofragment detectors as discussed in the section 2.4.2 below, providing appropriate gates for the detectors so that only the signals arriving within a certain time window are accepted, reducing the background noise.

2.2 Improvement of the Vacuum System

During a PPC experiment, the source, acceleration, TOF, and detector regions of the fast-ion-beam spectrometer are operated at pressures of ~10^{-4}, 10^{-5}, 10^{-6}, and 10^{-9} torr, respectively, in order to achieve a free-jet expansion and collisionless conditions for the DPD study. During this thesis work, the vacuum system was improved significantly. The vacuum of the source region was previously maintained by a 2000 l/s diffusion pump (Edwards Diffstak 250/2000 M) backed by a 40 m^3/hr mechanical pump (Edwards E2M40). The new vacuum system employs an 8000 l/s diffusion pump (Varian VHS-400) backed by a 500 m^3/hr roots-blower pump (Edwards EH500) in series with an 80 m^3/hr mechanical pump (Edwards E2M40). In the acceleration region, a 2000 l/s diffusion

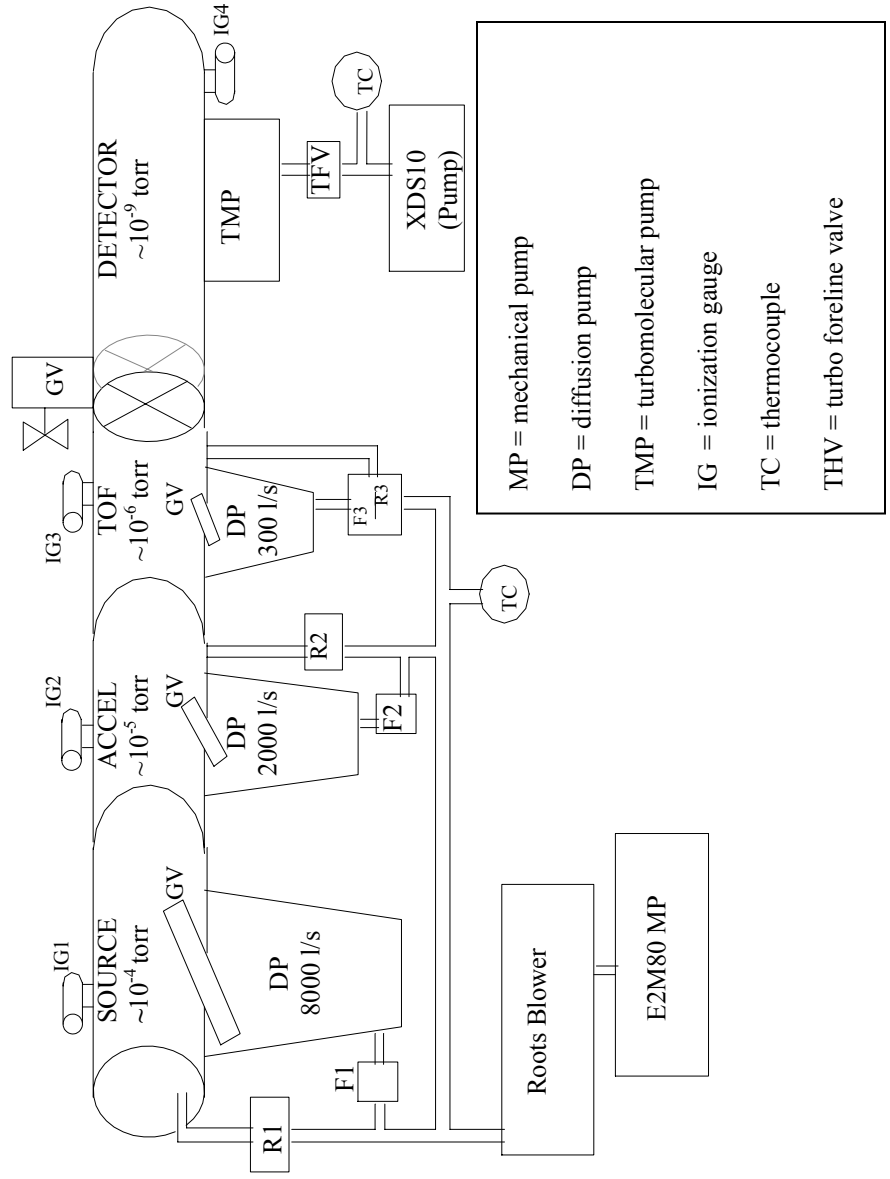

Figure 2-2: Schematic of vacuum system.

pump (Edwards Diffstak 250/2000 M) replaces the previous 700 l/s diffusion pump (Edwards Diffstak 160/700 M). In the current set-up, the roots-blower system backing the source diffusion pump is also used to maintain the backing vacuum for the diffusion pumps in the acceleration and TOF regions. The detector region requires an ultrahigh vacuum (UHV). Previously this was achieved by a 350 l/s turbomolecular pump (Edwards EXT351/160CF) backed by a 150 l/s diffusion pump (Edwards Diffstak 63/150 M) and a 5 m^3/hr mechanical pump (Edwards E2M5). The modified pumping system for the detector region uses a 700 l/s magnetic suspended molecular pump (Osaka Vacuum, LTD., TG713MC) backed by a 13.4 m^3/hr dry scroll mechanical pump (Edwards XDS 10). These two pumps for the detector region do not use any pump oil, and therefore provide a cleaner environment than the previous set-up. With the increased pumping speed for most of the regions in the PPC spectrometer, the generation and detection of more intense anion beams are feasible. A schematic of this new vacuum system is presented in Figure 2-2.

2.3 Photoelectron Detector

The full 4π solid angle of photoelectrons produced by the photodetachment is collected by a space-focusing extraction assembly, as described by Hayden and coworkers.[7-9] As shown in Figure 2-3, the space-focusing photoelectron collector contains an extraction field, typically ranging between ~5 to ~20 V/cm, and a field free flight region. This extraction voltage is applied as a negative pulse to the bottom plate, with the -25V shown on Fig. 2.3 corresponding to a field of ≈14 V/cm. This voltage is switched on ≈ 140 ns before the laser pulse to minimize deflection of the parent anion

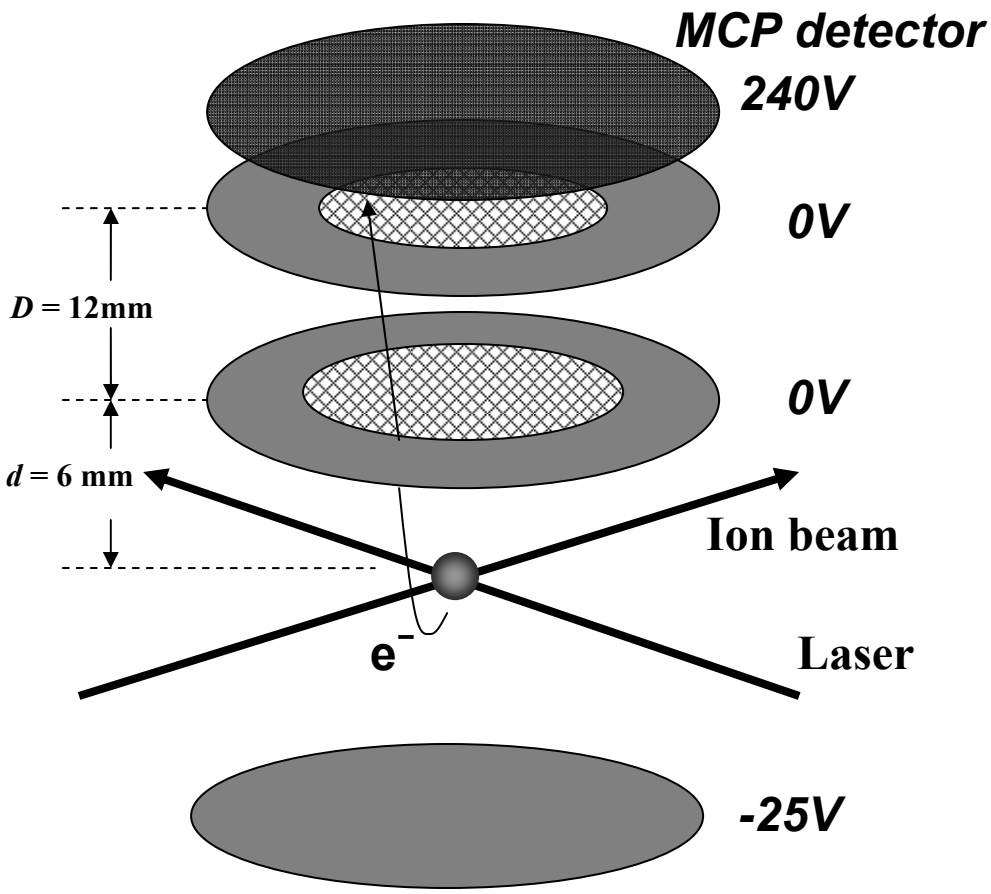

Figure 2-3: Schematic of the space-focused photoelectron detector assembly.

beam. The accelerated electrons pass through the first ground grid with 80% transmission and enter into the field-free region, travel over a distance of D = 12 mm, pass through a second grounded grid with the same transmission, and finally are accelerated toward the front microchannel plate (MCP) at a positive potential. For the convenience of the discussion here, we choose the z axis as the direction perpendicular to the photoelectron detector face and designate the z component of the photoelectron velocity vector by $\bar{v}_z$. In

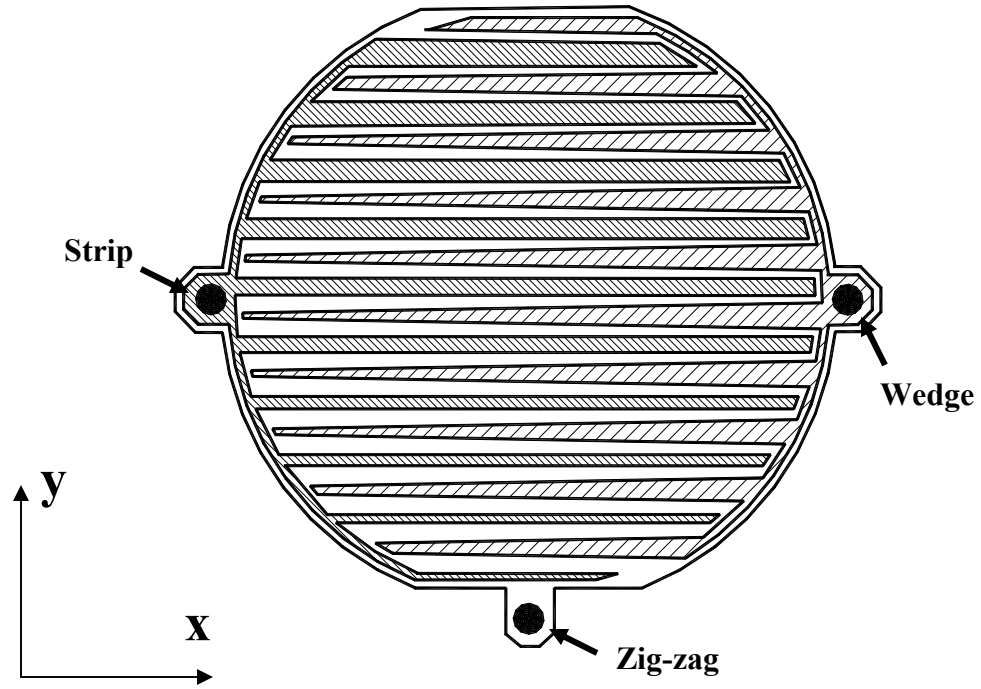

Figure 2-4: Schematic of the wedge-and-strip anode in the photoelectron detector.

Figure 2-3, the field-free distance *D* is set to be twice of the distance *d* between the laser interaction region and first grounded grid, resulting in the arrival time of photoelectron with the same $\vec{v}_z$ to be insensitive to the variation of photodetachment position along z direction.[8] The photoelectrons collected by the space-focusing assembly impinge on a stack of three MCPs and generate a cloud of electrons. By this means, the photoelectron signals are amplified. The electron cloud is then detected by a time- and position-sensitive anode floating at a positive high voltage. The anode used in the photoelectron detector is a "wedge-and-strip" type as shown in Figure 2-4.[10] It consists of three

conductor components “wedge”, “strip”, and, “zig-zag”, which are insulated from each other. Because these three conductors share the area of the detector face differently along the x and y coordinates as shown in Fig. 2-4, one can calculate the position-of-arrival using the charge division of the electron cloud among the three conductors:

$$x \propto \frac{Q_w}{Q_s + Q_w + Q_z}, \tag{2-1}$$

$$y \propto \frac{Q_s}{Q_s + Q_w + Q_z}. \tag{2-2}$$

In addition, the photoelectron TOF signal can be picked off from the wedge component and serves as a measure of the photoelectron distributions in *z* direction. The calculations and calibrations of photoelectron signals have been reviewed in detail in Ref. 9.

2.4 Neutral Photofragment Detector

The kinetic energy release (KER) among the neutral photofragments produced in a DPD process is typically on the order of eV, while the parent anion has a beam energy of several keV. Therefore, although photofragments recoil away from the CM after photodetachment, the laboratory velocity component parallel to the propagation direction of the parent ion beam is easily large enough to strike the MCP stack and generate an electron cloud that can be detected by the time- and position-sensitive anode.

Two types of anodes were used for the photofragment detector in the experiments presented here. In the DPD study of $CH_3CO_2^-$, the same type of wedge-and-strip anode as used in the photoelectron detector was employed to record the neutral photofragments. However, the dead time of the charge-division anode is on the order of μs, larger than the

separation time between the pair of photofragments from any DPD event. To achieve the coincidence measurement of the two dissociation fragments, the anode was divided into two halves separated by a 7-mm-diameter beam blocker at the center. In the measurement of a two-body break-up, each of the two halves has to be struck by one of the paired photofragments. In the measurement of a stable neutral product, the photofragment detector has to be shifted to an off-centered position so that the stable neutral particle will avoid the beam blocker. Due to the relatively long dead time, neither three-body dissociations, nor two-body dissociations with the photofragments recoiling along the ion beam direction, can be studied with the wedge-and-strip anode. For that reason a new detector based on delay-line technology with minimal deadtime was implemented as discussed in the next section.

2.4.1 Fast-Crossed-Delay-Line Detector

A new-generation photofragment detector based on a fast-crossed-delay-line (FXDL) anode was installed on the PPC spectrometer and used for the DPD studies of $HOCO^-/DOCO^-$ presented in Chapters 4 – 6 of this thesis. The FXDL anode uses time-division instead of charge-division to resolve position information, and is similar to a previous version of quadrant-crossed-delay-line (QXDL) anode described by Hanold *et al.*.[11] The FXDL has two sets of signal conductor fingers oriented along the x and y directions in two insulated layers, respectively, as shown in Figure 2-5. In each layer a conductive delay line connects the ends of individual signal conductor fingers. A layer of grounded conductive strips oriented parallel to the top signal fingers are inserted to prevent cross talk between the x and y signal fingers, while all three conductive layers are

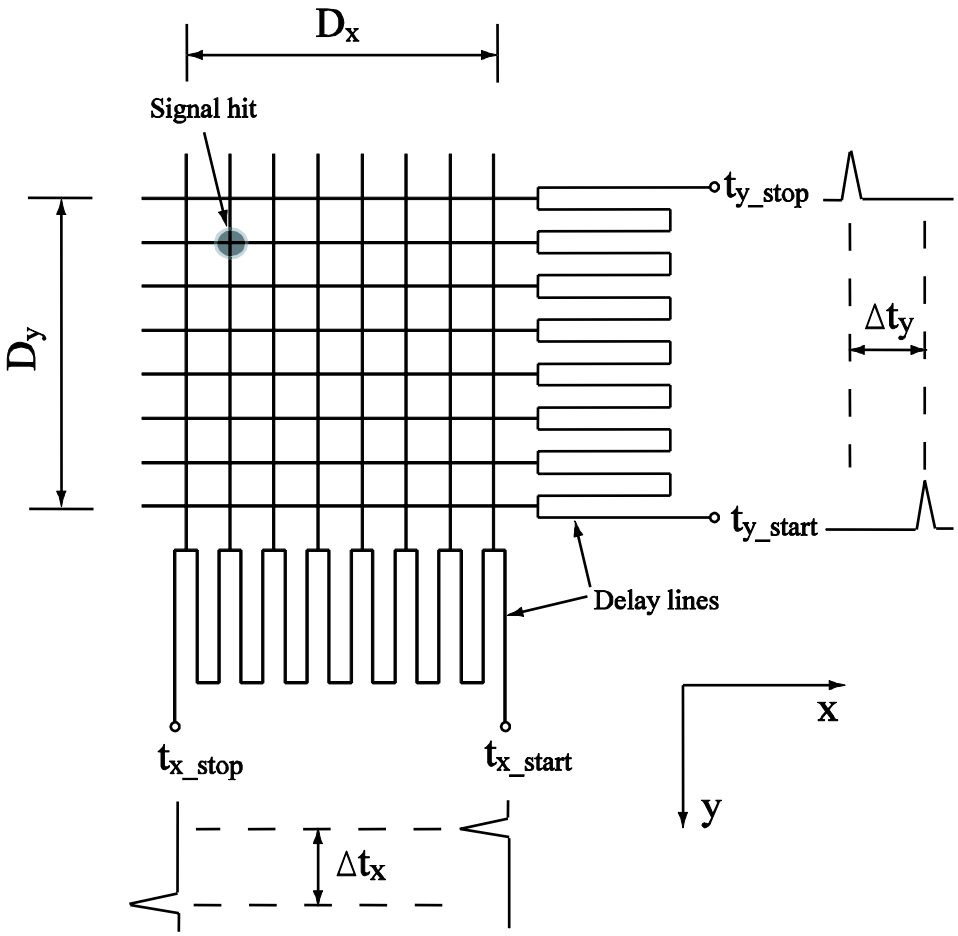

Figure 2-5: Schematic of the FXDL anode.

insulated from each other by dielectric strips which are also oriented parallel to the top signal fingers. The bottom signal finger layer is insulated from the grounded anode base as well.

When the electron cloud (≈2 x 10^7 e^-) from the MCP stack strikes a given area on the anode, the charges are partitioned onto the x and y signal conductor fingers and propagate to the two ends of each delay line. The x and y positions can then be calculated

from the time-of-arrival of the charge at the ends of each delay line as illustrated in Figure 2-5 since

$$X = \frac{D_x}{2\tau_x}\Delta t_x = \frac{D_x(t_{x\_stop} - t_{x\_start})}{2(t_{x\_stop} + t_{x\_start})}, \tag{2-3}$$

$$Y = \frac{D_y}{2\tau_y}\Delta t_y = \frac{D_y(t_{y\_stop} - t_{y\_start})}{2(t_{y\_stop} + t_{y\_start})}, \tag{2-4}$$

where D_x and D_y are the dimensions of the FXDL active area along the x and y coordinate, τ_x and τ_y are the total time it takes the charges to travel from end to end along the x and y delay lines, and Δt_x and Δt_y are the difference of time-of-arrival of charges at the two ends of the each delay lines. In this calculation, the position of the anode center is defined to be the spatial origin (0, 0).

The active area of the FXDL used in this thesis work is 45 × 45 mm^2, slightly larger than the 40-mm-diameter field-of-view of the photofragment detector that is determined by the MCP size. Unlike the QXDL anode that has four separated quadrants as described by Hanold *et al.*,[11] the FXDL anode consists of only one active element. Therefore, the two dissociation fragments detected in coincidence by the FXDL detector have to be separated in time-of-arrival by more than the anode dead time. The new-generation photofragment detector using the FXDL also allows coincidence measurements of three-body dissociations as long as the time-of-arrival difference between any two of the three photofragments is larger than the dead time. The observed dead-time will be discussed further below.

A schematic of the photofragment detector is illustrated in Figure 2-6. This set-up includes a stack of three MCPs and an FXDL anode. The front MCP is biased at a

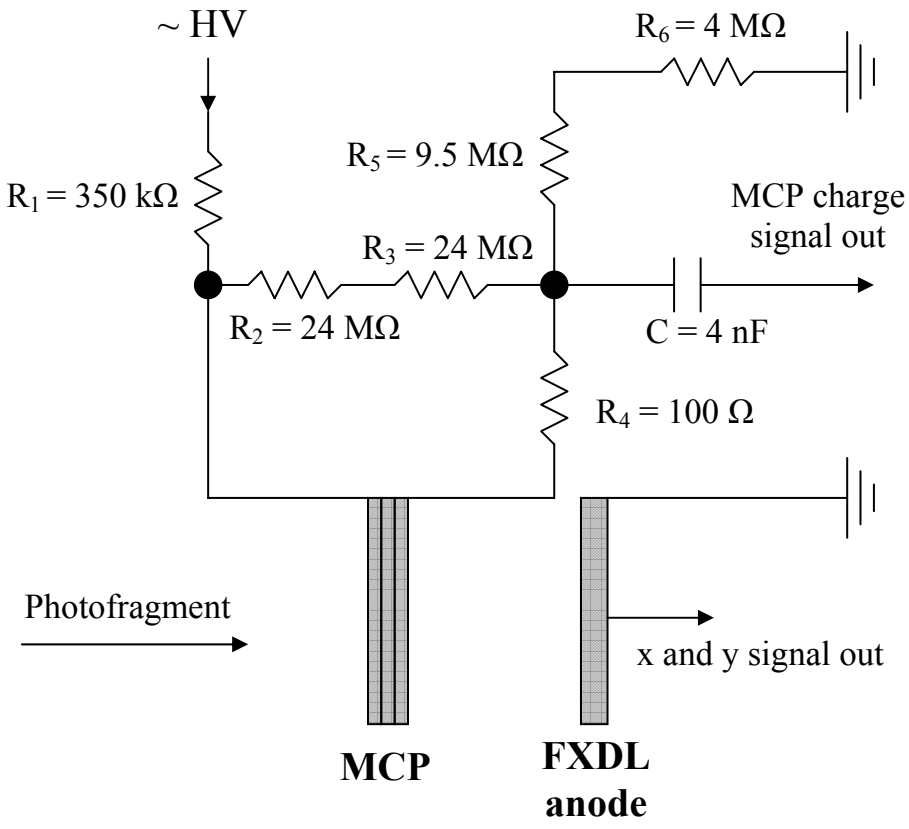

Figure 2-6: Circuit diagram used for FXDL anode. See details in text.

negative high voltage of -5 kV, while the third MCP is floated at ~ -1 kV and resistively coupled to the ground. The grounded FXDL anode is positioned 5 mm away from the third MCP. A 4 nF capacitor is used in the circuit in Figure 2-6 to measure the amount of charges compensated into the MCP when an electron cloud is generated by the impact of photofragments. This signal is fed into a preamplifier (EG&G ORTEC 142 AH) and a pulse-shaping amplifier (EG&G ORTEC 575A) in series before being converted into digital signals. The resulting data provides a measure of the number of photofragments hitting the MCP within a single data acquisition cycle.

2.4.2 Data Acquisition

Figure 2-5 shows that one can measure the x and y positions of a single hit on the FXDL anode by recording the relative time-of-arrival at the two ends of the x and y delay lines. However, PPC spectroscopy requires a coincidence measurement of all of the neutral products generated in a many-body DPD process. Therefore the photofragment detector has to distinguish the time and positions of the different neutral products produced in a single DPD event. The current section describes how this goal is accomplished using a multi-hit time-to-amplitude converter (TAC) system, as well as the conversion of analog signals into digital ones so that the data can be analyzed by computer.

In Figure 2-7, the measurement of the x coordinate is used as an example to show how the multi-hit TAC system works. Although only two-body DPD processes were studied in this thesis, the current multi-hit TAC system is designed to be able to measure up to three neutral dissociation particles in coincidence.

As shown in Figure 2-7, the charges arriving at the two ends of the x delay line on the FXDL anode first enter a timing-and-charge amplifier (Siegmund Scientific, DDLA 101) specially manufactured for this detector. An extra 45 ns delay is added onto the time-of-arrival of X STOP signal to ensure that the X START signal always arrives first. Each of the amplified X START and X STOP signals is then split into three pulses that will be delayed by 0, 6, and 12 ns, respectively, and collected by the multi-hit TAC units. These delays represent the electronic dead-time of the data acquisition system. The practical dead-time is given by the delay-line length of $\approx$ 19 ns.

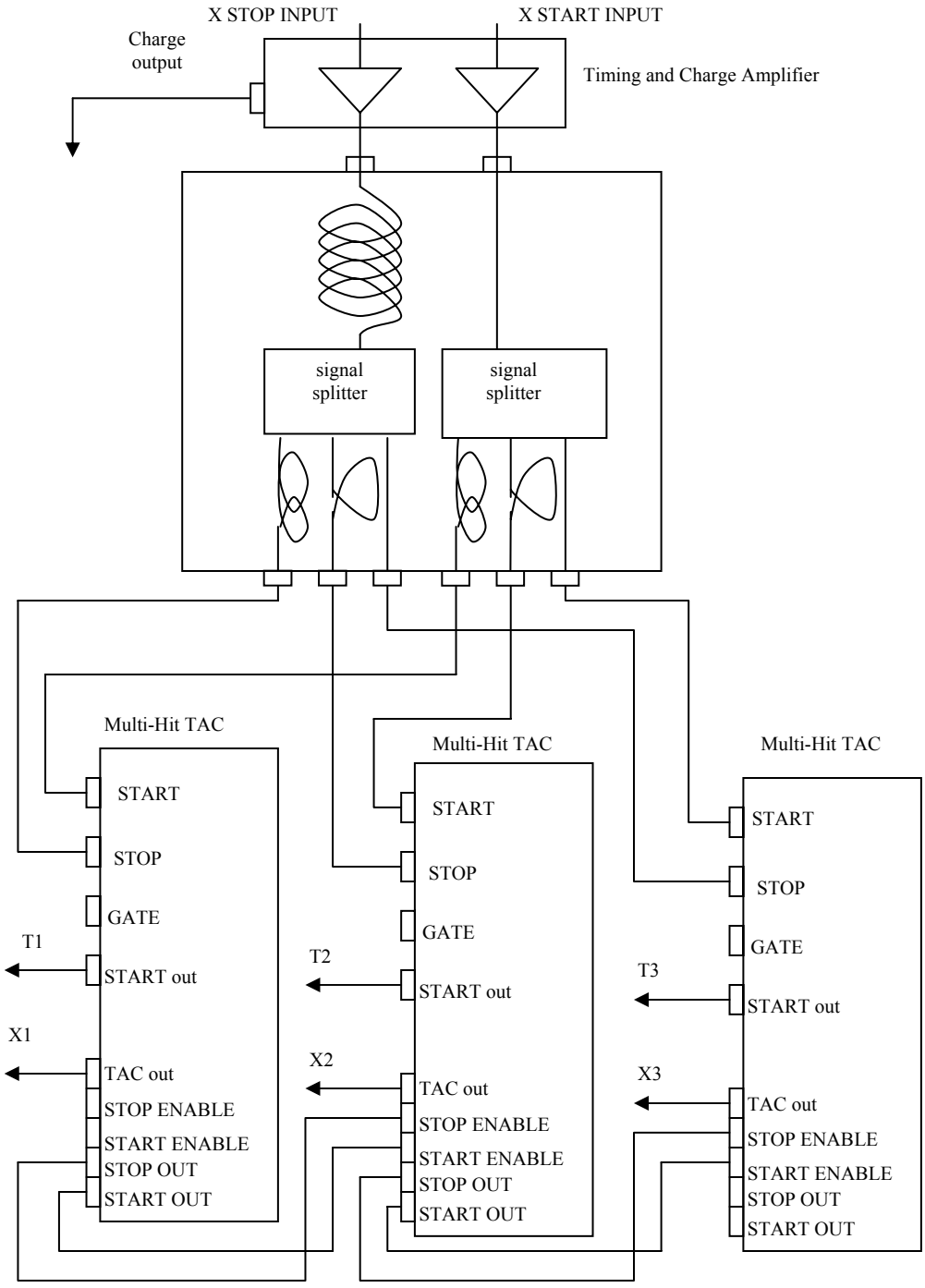

Figure 2-7: Schematic of multi-hit TAC system for signals along the x coordinate.

The multi-hit TAC is a single-wide NIM unit that produces a positive pulse with amplitude proportional to the time difference of the two negative pulses separately input into the "START" and "STOP" ports. Each TAC unit also generates a negative NIM pulse that can be used by a time-to-digital converter (TDC) to measure the timing of the pulse input into the "START" port. For the measurement of x positions, three multi-hit TAC units are employed corresponding to the three pairs of split signals from 0, 6, and 12 ns delay lines. The TAC unit #1 is enabled by jumping the "START ENABLE" and "STOP ENABLE" ports to ground, and therefore is ready to accept signals at any time, while the second and third TAC units are normally disabled.

In the current set-up, the X START (STOP) signals carried by the 12, 6, and 0 ns delay lines are guided into the "START" ("STOP") ports of the first, second, and third TAC units, respectively. In a multi-body dissociation, the photofragments arrive sequentially. The X START (STOP) pulse from the first product can only be recorded by TAC unit #1 because this is the only one enabled. Once TAC #1 receives an X START (STOP) signal, it sends an ECL pulse to enable the "START" ("STOP") port on TAC unit #2. At this moment, the X START (STOP) pulse from the first product leading to TAC unit #2 already passed 6 ns earlier and therefore will not be registered in TAC unit #2. The enabled TAC unit #2 then can only be used to record the pulse from the second product. The third product can be recorded by TAC unit #3 in a similar manner.

Any two dissociation products arriving at the detector within 6 ns cannot be recorded by the current data acquisition system. However, the 19 ns dead time of the FXDL anode itself is larger than this 6 ns period. A similar multi-hit TAC set-up is used to obtain the Y position information. In addition, a charge distribution on the x and y

delay line can be measured individually from the DDLA 101 amplifier. The timing signals are measured from "START" pulses in x delay line.

The X, Y, and timing outputs from the multi-hit TAC units are all analog pulses, and have to be converted into digital signals for analysis. This conversion is accomplished by a peak-sensing analog-to-digital converter (ADC) (Phillips Scientific, model 7164) for the X and Y data and a TDC (Phillips Scientific, model 7186) for the timing data, as shown by Figure 2-8. The charges measured from the back of the MCP stack as well as those measured from the x and y delay lines are also digitized by the ADC. The ADC is gated by a 5-μs-wide negative NIM level pulse that is delayed by several μs after the laser shot, depending on the beam energy and mass of the system under study. The TDC is triggered by the leading edge of the same negative NIM pulse. The digitized 12-bit data are then collected by a personal computer through a CAMAC (computer automated measurement and controller) interface.

2.4.3 Data Analysis and Detector Calibration

The raw data collected from the ADC and TDC are a set of 12 bit integers. To appropriately interpret these raw data and obtain the actual time- and position-of-arrival, the FXDL detector has to be carefully calibrated using a well-characterized system. Once the time- and position-of-arrival are determined, the three-dimensional (3D) velocities of photofragments can be calculated, which in turn can yield rich kinematic information including the center of mass (CM) of the dissociation products, the kinetic energy release (KER), and the angular distributions. In this section, the data analysis methods for

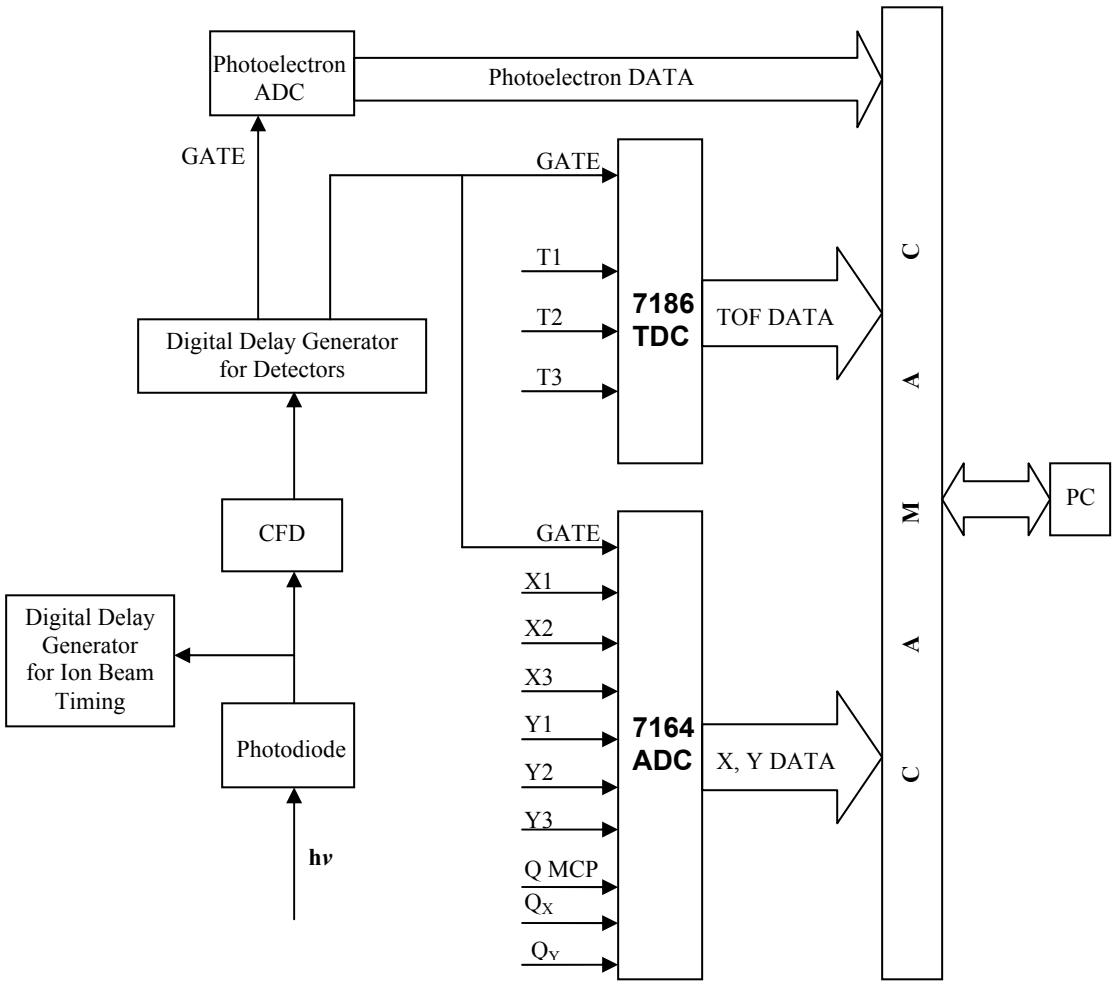

Figure 2-8: Schematic of FXDL data acquisition system. See details in text.

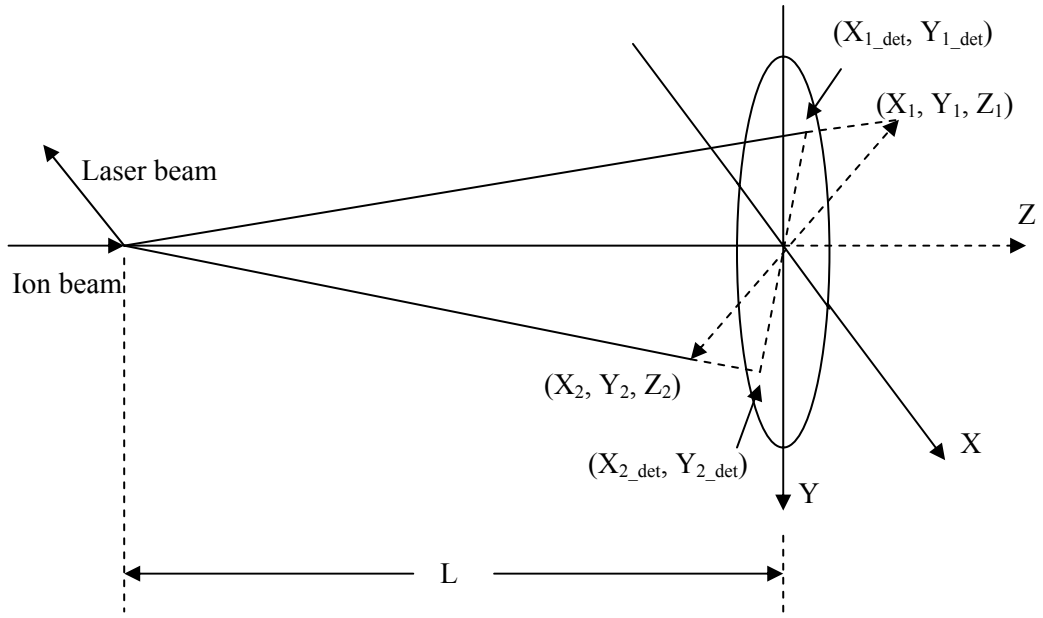

Figure 2-9: Cartesian coordinate system for photofragments in a DPD process.

two-body dissociation as well as the FXDL detector calibration using the DPD of O_4^- at 532 nm ($E_{h\nu}$ = 2.33 eV) are presented.

The schematic of a two-body dissociation process and the definition of the Cartesian coordinates are illustrated in Figure 2-9. The Z direction is chosen to be the same as the parent ion propagation direction, and the X axis points in the counter-laser-propagation direction. The third axis, Y, is determined by the right hand rule to point downwards and be perpendicular to the plane of the laser and ion beams. The XY plane defines the FXDL detector face. Since the dissociation dynamics is most important in the CM frame, the position where the two-body CM hit the detector face is chosen as the spatial origin (0, 0, 0). The 1.4-meter flight path of the two-body CM from the interaction

region to the detector is labeled as L in Figure 2-9. Consequently, the TOF of the CM over the distance L can be calculated by:

$$t_0 = \frac{L}{V_{beam}}, \tag{2-5}$$

where V_{beam} is the velocity of the parent ion beam (the CM).

The principles of the photofragment recoil calculations have been previously presented.[1,12,13] Let us first assume there is no detector stopping the photofragments. In this case, when the CM propagates over the distance L to reach the position of (0, 0, 0) at the given time t_0, the photofragment recoiling forward would have arrived at a position labeled by (X_1, Y_1, Z_1), while the second fragment would reach (X_2, Y_2, Z_2), as shown in Figure 2-9. Here $Z_2 \leq 0 \leq Z_1$. The positions of (X_1, Y_1, Z_1) and (X_2, Y_2, Z_2) can be used to characterize the photofragment recoil at t_0. However, in the experiment, the first photofragment is stopped by the detector at (X_{1_det}, Y_{1_det}) earlier than t_0, while the second fragment continues to fly, hitting the detector at (X_{2_det}, Y_{2_det}) at a time later than t_0, instead of stopping at (X_2, Y_2, Z_2).

Fortunately, since the ion beam is at an energy of several keV and the KER of the recoiling photofragment is typically less than 1 eV in the DPD experiments presented in this thesis, the photofragment recoil velocity components V_{1z} and V_{2z} are less than ~5% of the V_{beam}. As a result, the X, and Y positions can be approximated to be X_{det} and Y_{det} positions measured by the FXDL detector:

$$X_1 \approx X_{1\_det} \quad \text{and} \quad X_2 \approx X_{2\_det} \tag{2-6}$$

$$Y_1 \approx Y_{1\_det} \quad \text{and} \quad Y_2 \approx Y_{2\_det} \tag{2-7}$$

The Z positions can be approximated by:

$$Z_1 \approx -V_{beam} \cdot t_{1\_det} \text{ and } Z_2 \approx -V_{beam} \cdot t_{2\_det} \tag{2-8}$$

Here t_{1_det} is the TOF of the fast photofragment over the distance of Z_1 and is negative because the fast photofragment hits the detector before the CM, while t_{2_det} is positive and defined by the TOF of the slow photofragment from (X_2, Y_2, Z_2) to the detector.

As discussed above, to obtain the photofragment recoil information in the CM frame, the first step is to determine the X_{det}, Y_{det}, and t_{det} values from the raw data. This goal can be accomplished by the linear relationships:

$$X_{\text{det},i} = DMC_{X,i} \cdot X_{raw,i} + DAC_{X,i} \tag{2-9}$$

$$Y_{\text{det},i} = DMC_{Y,i} \cdot Y_{raw,i} + DAC_{Y,i} \tag{2-10}$$

$$t_{\text{det},i} = DMC_{t,i} \cdot T_{raw,i} + DAC_{t,i} - \frac{(X_{\text{det},i} - 1/2\, D_X)}{D_X} \tau_X \tag{2-11}$$

where $X_{raw,i}$, $Y_{raw,i}$, and $T_{raw,i}$ are the raw position data, and DMC and DAC are the multiplicative and additive constants, respectively. The last term in equation (2-11) is used to correct the additional propagation time of the charge over the x delay line since the timing signal is picked from x "START" as shown in Figure 2-7. The constant D_x is the size of FXDL anode along the x dimension shown in Figure 2-5, while τ_x = 19 ns is the total time it takes a signal travel from end to end along x delay line as defined in section 2.4.1. The DMC and DAC constants can be obtained from the detector calibrations.

The mathematical treatment above assumes the CM hits the center of the FXDL detector. However, during an experiment, the detector is often off-centered. In this case, the equations (2-6) and (2-7) will be modified to be:

$$X_i \approx X_{i\_\mathrm{det}} - X_0 \tag{2-12}$$

$$Y_i \approx Y_{i\_\mathrm{det}} - Y_0 \tag{2-13}$$

where (X_0, Y_0) is where the two-body CM hits the detector face.

Once the X, Y and Z positions are calculated, the kinematic information for the two-body dissociation can be obtained. The masses for the slow and fast photofragments are calculated by:

$$m_1 = M\frac{d_2}{d_1 + d_2}, \qquad \text{and} \qquad m_2 = M\frac{d_1}{d_1 + d_2}, \tag{2-14}$$

in which M is the total mass of the parent anion, and d_i is determined by the equation:

$$d_i = \sqrt{X_i^2 + Y_i^2 + Z_i^2}\ . \tag{2-15}$$

The equation to calculate the KER in the two-body dissociation has been derived previously: [12,13]

$$KER = E_{beam}\frac{m_1 m_2}{M^2}\frac{[(V_{beam}t_{co})^2 + R^2]}{L^2}[1 + 2(\frac{m_2 - m_1}{M})\frac{V_{beam}t_{co}}{L}] \tag{2-16}$$

where R and t_{CO} are given by:

$$R = \sqrt{(X_1 - X_2)^2 + (Y_1 - Y_2)^2} \tag{2-17}$$

$$t_{co} = t_2 - t_1 = t_{\mathrm{det},2} - t_{\mathrm{det},1}\,. \tag{2-18}$$

Finally, the angular distribution of the photofragment recoil is obtained by:

$$\theta_{neutral} = \arccos(\frac{Z_1 - Z_2}{\sqrt{(X_1 - X_2)^2 + (Y_1 - Y_2)^2 + (Z_1 - Z_2)^2}}) \tag{2-19}$$

if $m_1 \geq m_2$,and

$$\theta_{neutral} = \arccos\left(\frac{Z_2 - Z_1}{\sqrt{(X_1 - X_2)^2 + (Y_1 - Y_2)^2 + (Z_1 - Z_2)^2}}\right) \quad (2\text{-}20)$$

if $m_1 < m_2$. This approach ensures the calculated angular distributions are all defined by the recoil of heavier photofragment.

The calculations above assume the laser interacts with the ions in an infinitesimal volume. However, in reality, the laser-ion interaction has a non-negligible volume, causing a spatial distribution of the two-body CM, and therefore reducing the measurement resolution. The spatial distribution of the two-body CM is also broadened by the energy spread and the angular divergence of the parent anion beam. The masses calculated from the equation (2-14) are thus expected to have some experimental distribution and in turn affect the KER calculation using the equation (2-16). One solution to this problem is to assign the calculated masses by their nearest peak mass: $m_i = m_i^a$. The m_i^a used for the assignment has to correspond to a photofragment that is energetically feasible to be produced in a DPD using the available thermodynamic data. In addition, the interaction volume is characterized by calculations of the centroid distributions:

$$X_{centroid} = \frac{m_1^a X_1 + m_2^a X_2}{M} \quad (2\text{-}21)$$

$$Y_{centroid} = \frac{m_1^a Y_1 + m_2^a Y_2}{M} \quad (2\text{-}22)$$

$$Z_{centroid} = \frac{m_1^a Z_1 + m_2^a Z_2}{M} \quad (2\text{-}23)$$

A narrow centroid gate with a typical width of 1−2 mm is then used to filter out those data with the CM lying far away from the center of the interaction volume, indicating either a false coincidence or an incorrect mass assignment.

The centroids can be viewed as a measure of linear momentum conservation with the assumption of an infinitely small laser-ion interaction volume. Therefore, centroid gating is particularly useful in the study of multi-channel DPD processes. For example, the DPD of $HOCO^-$ presented in the chapters 4, 5 and 6 produces either H + CO_2 or OH + CO neutral products. To distinguish the two possible DPD channel, the 3D centroids of each photodetachment event are calculated for both H + CO_2 and OH + CO paired masses. Only those events with the H + CO_2 centroids falling into the assigned narrow gates are considered to be valid for the H + CO_2 channel, while the DPD events leading to the OH + CO channel can also be determined in a similar way. The centroid gating significantly reduces the false coincidences from the two individual DPD events as well.

The calibration of the FXDL detector is accomplished by measuring the photofragments from the DPD of O_4^- at $E_{h\nu}$ = 2.33 eV (532 nm). The photoelectron-photofragment energetic and angular distributions produced from this DPD process has been investigated in a great detail previously in our lab.[1,14-18] At $E_{h\nu}$ = 2.37 eV (523 nm), a direct DPD channel (a) as well as a two-step ionic-photodissociation-photodetachment process (b) are observed:

(a) $$O_4^- + h\nu \rightarrow O_2 + O_2 + e^-; \quad (2\text{-}24)$$

(b) $$O_4^- + h\nu \rightarrow O_2 + O_2^-, \quad (2\text{-}25)$$

$$O_2^- + h\nu \rightarrow O_2 + e^-. \quad (2\text{-}26)$$

The KER for channel (a) has a relatively broad distribution peaking at 0.40 eV, while the KER from channel (b) peaks narrowly at 0.80 eV at $E_{h\nu}$ = 2.37 eV.[16] The photon energy used for the FXDL calibration was $E_{h\nu}$ = 2.33 eV. Since the KER in the direct DPD of channel is determined by the Franck-Condon overlap between the anion and repulsive potential, at $E_{h\nu}$ = 2.33 eV, the KER distribution is still expected to peak at 0.40 eV. On the other hand, the KER in the photodissociation channel (b) is determined directly by the difference of the photon energy and the bond dissociation energy of O_2 - O_2^-, thus it is expected to appear at 0.76 eV, as observed. In addition, the O_2 fragments from the DPD of O_4^- were observed to recoil perpendicularly to the laser polarization.[14,16-18]

The goal of the detector calibration is to obtain the correct DMC and DAC constants. During the calibration procedure, all the DMC and DAC constants are carefully adjusted to ensure the resulted KER matches the literature spectra. Several other requirements have to be met as described below.

Figure 2-10 shows a photofragment image which describes the X and Y positions of photofragment arrival. These data were recorded with the laser polarization parallel to the ion beam and perpendicular to the FXDL detector face. Since the O_2 molecules recoil perpendicular to the laser polarization, the photofragment image, which is the projection of the fragment recoil on the XY plane, is expected to be a ring as shown in Figure 2-10. Therefore, the DMC's for X and Y are adjusted to reproduce the ring-type image while the DAC's for X and Y are adjusted to center the ring at (0, 0).

The $DAC_{t,i}$ values can first be tested by the photofragment TOF distribution as shown in Figure 2-11. As discussed above, t_{1_det} is expected to be less than zero as shown

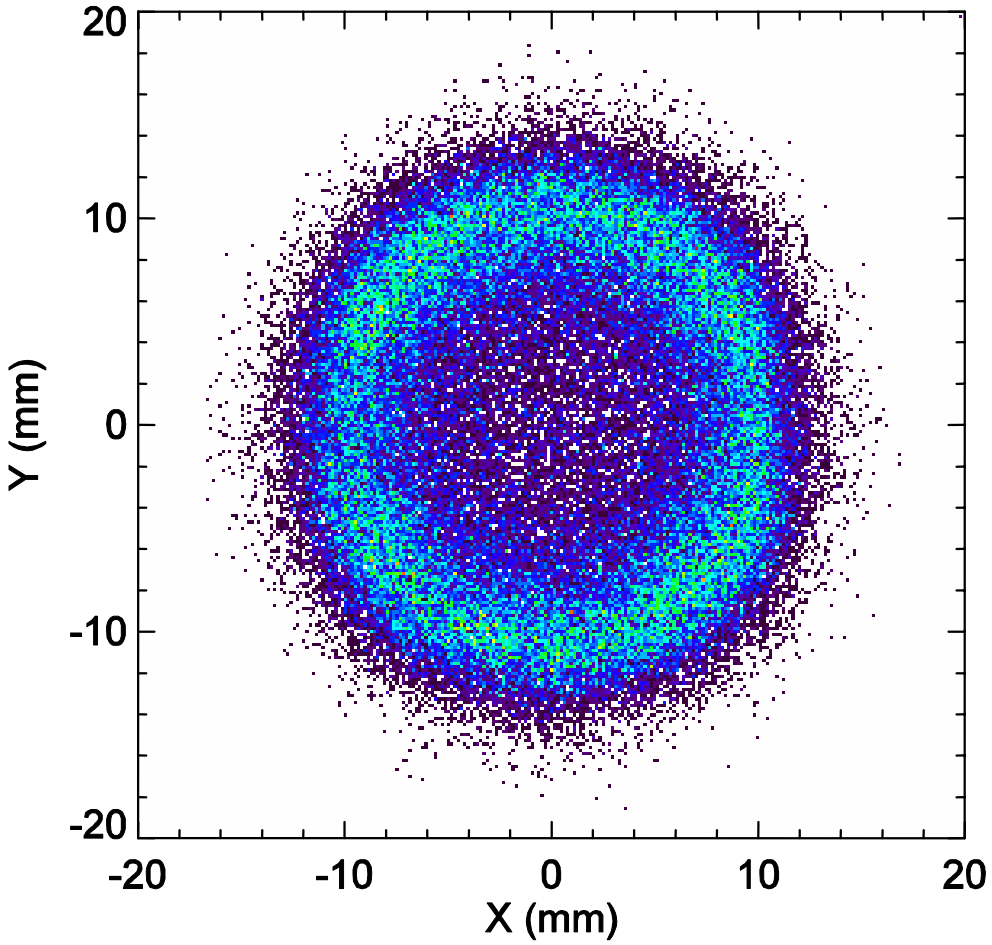

Figure 2-10: Photofragment image from the DPD of O_4^- at $E_{h\nu}$ = 2.33 eV.

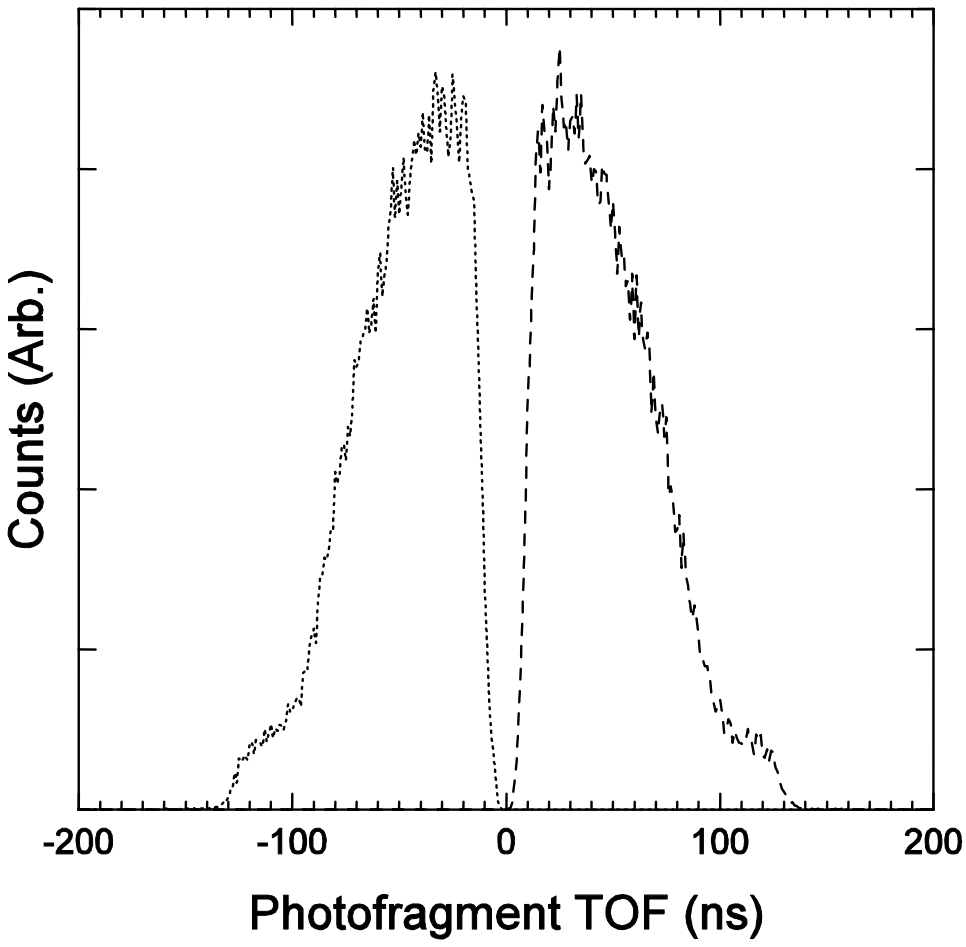

Figure 2-11: TOF spectra of O_2 photofragment from the DPD of O_4^- at $E_{h\nu}$ = 2.33 eV. The TOF for center of mass is defined to be zero. The dotted line represents the TOF of fast photofragment, while the dashed line represent the TOF of slow photofragment.

by the dotted curve in Figure 2-11, while t_{2_det} has to be larger than zero as illustrated by the dashed curve. The gap between the TOF of fast and slow fragments is a measure of the FXDL dead time. In this data, we see a dead-time gap with a ~20 ns FWHM, consistent with the 19 ns delay line length discussed above. The $DMC_{t,i}$ values are adjusted using the two-dimensional (2D) velocity distributions in Figure 2-12. Panel (a) illustrates the V_{per} *v.s.* V_{par}, in which $V_{par} = V_Z$, and V_{per} is the velocity perpendicular to the z-axis, calculated by:

$$V_{per} = \sqrt{V_X^2 + V_Y^2} \tag{2-27}$$

Panel (b) – (d) shows V_X *v.s.* V_Z, V_Y *v.s.* V_Z, and V_Y *v.s.* V_X, respectively. Again the gaps at $V_Z = 0$ in these 2D distributions are caused by the detector dead time. The $DMC_{t,i}$ factors are adjusted to fit the profiles of the images in panel (a) – (c) to a shape of circle. Once the $DMC_{t,i}$, factors are changed, the corresponding $DAC_{t,i}$ also needs to be adjusted to center the images at (0, 0). Since in the panels (a) – (c), the data points on the right side with $V_Z > 0$ correspond to the fast photofragments while those on the left side with $V_Z < 0$ correspond to the slow fragments, the 2D velocity distributions provide a way to evaluate the constants for the fast and slow fragments separately. The resulting DMCs and DACs for the fast and slow fragments are slightly different.

The DMC and DAC constants are then multiplied by a common scale factor to match the KER peaks with the literature values, as shown in Figure 2-13. The whole calibration process needs to be iterated until all the above calibration requirements are met. In addition, the actual value of the ion beam energy needs to be used. This may change as a function of time, for example, if the HV switch circuitry is modified.

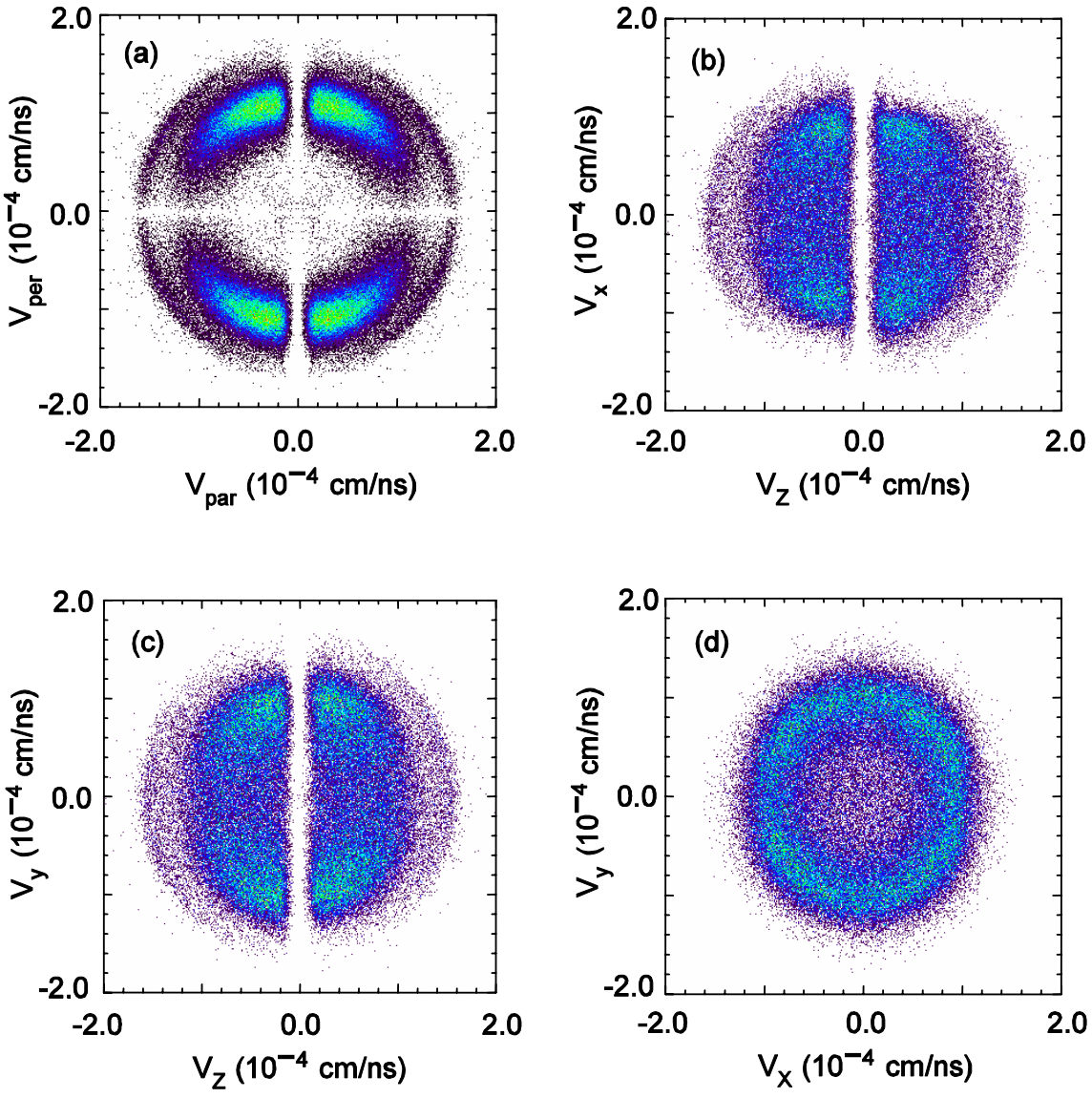

Figure 2-12: Two dimensional velocity distributions of O_2 photofragment from the DPD of O_4^- at $E_{h\nu}$ = 2.33 eV: (a) V_{per} *v.s.* V_{par}; (b) V_X *v.s.* V_Z; (c) V_Y *v.s.* V_Z; and (d) V_Y *v.s.* V_X.

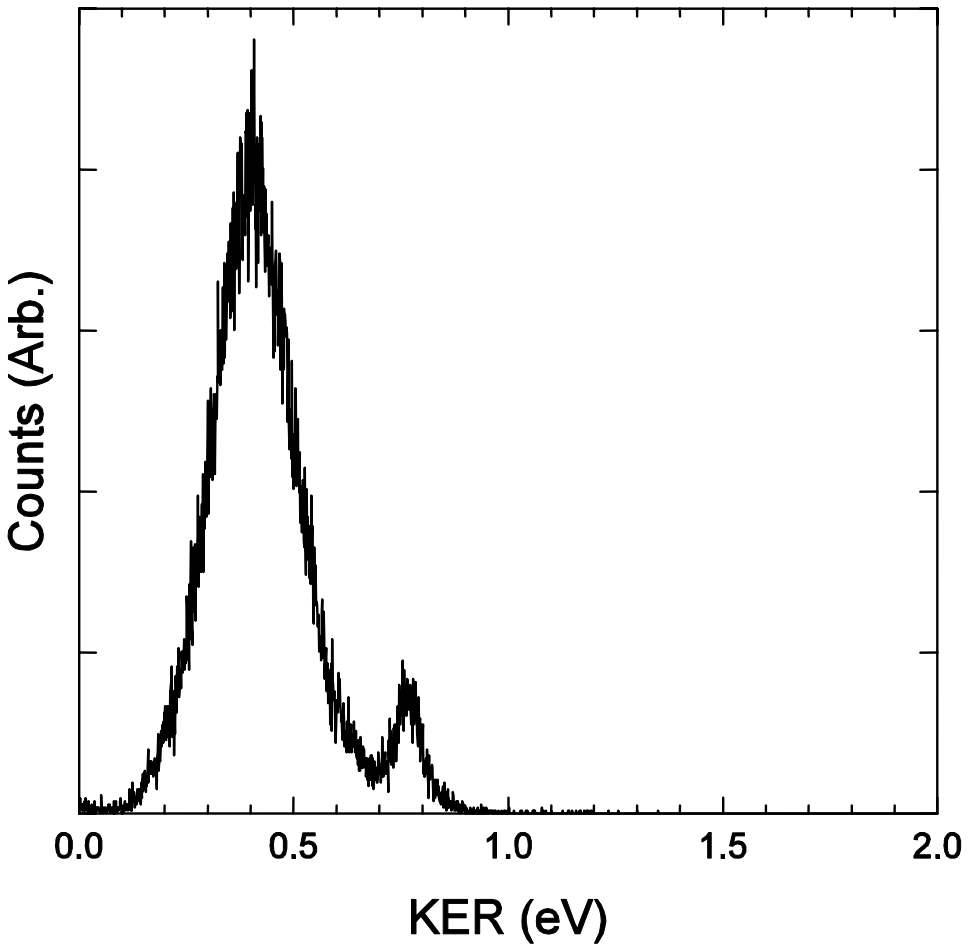

Figure 2-13: The kinetic energy release among O_2 photofragments in the DPD of O_4^- at $E_{h\nu}$ = 2.33 eV. The peak at 0.40 eV corresponds to a direct DPD: $O_4^- + h\nu \rightarrow O_2 + O_2 + e^-$; while the peak at 0.76 eV corresponds to a two-step photodissociation-photodetachment channel: $O_4^- + h\nu \rightarrow O_2 + O_2^-$; $O_2^- + h\nu \rightarrow O_2 + e^-$.[16]

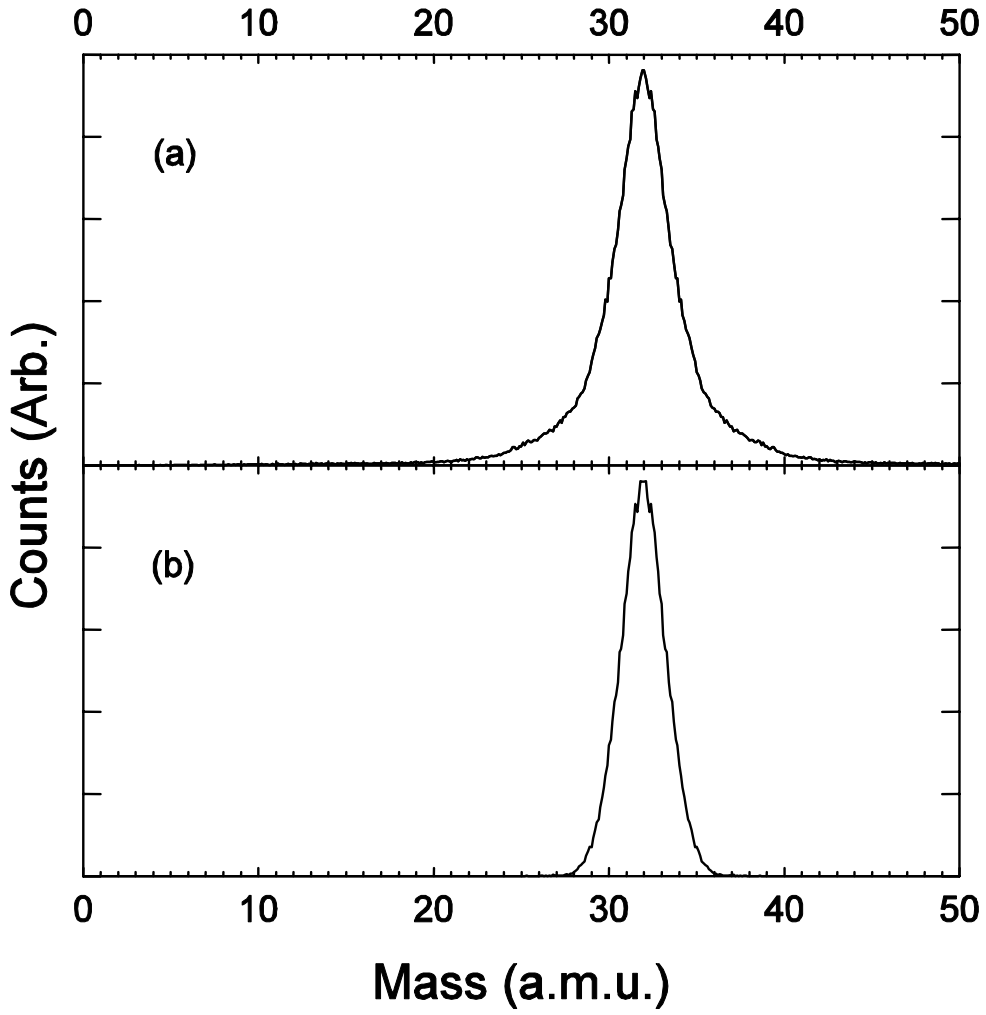

Figure 2-14: Photofragment mass spectra in the DPD of O_4^- at $E_{h\nu}$ = 2.33 eV: (a) without any centroid gating; (b) with a 2-mm-wide gate applied to each of the X, Y, and Z centroids.

Figure 2-14 demonstrates the effect of centroid gating by examination of the mass spectra of photofragments produced in the DPD of O_4^- at $E_{h\nu}$ = 2.33 eV. The spectrum in panel (a) includes all the data without centroid gating, showing a peak centered at 32 a.m.u. with a FWHM = 3.4 a.m.u. and extending to 19 and 45 a.m.u. A narrower peak with a FWHM of 2.5 a.m.u. and extending to 28 and 36 a.m.u. is observed in panel (b)

with a 2-mm-width centroid gate applied to all three dimensions, giving a mass resolution $m/\Delta m \approx 13$.

2.5 Conclusion

This chapter has described the basic principles of the fast-ion-beam photoelectron-photofragment coincidence spectrometer, the strategies for the data acquisition, and the procedures for detector calibration of the new FXDL detector. Coincidence measurements of the three dimensional velocities of the photoelectron and the photofragments from the same dissociative photodetachment event are accomplished using time- and position-sensitive detectors synchronized with the photodetachment laser pulse. The experimental results obtained using this spectrometer to study the dynamics of gas-phase transient species will be presented in the following chapters.

References

1 C. R. Sherwood, Ph.D. Thesis, University of California, San Diego, 1995.

2 K. A. Hanold, C. R. Sherwood, M. C. Garner, and R. E. Continetti, Rev. Sci. Instrum. **66**, 5507 (1995).

3 M. C. Garner, C. R. Sherwood, K. A. Hanold, and R. E. Continetti, Chem. Phys. Lett. **248**, 20 (1996).

4 R. E. Continetti, Int. Rev. Phys. Chem. **17**, 227 (1998).

5 D. L. Osborn, D. J. Leahy, D. R. Cyr, and D. M. Neumark, J. Chem. Phys. **104**, 5026 (1996).

6 J. M. B. Bakker, J. Phys. E-Sci. Instrum. **6**, 785 (1973).

[7] J. A. Davies, J. E. LeClaire, R. E. Continetti, and C. C. Hayden, J. Chem. Phys. **111**, 1 (1999).

[8] R. E. Continetti and C. C. Hayden, in *Modern Trends in Chemical Reaction Dynamics*, edited by X. Yang and K. Liu (World Scientific, Sigapore, 2004).

[9] L. S. Alconcel, Ph.D. Thesis, University of California, San Diego, 2002.

[10] C. Martin, P. Jelinsky, M. Lampton, R. F. Malina, and H. O. Anger, Rev. Sci. Instrum. **52**, 1067 (1981).

[11] K. A. Hanold, A. K. Luong, T. G. Clements, and R. E. Continetti, Rev. Sci. Instrum. **70**, 2268 (1999).

[12] D. R. Cyr, Ph.D. Thesis, University of California, Berkeley, 1993.

[13] D. P. deBruijn and J. Los, Rev. Sci. Instrum. **53**, 1020 (1982).

[14] C. R. Sherwood, M. C. Garner, K. A. Hanold, K. M. Strong, and R. E. Continetti, J. Chem. Phys. **102**, 6949 (1995).

[15] K. A. Hanold, C. R. Sherwood, and R. E. Continetti, J. Chem. Phys. **103**, 9876 (1995).

[16] C. R. Sherwood, K. A. Hanold, M. C. Garner, K. M. Strong, and R. E. Continetti, J. Chem. Phys. **105**, 10803 (1996).

[17] K. A. Hanold, M. C. Garner, and R. E. Continetti, Physical Review Letters **77**, 3335 (1996).

[18] K. A. Hanold and R. E. Continetti, Chemical Physics **239**, 493 (1998).

Chapter 3

Dynamics of the Acetyloxyl Radical Studied by Dissociative Photodetachment of the Acetate Anion

Oxygenated organic radicals are important in a number of complex environments. In the present work, the energetics and dynamics of the acetyloxyl radical formed by photodetachment of the acetate anion are studied. The acetyloxyl radical is a possible intermediate in the bimolecular collision of $CH_3O\cdot$ + CO,[1-3] an important process in atmospheric and combustion chemistry. In addition, carboxyl radicals $RCO_2\cdot$ play significant roles in synthetic organic chemistry. Two well-known examples are the Kolbe and Hunsdiecker reactions,[4] both involving the unimolecular reaction step in which $RCO_2\cdot$ radicals decompose into CO_2 and free radicals R·. Studies of the acetyloxyl radical, $CH_3CO_2\cdot$, can thus provide insights into detailed reaction mechanisms in organic synthesis and the role this radical may play in oxidation and combustion phenomena.

The lifetime of $CH_3CO_2\cdot$ and the reactivity of this radical or the decomposition product $CH_3\cdot$ have been of interest to organic chemists for years.[5-13] Previous studies have focused on the kinetics and thermodynamics of decarboxylation. Most of these experiments made use of the dissociation of acetyl peroxide $(CH_3CO_2)_2$, which produces $CH_3CO_2\cdot$ radicals followed by a subsequent dissociation to form $CH_3\cdot$ and CO_2. The reactive $CH_3\cdot$ radicals can then react with other species in the reaction environment. By measuring the kinetics of these reactions, Herk *et al*. estimated the unimolecular decarboxylation rate constant of $CH_3CO_2\cdot$ to be 10^9-10^{10} $sec.^{-1}$ with an activation energy of 5 kcal/mole.[5] A similar study by Braun *et al.* with a more detailed kinetic treatment

found a decomposition rate constant of 1.6×10^9 sec.$^{-1}$ at 60ºC, and an activation energy E_A = 6.6 kcal/mole.[14] Taking into account the heat of combustion and the dissociation energy of $(CH_3CO_2)_2$, a heat of formation $\Delta_f H°_{298K}$ = -45 ± 2 kcal/mol and a decarboxylation exothermicity of 17 ± 5 kcal/mole were predicted for the acetyloxyl radical.[15]

Using the appearance energy method, mass-spectrometric measurements by Holmes *et al.* reported the heat of formation for $CH_3CO_2\cdot$ to be $\Delta_f H°_{298\ K}$ = -51.7 ± 3 kcal/mol.[16] Experiments were also carried out to determine the electron affinity (EA) of $CH_3CO_2\cdot$. These include Yamdagni and Kebarle's study of ion equilibria,[17] electron-impact ion appearance energy studies by Tsuda *et al.*[18] and Muftakhov *et al.*,[19] and electron attachment measurements by Wentworth and coworkers.[20] Wang and coworkers have also carried out a photodetachment study on the acetate anion, yielding an adiabatic EA ≈ 3.4 eV.[21] All these reported EA values show good agreement within a range from 3.2 to 3.4 eV.

Theoretical predictions of the structure and potential energy surfaces are difficult for the acetyloxyl radical due to the existence of several low-lying electronic states and symmetry breaking from C_{2v} to C_s symmetry. [2,3,22-27] The most recent studies include the *ab initio* calculations of Armstrong and co-workers on the acetyloxyl radical using MP2 and G2(MP2)/6-31G(D) methods[25,26] and a density functional theory (B3PW91/aug-cc-pVdz) calculation by Kieninger *et al.*[27] In these studies two local minima were found, ^{2}A"(B_2) and ^{2}A'(A'), along with two transition states ^{2}A'(B_2) and ^{2}A'(A_1). The symmetry terms are given for the overall $CH_3CO_2\cdot$ radical (in C_s symmetry), and in parentheses, the

(a) **(b)**

Figure 3-1: Structures of the CH_3CO_2 radical. (a) One hydrogen atom lies in the plane of O-C-O group. (b) One hydrogen atom is in the plane bisecting O-C-O group.

symmetries of the molecular orbitals of the carboxyl group (-CO_2·) in either C_{2v} symmetry or C_s symmetry if the symmetry of that moiety is reduced by the pseudo-Jahn-Teller effect. The ^{2}A'(A') minimum and the ^{2}A'(B_2) transition state have one hydrogen atom lying in the plane of O-C-O [Figure 3-1 (a)]. The geometries of the ^{2}A"(B_2) minimum and the ^{2}A'(A_1) transition state, on the other hand, have one hydrogen located in the plane perpendicular to and bisecting the O-C-O plane [Figure 3-1(b)]. The relative energies of these states vary considerably with the level of theory used, but the highest level *ab initio* results from Armstrong and co-workers indicate that the ground state is the ^{2}A"(B_2) state, with the ^{2}A'(A') state lying 0.1 eV higher at the G2(MP2) level of theory. The acetate anion is a closed-shell system, previously studied by Yu *et al.* at the MP2/6-31G(d) level,[26] with a ^{2}A'(A') ground state, with an O-C-O bond angle of 130° compared to 121° for the analogous state in the radical. Armstrong and co-workers suggest that rotation about the C-C bond in the acetyloxyl radical may lead to CH_3· + CO_2 products with little or no barrier on the ^{2}A'(A_1) surface.

The formyloxyl radical HCO_2· is the simplest analog of CH_3CO_2· and provides similar challenges for accurate calculations of its structure and energetics.[23,25-27] Unlike the lack of experimental results on CH_3CO_2·, however, photoelectron and photoelectron-

photofragment coincidence (PPC) spectroscopy experiments on the formate anion HCO_2^- have provided insights into the electronic and vibrational structure of the $HCO_2\cdot$ radical and the dissociation dynamics of $HCO_2\cdot \rightarrow H + CO_2$.[28,29] In order to obtain spectroscopic and dynamics data on the $CH_3CO_2\cdot$ radical, in the current work PPC spectroscopy was applied to study the dissociative photodetachment (DPD) of the acetate anion $CH_3CO_2^-$ and its deuterated form $CD_3CO_2^-$ in the gas phase. With different photon energies, the exploration of the low-lying electronic states of $CH_3CO_2\cdot$ is possible, while experiments carried out near the photodetachment threshold yield high-resolution photoelectron spectra. Near-threshold measurements of the PPC spectra at 355 nm (3.49 eV) are reported along with an above-threshold measurement at 257 nm (4.82 eV). The branching between stable radicals and dissociation of the nascent $CH_3CO_2\cdot$ radical is presented, along with a discussion of the mechanism and dissociation dynamics of $CH_3CO_2\cdot$.

3.1 Experiment

The fast-ion-beam photoelectron-photofragment spectrometer used in this work has been previously described[30-32] and only the essential elements will be reviewed here. Room temperature vapor of 20% acetic acid or deuterated acetic acid [prepared from CD_3CO_2D (99.5%, Cambridge Isotope Laboratory) and D_2O (99.9 atom %, Aldrich)] in aqueous solution was seeded in N_2O/Ar (~13% N_2O, ~87% Ar) and expanded through a 0.25 mm diameter nozzle pulsed at 1 kHz with a piezoelectric valve. A pulsed electric discharge was used to produce negative ions. The O^- produced by dissociative electron attachment to N_2O abstracted a proton from acetic acid, yielding the acetate anion. The fast ion beam of $CH_3CO_2^-$ (m/e = 59) or $CD_3CO_2^-$ (m/e = 62) at energies of 3 and 6 keV

was mass-selected by time-of-flight (TOF) and perpendicularly intersected with linearly polarized laser pulses. Two different laser wavelengths were used: 355 nm (3.494 eV) generated by the third harmonic of an Nd:YAG laser (~100 ps FWHM, Quantronix Model 116) and 257 nm (4.82 eV) from the third harmonic of a Ti:Sapphire laser (1.8 ps FWHM, Clark CPA 2000).

The full 4π sr solid angle of photoelectrons was collected by a space-focusing electron optics assembly first developed by Hayden and coworkers.[33] In the 257 nm experiments, the photoelectrons were extracted by a pulsed electric field of 8.9 V/cm toward the detector. In the near-threshold 355 nm experiments, a lower electric field of 1.0 V/cm was applied in order to achieve better resolution. The center of mass (CM) electron kinetic energies (eKE) and laboratory frame photoelectron angular distributions were calculated from the recorded time- and position-of-arrival of the photoelectrons. The *z* velocity component of photoelectrons, perpendicular to the photoelectron detector face and derived from the photoelectron TOF, was the major factor limiting the resolution. To minimize this problem, a slice of the three dimensional photoelectron distribution with small *z* velocity components in the CM is analyzed and the resulting photoelectron intensity distribution is corrected based on the cylindrical symmetry about the electric vector of the laser.[34] This required the photoelectron data to be recorded with the laser electric vector along the direction of the ion beam, parallel to the face of the photoelectron detector. The resulting energy resolution is $\Delta E/E \approx 12\%$ (FWHM) as determined by the photodetachment of I^- at 257 nm. To reduce laser-generated photoelectron background in the 257 nm experiments, only those electrons coincident with at least one photofragment or the stable neutral product were collected.

Undetached anions were deflected out of the beam into a microchannel-plate-based ion detector. The stable free radicals and neutral photofragments formed by photodetachment were detected by a 4-cm-diameter two-particle time- and position-sensitive detector, with a 7 mm diameter beam block at the center.[30] By adjusting the vertical position of the neutral particle detector, the ion beam can be either centered on the beam block or off-centered on one of the two detector halves. In the centered case, only photofragments with sufficient recoil velocities to clear the beam block are detected. In the off-centered case, photofragments recoiling along the ion beam and non-dissociative stable radicals are detectable. Conservation of linear momentum between the coincident photofragments determines the product mass ratio and the CM kinetic energy release, E_T, for the dissociation event. The detector acceptance function (DAF) for detecting coincident photofragments with the neutral particle detector is a function of the kinetic energy of the ion beam, the mass ratios of the dissociation products, the translational energy release during the dissociation, and the position of the detector. Numeric correction for the DAF has been previously derived and is used here to convert the measured $N(E_T)$ distributions into product translational energy $P(E_T)$ distributions. [35] The dissociative photodetachment $O_4^- + h\nu \rightarrow O_2 + O_2 + e^-$ at 257 nm was used for calibration, yielding a resolution of $\Delta E_T/E_T \approx 10\%$.

3.2 Results

3.2.1 Photoelectron Spectra

The photoelectron kinetic energy spectrum of acetate anion recorded at 3.494 eV (355 nm) is shown in Figure 3-2(a). As discussed in the experimental section, this

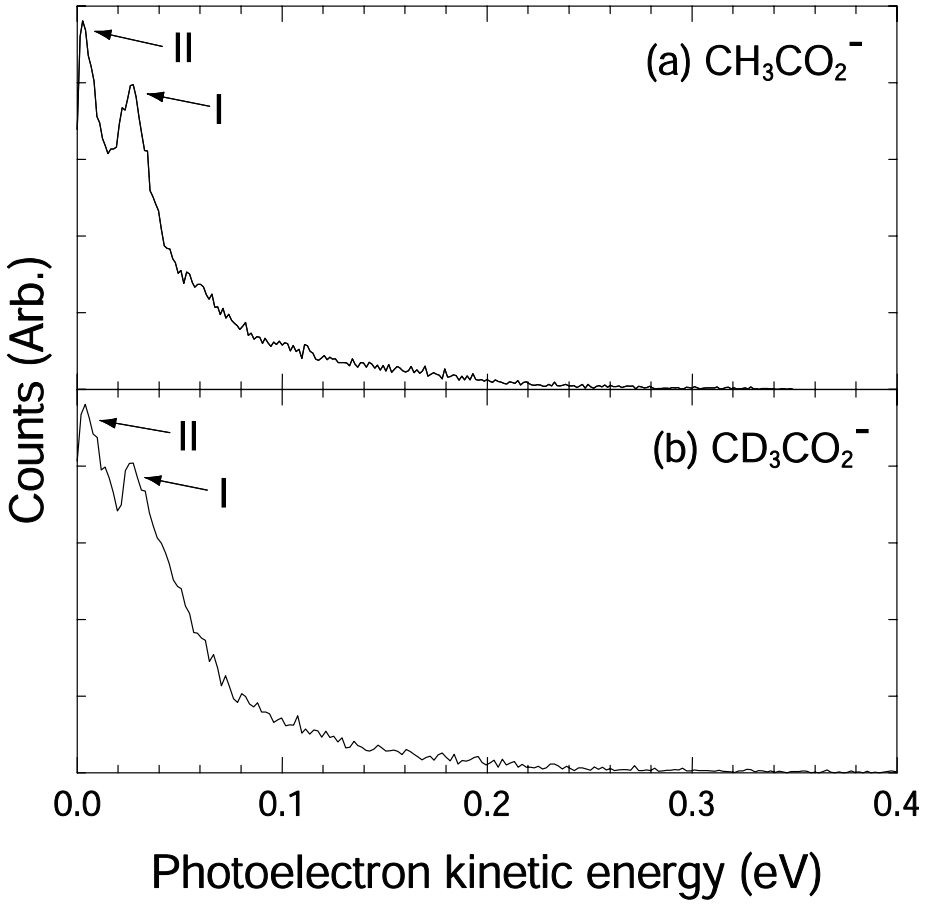

Figure 3-2: Near-threshold photoelectron spectra of (a) $CH_3CO_2^-$ and (b) $CD_3CO_2^-$ at 355 nm (3.49 eV). The position of peak I is used to calculate the upper limit of adiabatic EA of $CH_3CO_2\cdot$ and $CD_3CO_2\cdot$.

spectrum represents the probability of photoelectrons P(eKE) integrated over the full 4π sr. A narrow distribution near eKE = 0.0 eV is observed, indicating that this photon energy is close to the photodetachment threshold. Two peaks are observed in the spectrum, one at 0.003 eV, and the other at 0.026 eV [peak I in Figure 3-2(a)]. In order to reveal the origin of the 0.023 eV (185 cm^{-1}) energy spacing, the P(eKE) spectrum of the deuterated acetate anion, $CD_3CO_2^-$ [Figure 3-2(b)] was collected under the same experimental conditions. The two spectra have nearly identical features, indicating that

the observed structure is not related to C-H vibrational modes and that zero-point energy differences between the anion and neutral radical nearly cancel. Assuming that the peak at 0.026 eV is the electronic origin, an upper limit to the adiabatic electron affinity (AEA) is found to be 3.47 ± 0.01 eV, in good agreement with the lower resolution experiments of Wang and coworkers.[21] The precision of ± 0.01 eV in this case refers to the measurement itself – the assignment will be discussed further in Sections 3.3.1 and 3.3.2 below. The photoelectron images recorded at 355 nm are not shown here, but are consistent with *s*-wave photodetachment with a nearly isotropic angular distribution near threshold.

A high-energy tail extending above 0.2 eV is seen in both of the P(eKE) spectra in Figure 3-2, however, which is likely to arise from photodetachment of vibrationally excited anions. The acetate anions in this experiment were generated in a pulsed discharge, with vibrational temperatures expected to be 300K or greater. A RB3LYP/aug-cc-pVDZ calculation of the vibrational frequencies in the anion was carried out. Using the calculated vibrational frequencies the vibrational partition function was evaluated indicating that a tail of this magnitude can arise from a vibrational temperature of ≈ 400K, ignoring any Franck-Condon effects, consideration of which are beyond the scope of the present work given the complexity of the electronic structure of the acetyloxyl radical. The observed high-energy tail suggests that the upper bound for the EA = 3.47 ± 0.01 eV can be no more than 0.2 eV too high.

The P(eKE) spectrum of $CH_3CO_2^-$ obtained at a photon energy of 4.82 eV (257 nm) is shown in Figure 3-3. Since the photon energy of 4.82 eV is no longer near threshold, the eKE resolution is worse and the fine structure observed in the 3.49 eV

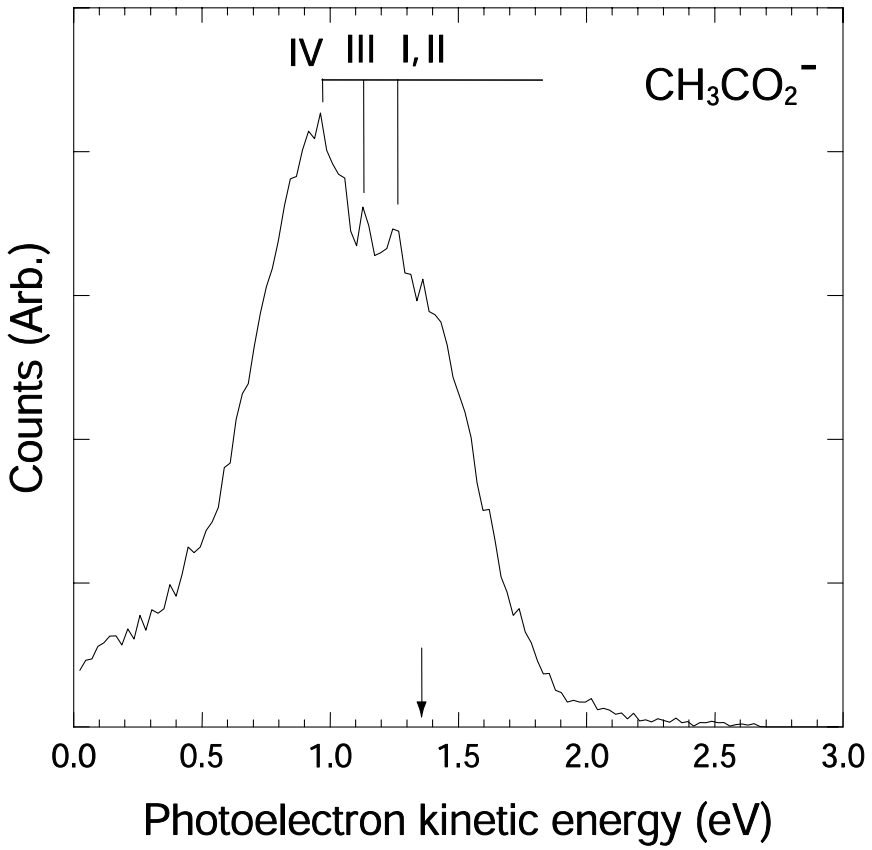

Figure 3-3: Photoelectron spectrum of $CH_3CO_2^-$ at 257 nm (4.82 eV). The arrow points to EA determined from Figure 3-2.

spectra in Figure 3-2 is not seen here. However, two new poorly resolved features are observed when compared with the spectrum at 3.49 eV: 1.14 eV (peak III in Figure 3-3) and 0.94 eV (peak IV), while the third feature at 1.30 eV is consistent with the near-threshold photodetachment observed at E_{hv} = 3.49 eV. Comparison of Figures 3-2 and 3-3 shows the eKE spectrum taken at 257 nm is significantly broadened due to the loss of resolution at high eKE. The assignment of the features (III) and (IV) must be taken as tentative given the signal-to-noise of the measurement. The photoelectron images

recorded at 257 nm are not reported here, but indicate that the photoelectron angular distribution peaks perpendicular to the laser electric vector at this wavelength.

3.2.2 Photofragment Spectra

The time-of-flight (TOF) spectra of the resultant neutral particles after photodetachment of the acetate anion at E_{hv} = 3.49 eV are shown in Figure 3-4. The ion beam was set off-center on the neutral particle detector for this measurement. The photofragment TOF spectra at E_{hv} = 4.82 eV are not presented here because they are very similar to the spectra in Figure 3-4. The abscissa is the time of arrival of the neutral particles relative to the TOF of the center-of-mass at zero. Negative TOF corresponds to particles recoiling forward in the direction of the ion beam velocity and positive TOF corresponds to particles recoiling backward. These fast ion-beam TOF spectra are analogous to the Doppler spectra frequently measured in optical studies of reaction dynamics. [36,37] The sharp peak at 0 ns in the TOF spectra in Figure 4 results from a stable neutral radical with the empirical formula $C_2H_3O_2$. The broad feature around the $C_2H_3O_2$ peak result from CO_2 molecules produced in the dissociation of the $CH_3CO_2\cdot$, while the smaller wings at larger positive and negative TOF are from lighter $CH_3\cdot$ radical products scattered forward and backward along the beam. In Figure 3-4 the CO_2 peaks are significantly higher than $CH_3\cdot$ peaks and an asymmetry in peak heights is also seen when comparing the peaks at negative TOF with those at positive TOF. This is a result of the finite DAF for detection of the dissociation products of $CH_3CO_2\cdot$ at this beam energy. The relatively large E_T and the mass of $CO_2/CH_3\cdot$ = 44/15 results in most of the $CH_3\cdot$ products recoiling out of the beam and missing the neutral particle detector.

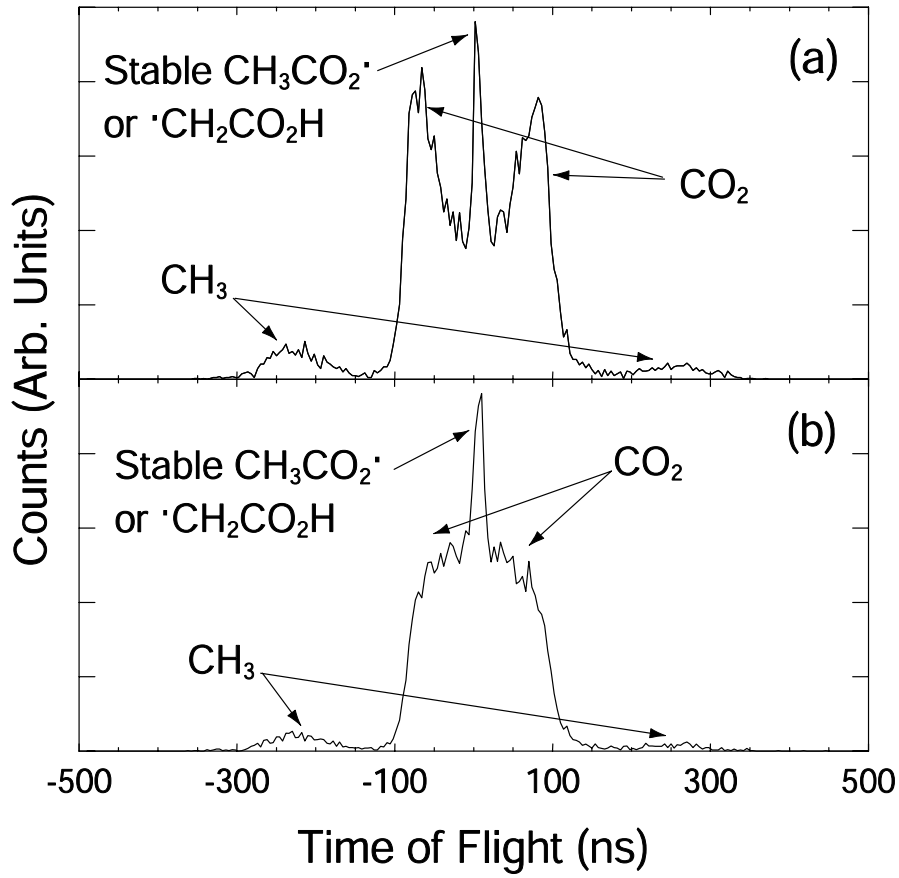

Figure 3-4: Time-of-flight (TOF) spectra of neutral products in photodetachment of $CH_3CO_2^-$ at 355 nm (3.49 eV). (a) Electric vector of laser parallel to the direction of ion beam (perpendicular to the face of neutral particle detector); (b) electric vector of laser perpendicular to the direction of ion beam (parallel to the face of neutral particle detector). The abscissa here is the relative TOF with zero as the TOF of undissociated CH_3CO_2· (or ·CH_2CO_2H).

Similarly, the particles at negative TOF have larger laboratory velocities and recoil less out of the beam before reaching the detector and are thus detected with higher efficiency. The branching ratio between stable $C_2H_3O_2$ radical and dissociation products is ≈ 1:9 based on measuring the relative intensities of the CO_2 and stable radical peaks in Figure

3-4 under the assumption that the detection efficiencies are equal for both particles that strike the detector. TOF spectra of $C_2D_3O_2$ radicals gave similar results, indicating that the branching between stable radicals and dissociation products is not sensitive to isotopic substitution of deuterium for hydrogen.

Comparison of Figures 3-4(a) and 3-4(b) shows that the dissociation products are more separated in TOF when the laser $\vec{E}$ vector is along the ion beam. This anisotropic photofragment angular distribution implies that rupture of the carbon-carbon bond occurs promptly on the time scale of molecular rotation. As discussed by Zare and others,[38] the photofragment angular distribution in the electric-dipole approximation is given by

$$I(E_T,\theta) = \frac{\partial\sigma(E_T)}{\partial\Omega} = \frac{\sigma_{tot}}{4\pi}[1+\beta(E_T)\bullet P_2(\cos\theta)] \qquad (3\text{-}1)$$

where σ_{tot} is the total photodissociation cross section, θ is the polar angle between the photofragment recoil and the laser electric vector $\vec{E}$, $P_2(\cos\theta)$ is the second-order Legendre polynomial in $\cos\theta$, and $\beta(E_T)$ is an energy-dependent anisotropic parameter, ranging between -1 and 2. Fitting the photofragment angular distributions and the time-of-flight spectra following correction for the DAF[35] shows an energy-averaged anisotropy parameter $\beta \approx 1.2 \pm 0.2$, corresponding to a predominantly $\cos^2\theta$ distribution. This shows that DPD of the acetate anion yields an anisotropic photofragment angular distribution, similar to the direct DPD of O_4^- previously studied in this laboratory. [39]

The DAF-corrected translational energy release distributions, $P(E_T)$, for the DPD of $CH_3CO_2^-$ and $CD_3CO_2^-$ at both $E_{h\nu}$ = 3.49 eV and 4.82 eV are plotted in Figure 3-5. At $E_{h\nu}$ = 3.49 eV, $P(E_T)$ for $CH_3CO_2^-$ peaks at 0.65 eV [Figure 3-5(a), dashed line], with a relatively narrow distribution. In DPD at $E_{h\nu}$ = 4.82 eV, the $P(E_T)$ [solid line in Figure 3-

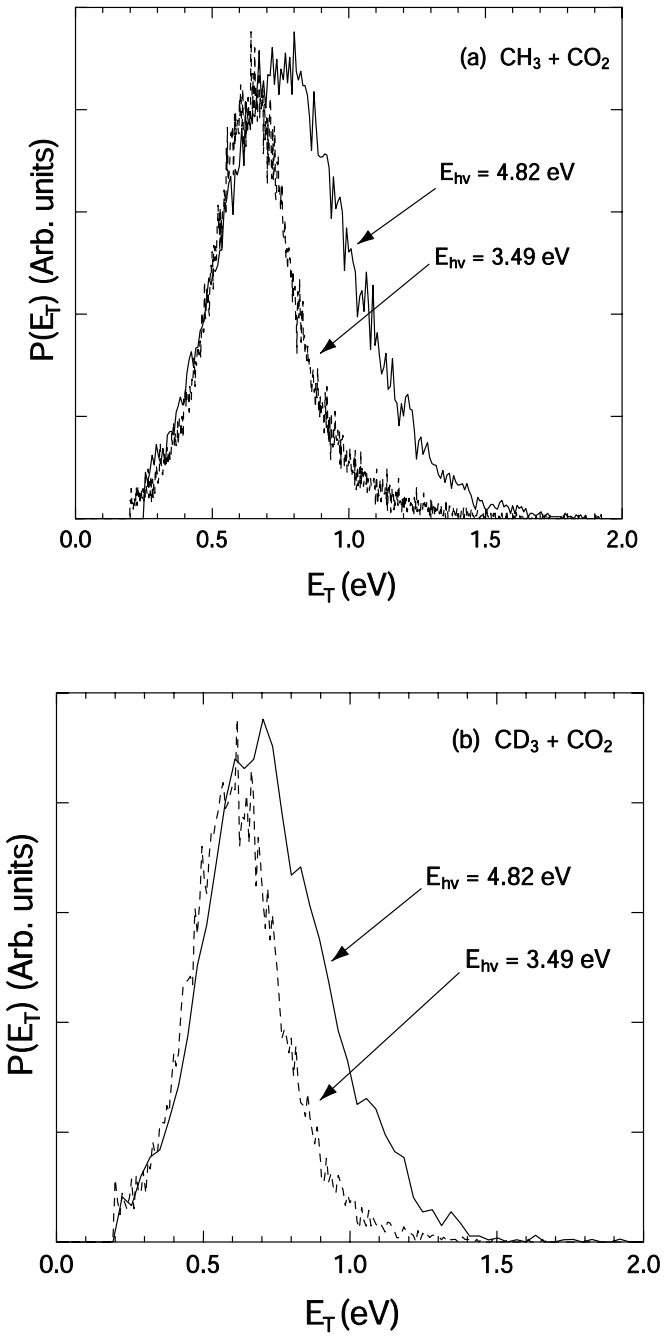

Figure 3-5: Translational energy release spectra, $P(E_T)$, of the photofragments in the dissociative photodetachment of (a) $CH_3CO_2^-$; (b) $CD_3CO_2^-$. The solid lines in both (a) and (b) represent the $N(E_T)$ recorded at 257 nm (4.82 eV). The dashed lines represent $N(E_T)$ at 355 nm (3.49 eV).

5(a)] is nearly the same on the low-energy side as the 3.49 eV distribution, however, at high E_T in the 4.82 eV distribution, $P(E_T)$ is broader, and the peak shifts to 0.80 eV. The translational energy distribution for the DPD of $CD_3CO_2^-$ shown in Figure 3-5(b) is similar, with the distribution shifted to lower E_T at both wavelengths compared with the $CH_3CO_2^-$ data: $P(E_T)$ peaks at 0.60 eV at E_{hv} = 3.49 eV and 0.69 eV at E_{hv} = 4.82 eV, respectively.

3.2.3 Photoelectron-Photofragment Correlation Spectra

The unique feature of our apparatus is that it allows the coincident measurement of the photoelectron and photofragments, revealing the partitioning of the available kinetic energy among the products. One interesting observation is that the P(eKE) spectra measured in coincidence either with only the stable $C_2H_3O_2$ radical or with only the $CH_3\cdot$ + CO_2 products are indistinguishable within the signal-to-noise ratio of the measurement. This phenomenon will be discussed in detail in section 3.3.1 below. Figure 3-6 shows the photoelectron-photofragment kinetic energy correlation spectra, $N(eKE,E_T)$, as two-dimensional gray-scale histograms in which the intensity of each point represents the number of events with specific eKE and E_T values in the DPD of $CH_3CO_2^-$. On the left and the bottom of each correlation spectrum are the raw N(eKE) and $N(E_T)$ spectra, respectively. These spectra are uncorrected for any DAF effects and are obtained by integrating over the complementary variables in the two-dimensional correlation spectrum. The N(eKE) spectrum for E_{hv} = 4.82 eV seen in Figure 3-6(b) exhibits a different intensity distribution than the higher-resolution sliced and DAF-corrected P(eKE) spectrum shown in Fig. 3-3. This occurs because it is not possible to

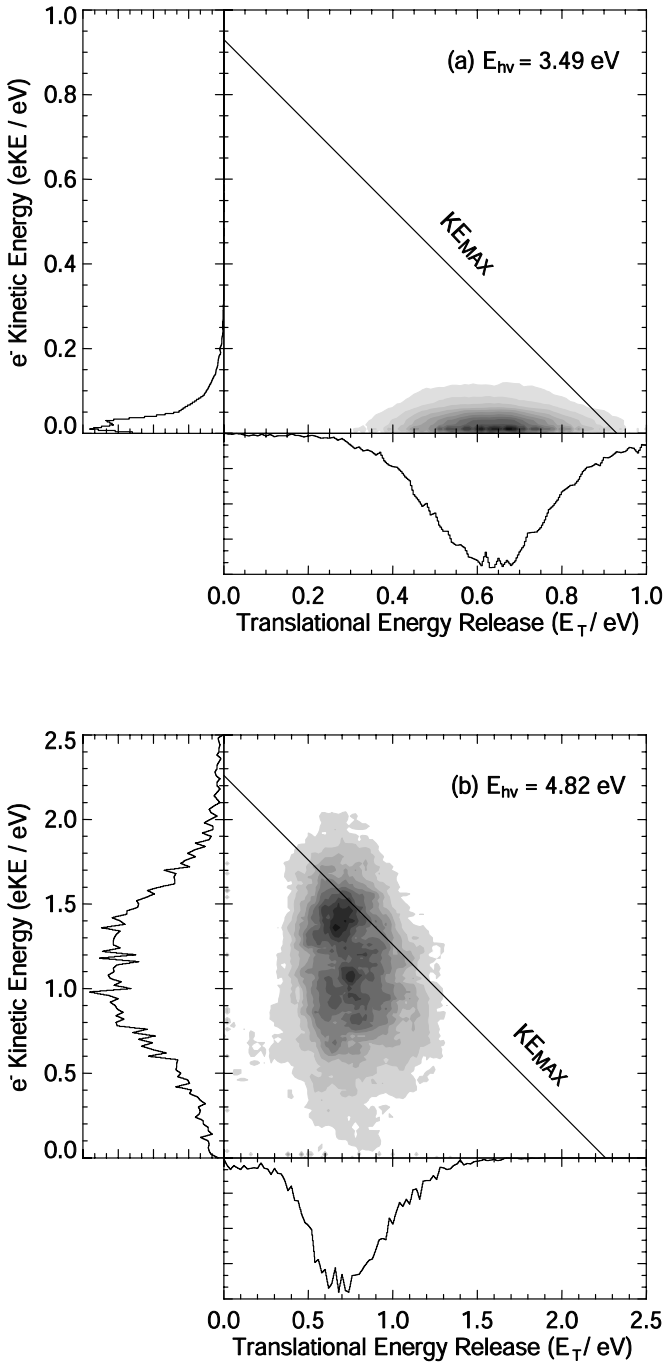

Figure 3-6: Photoelectron-photofragment translational energy correlation spectra, $N(E_T, eKE)$, of $CH_3CO_2^-$ at (a) 355 nm (3.49 eV); (b) 257 nm (4.82 eV). The photoelectron N(eKE) spectra are shown along y-axis and the photofragment $N(E_T)$ spectra are shown along the x-axis. The diagonal lines represent KE_{MAX} at E_{hv} = 3.49 eV as described in the text.

carry out the DAF-correction for the photoelectrons in the correlated data, so the resolution is reduced and the intensity distribution is altered. The experimental value for the maximum kinetic energy release (KE_{MAX}) for all products in the DPD reaction ($CH_3CO_2^- + h\nu \rightarrow CH_3\cdot + CO_2 + e^-$) is typically determined from the contour at 5% of the peak, representing the level of false coincidences expected in the experiment.[30] The value of $KE_{MAX} = 0.93 \pm 0.05$ eV obtained from the higher-resolution near-threshold photodetachment data at $E_{h\nu} = 3.49$ eV is shown by the diagonal line in Figure 3-6(a). In Figure 3-6(b), the $E_{h\nu} = 4.82$ eV data is shown, along with $KE_{MAX} = 2.26 \pm 0.05$ eV, as derived from the data in Figure 3-6(a) and the photon energy difference. As Figure 3-6(b) shows, this value of KE_{MAX} cuts through a significant fraction of the data, as a result of the much lower N(eKE) resolution this far above threshold. The KE_{MAX} value of 0.93 eV obtained from the near-threshold photodetachment at $E_{h\nu} = 3.49$ eV is the most reliable and shows that 2.56 eV is required to dissociate $CH_3CO_2^- \rightarrow CH_3\cdot + CO_2 + e^-$.

At a photon energy of 3.49 eV, all events in the correlation spectrum are compressed at the bottom owing to the small distribution of eKE. In the correlation spectrum when $E_{h\nu} = 4.82$ eV, there are two regions corresponding to the two broad features in the N(eKE) spectrum with slightly different translational energy release, E_T [Figure 3-6(b)]. The region with larger eKE corresponds to the peak at 1.30 eV in the N(eKE) spectrum recorded at the same photon energy. The other region corresponds to the features at eKE = 0.94 and 1.14 eV. These lower eKE features arise from new electronic states accessed at $E_{h\nu} = 4.82$ eV, and lead to the larger E_T release seen in the high-energy tail on the $P(E_T)$ spectra at this photon energy in Figure 3-5. The total kinetic energy, $KE_{total} = eKE + E_T$, is smaller for the lower eKE features, implying that the

$CH_3\cdot + CO_2$ formed by dissociation of these new electronic states are more vibrationally and/or rotationally excited since there are no low lying electronic states of the products.

3.3 Discussion

The spectra presented here provide insights into the energetics and dynamics of the $CH_3CO_2\cdot$ radical formed in the photodetachment of $CH_3CO_2^-$. In section 3.3.1, possible mechanisms are suggested based on the PPC spectra and TOF of the neutral products. The energetics of the nascent $CH_3CO_2\cdot$ radical from the P(eKE) spectra and comparison with theoretical predictions are discussed in section 3.3.2. In section 3.3.3, an impulsive model is applied to interpret the energy partitioning among the dissociation products. Finally, the possibility of ionic photodissociation channels competing with DPD is considered.

3.3.1 Reaction Mechanism

The TOF spectra of the neutral particles in Fig. 3-4 reveal two channels after the photodetachment of the $CH_3CO_2^-$: dissociation into $CH_3\cdot + CO_2$ and a minor channel yielding the stable radical $C_2H_3O_2\cdot$. The two most likely structures of $C_2H_3O_2\cdot$ radical are the acetyloxyl radical, $CH_3CO_2\cdot$ and the carboxyl-methyl radical isomer $\cdot CH_2CO_2H$. The present experiments cannot distinguish between these two isomers, but provides the first direct evidence that stable radicals can be produced by photodetachment of the acetate anion in the gas phase. This result contradicts previous suggestions that all the $CH_3CO_2\cdot$ radicals dissociate on ns time-scales.[5] Thus, in some combustion and organic synthesis processes, not only $CH_3\cdot$, but also the non-dissociative $CH_3CO_2\cdot$ or $\cdot CH_2CO_2H$

radicals may play roles in the reaction mechanisms and kinetics. It is also possible that in condensed phase environments, the nascent $CH_3CO_2\cdot/\cdot CH_2CO_2H$ radical is stabilized. In the experiments at a beam energy of 3 keV, it takes approximately 10 μs for $C_2H_3O_2$ to travel from the interaction region to the neutral particle detector, providing a lower limit for the lifetime of the stable $C_2H_3O_2$ radical of ~10 μs under collision-free conditions.

As mentioned in section 3.2.3 above, the P(eKE) spectra measured in coincidence either with only stable $C_2H_3O_2$ radicals or with only the $CH_3\cdot + CO_2$ products are indistinguishable within the signal-to-noise of the measurement. This implies that instead of a transition directly from the acetate anion to a repulsive potential surface of the neutral radical, the removal of one electron from $CH_3CO_2^-$ places the $CH_3CO_2\cdot$ radical into some intermediate state(s). Following the production of the nascent $CH_3CO_2\cdot$, the system rapidly (faster than molecular rotation) evolves to either produce the stable $CH_3CO_2\cdot/\cdot CH_2CO_2H$ radical or the dissociation products. Given the small branching ratio to stable radicals, we cannot unambiguously say at this time whether or not there is some internal energy dependence in the product branching process, but there is no gross dependence. If the observed stable radical is $CH_3CO_2\cdot$, the intermediate species may be one of the transition states or low-lying excited states theoretically predicted for this species, as reviewed in the introduction:

$$CH_3CO_2^- + h\nu \rightarrow CH_3CO_2\cdot^* + e^- \rightarrow CO_2 + CH_3\cdot + e^- \qquad (90\%)$$

$$\downarrow$$

$$CH_3CO_2\cdot + e^- \qquad (10\%)$$

Formation of the isomeric stable radical $\cdot CH_2CO_2H$ from the nascent $CH_3CO_2\cdot$ is also possible. Although the barrier of an intramolecular hydrogen atom transfer

Table 3-1: Energetics data [a]

	Relative Energy (eV)	**Ref.**
$CH_3CO_2^-$	0.00±0.14	*b*
$CH_3CO_2\cdot$ (I) + e^-	3.47±0.01	
$CH_3CO_2\cdot$ (II) + e^-	3.49±0.01	
$CH_3CO_2\cdot$ (III) + e^-	3.68±0.1	
$CH_3CO_2\cdot$ (IV) + e^-	3.88±0.1	
$CH_3\cdot + CO_2 + e^-$	2.56±0.05	
	2.67±0.14	*b*
$^-CH_2CO_2H$	0.86±0.2	*c*
$\cdot CH_2CO_2H + e^-$	2.64±0.2	*d*
$CH_3\cdot + CO_2^-$	3.16±0.2	*e*
$CH_3^- + CO_2$	2.48±0.06	*f*

a. All values listed are relative energies using the ground state of $CH_3CO_2^-$ as reference level; *b.* Ref. [40]; *c.* Ref. [41]; *d.* Ref. [42]; *e.* This value is determined by the energy level of $CH_3\cdot + CO_2 + e^-$ measured in this work and the EA of CO_2 from Ref. [43]; *f.* This value is determined by the energy level of $CH_3\cdot + CO_2 + e^-$ measured in this work and the EA of CH_3 from Ref. [44].

forming $\cdot CH_2CO_2H$ radical from $CH_3CO_2\cdot$ is still unknown, this process is energetically favorable,[27,42] with an energy difference of ~0.8 eV between the lowest state of $CH_3CO_2\cdot$ observed in this work and $\cdot CH_2CO_2H$ reported in ref. [40] (See Table 3-1 and Figure 3-7). Direct production of the $\cdot CH_2CO_2H$ radical from photodetachment of the isomeric anion $CH_2CO_2H^-$ is unlikely on energetic grounds since the EA ≈ 1.9 eV for the $\cdot CH_2CO_2H$ radical[19] is inconsistent with the P(eKE) spectra presented. Thus, the $\cdot CH_2CO_2H$ radical can only originate from the isomerization process: $CH_3CO_2\cdot \rightarrow \cdot CH_2CO_2H$. The observation that the branching ratio between stable radicals and dissociation products is not sensitive to deuteration indicates that if isomerization

occurs, it must happen after formation of a metastable state of the $CH_3CO_2\cdot/CD_3CO_2\cdot$ radical as opposed to directly competing with the prompt dissociation channel.

This model, photodetachment to an intermediate state, followed by a rapid evolution to either one or more stable product(s) and a dissociative final state can explain the apparently conflicting phenomena observed — the existence of the stable $C_2H_3O_2$ radical with a lifetime longer than 10 μs and the anisotropic photofragment angular distribution indicative of a prompt decarboxylation process occurring in much less than a molecular rotational period. Although the preponderance of the radicals end up on the dissociative surface, some of them find at least a metastable state and possibly undergo an isomerization to the more stable carboxyl-methyl radical, $\cdot CH_2CO_2H$. This model needs the verification of reliable calculations that are beyond the scope of the present study.

3.3.2 Energetics and Dissociation Mechanism of the $CH_3CO_2\cdot$ Radical

Threshold photodetachment at $E_{h\nu}$ = 3.49 eV provides a high-resolution P(eKE) spectrum which is helpful to resolve the low-lying excited states of $CH_3CO_2\cdot$. As mentioned in Section 3.2.1, the P(eKE) spectra are nearly identical for $CH_3CO_2^-$ and $CD_3CO_2^-$, indicating the fine structure obtained at $E_{h\nu}$ = 3.49 eV does not originate from C-H vibrations. Moreover, the energy spacing of 0.023 eV (~185 cm^{-1}) is close to none of the vibrational frequencies of the $CH_3CO_2\cdot$ calculated by Rauk, *et al.* [25] and known vibrational energy levels of acetic acid, CH_3CO_2H.[45] As discussed in the introduction there is a significant change in O-C-O bending angle expected on photodetachment,

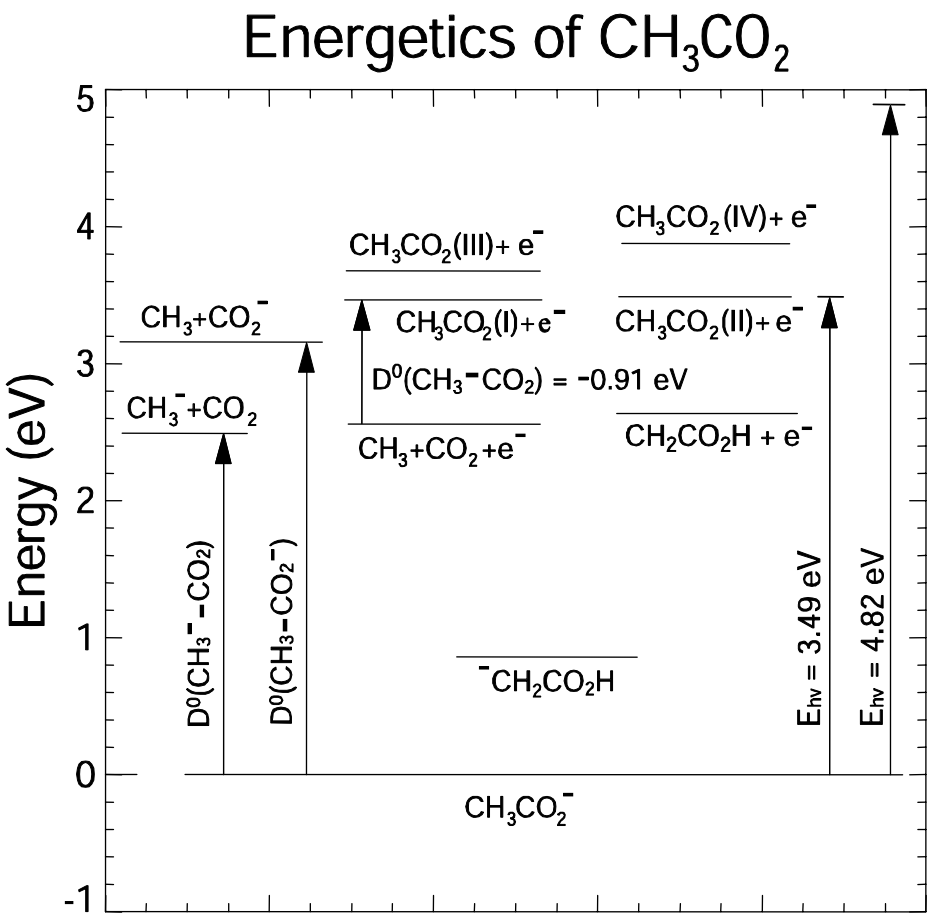

Figure 3-7: Energetics of the dissociative photodetachment of $CH_3CO_2^-$ in eV, relative to the ground state of $CH_3CO_2^-$. The energy of the CH_3 + CO_2^- channel is determined by the EA CO_2,[43] and the energy of CH_3^- + CO_2 is determined from the EA of CH_3[44] and the energetics for the DPD yielding $CH_3\cdot$ + CO_2 + e^- measured in this work. The energy of $\cdot CH_2CO_2H$ is obtained from Ref. [42] and energy of $^-CH_2CO_2H$ from Ref. [41].

however, the O-C-O bend in the acetyloxyl radical is predicted to be on the order of 600 cm^{-1} by comparison with the acetate anion and formyloxyl radical.[28] A likely explanation for these resolved features is that two nearly degenerate electronic states are produced.

This is supported by Neumark and coworkers' photodetachment study on the formate anion, HCO_2^-,[28] in which they reported the energy spacing between the ground and first electronic states to be 0.027 eV. It is also possible that some of the original acetate anions are vibrationally excited so the observed energy spacing could be the combination of the vibrational frequencies in the $CH_3CO_2^-$ and neutral $CH_3CO_2\cdot$ radicals. Although we cannot completely rule out this possibility, it is not likely because the fine structure was found unchanged even when different ion source conditions were employed. These two energy states, together with the two higher-lying states tentatively inferred from the P(eKE) spectrum at the photon energy of 4.82 eV, are shown in the Table 3-1 and in the energy diagram in Figure 3-7. The observed electron affinity of $CH_3CO_2\cdot$ is larger than the older values calculated from the previously reported heat of formation data of $CH_3CO_2\cdot$ discussed in the introduction,[15,16] but is consistent with the lower resolution photoelectron spectroscopy measurements of Wang and co-workers.[21]

As discussed in the introduction, the electronic structure of the $CH_3CO_2\cdot$ radical is complex owing to the presence of the O-C-O moiety, and is analogous to the well-studied $HCO_2\cdot$ radical. As discussed by Rauk *et al.*,[23,25,27] the lowest energy minimum for the $CH_3CO_2\cdot$ radical is $^2A''(B_2)$ [Figure 3-1(b)], while a transition state, $^2A'(B_2)$ [Figure 3-1(a)], separates the two symmetric $^2A''(B_2)$ geometries when the CH_3 group rotates about the C-C bond. Another minimum $^2A'(A')$ [Figure 3-1(a), but with the O-C-O moiety distorted from C_{2v} symmetry] is separated from the dissociation products $CH_3\cdot + CO_2$ by the transition state $^2A'(A_1)$ (Figure 1-b). At the G2(MP2)/6-31G(D) level, Rauk *et al.* found the $^2A''(B_2)$ and $^2A'(A')$ minima to be separated by 0.1 eV, nearly degenerate as are the two resolved peaks in the P(eKE) spectra. These are presumably the two states we

are observing, however, an unambiguous assignment of the ground state is not possible at this time.

The previous geometry optimization of the acetate anion by Yu *et al.* using MP2/6-31G(D) shows the minimum for $CH_3CO_2^-$ is similar to the $^2A'(A')$ minimum of the $CH_3CO_2\cdot$ radical in Figure 3-1(a).[26] A DFT calculation (RB3LYP/aug-cc-pvdz) we carried out, on the other hand, indicates that the $CH_3CO_2^-$ minimum has a geometry similar to Figure 3-1(b), with one H-C-C bond perpendicular to the O-C-O bond. These conflicting results are consistent with the observation that the torsional motion of the $CH_3\cdot$ group in the $CH_3CO_2^-$ anion was found to have nearly no barrier in our DFT calculations. Thus, it is possible that anion photodetachment projects onto both of the low-lying states of the $CH_3CO_2\cdot$ radical in accordance with the Franck-Condon principle. Armstrong and co-workers suggest that rotation of the methyl radical about the C-C bond can lead to rapid dissociation to $CH_3\cdot + CO_2$ via the $^2A'(A_1)$ transition state. Potential energy surfaces derived from high-level multireference configuration interaction calculations would be helpful for a Franck-Condon simulation of the P(eKE) spectra and further examination of the dissociation mechanism.

3.3.3 Dissociation Dynamics

The KE_{MAX} value shown on the photoelectron-photofragment correlation spectra defines the maximum available energy partitioned into the translational degrees of freedom of the photoelectron and two photofragments in a DPD event, which can be calculated by:

$$KE_{MAX} = h\nu - \Delta H^{\circ}_{f,0K}(CH_3\cdot) - \Delta H^{\circ}_{f,0K}(CO_2) + \Delta H^{\circ}_{f,0K}(CH_3CO_2^-) \quad (3\text{-}2)$$

In equation (2) $\Delta H^{\circ}_{f,0K}$ is the standard enthalpy of formation at 0°K of the designated species in gas phase. Assuming that the KE_{MAX} value measured in the threshold photodetachment experiment corresponds to some $CH_3\cdot + CO_2 + e^-$ products in their ground vibrational and electronic states, this dissociation asymptote is 2.56 ± 0.05 eV above $CH_3CO_2^-$ as shown in Figure 3-7. This value is 0.11 eV smaller than the results calculated based on the thermodynamics data from the NIST Standard Reference Database.[40] Combining the present results with the EA of 3.47 eV, the dissociation energy of the $CH_3CO_2\cdot$ radical into $CH_3\cdot + CO_2$ is found to be $D_0(CH_3 - CO_2)$ = -0.91 ± 0.05 eV. These results are summarized in Table 3-1 and Figure 3-7.

Unlike the DPD study on HCO_2^-,[29] no vibrational progressions were observed in the $P(E_T)$ distributions for the DPD of $CH_3CO_2^-$ and $CD_3CO_2^-$ because both CO_2 and $CH_3\cdot$ (or $CD_3\cdot$) can be vibrationally and rotationally excited. The average internal energy ($< E_{int}>$) partitioned into the dissociation products is $<E_{int}>$ = 0.26 eV (2100 cm^{-1}) for $CO_2 + CH_3\cdot$ and $<E_{int}>$ = 0.31 eV (2500 cm^{-1}) for $CO_2 + CD_3\cdot$ at 355 nm, calculated from KE_{MAX}, the average translational energy release $<E_T>$ and the near threshold eKE. When the C-C bond breaks in the $CH_3CO_2\cdot$ radical, the most significant geometric changes are the change of the CH_3 group from a pyramidal to a planar shape, and the relaxation of the bent O-C-O moiety to linear CO_2.[46] The major vibrational excitations expected in the products are thus the out-of-plane umbrella mode of $CH_3\cdot$ and the degenerate bending mode of CO_2. The umbrella (ν_2) frequency is 608.3 cm^{-1} for $CH_3\cdot$ radical[47] and 457.8 cm^{-1} for $CD_3\cdot$,[48] while the bending frequency of CO_2 is ν_2 = 667.3 cm^{-1}.[49] Therefore in the $CH_3\cdot + CO_2$ system, the most probable vibrational excitation is characterized by the sum

of vibrational quantum numbers, $\upsilon_2(CH_3\cdot) + \upsilon_2(CO_2) = 3$ or 4. In the $CD_3\cdot + CO_2$ system, $CD_3\cdot$ is expected to exhibit higher vibrational excitation υ_2 owing to the smaller vibrational quanta.

The observed energy partitioning in the DPD of $CH_3CO_2^-$ can be compared to the pure impulsive model used by Busch and Wilson and later extended by Houston and co-workers.[50,51] Using the pure impulsive model, all the chemical bonds are assumed to be soft except for the one that breaks in the dissociation. In other words, all the atoms not involved in the breaking bond stay still as "spectators". Given a dissociation AB $\rightarrow$ A + B by breaking a chemical bond α-β, with atom α in A and atom β in B, the CM translational energy release E_T is given by:

$$E_T = \frac{\mu_{\alpha\beta}}{\mu_{AB}} E_{avl} \tag{3-3}$$

where E_{avl} is the available energy, μ_{AB} is the reduced mass of A and B, and $\mu_{\alpha\beta}$ is the reduced mass of α and β. The translational and internal energy partitioned into the fragment A can be calculated separately by:

$$E_T(A) = \frac{\mu_{\alpha\beta}}{m_A} E_{avl} \tag{3-4}$$

$$E_{\text{int}}(A) = (\frac{1}{m_\alpha} - \frac{1}{m_A})\mu_{\alpha\beta} E_{avl} \tag{3-5}$$

with analogous equations for fragment B, where m_A, m_B, m_α and m_β are the masses for A, B, α and β respectively. The pure impulsive model can also be used to predict product rotational excitation when the α-β bond is not directed to the CM of A or B, however

Table 3-2: Energy partitioning in the DPD of $CH_3CO_2^-$ and $CD_3CO_2^-$ at E_{hv} = 3.49 eV

		Pure impulsive model		Experimental Values (355 nm)	
		f_T	f_{int}	f_T	f_{int}
$CO_2 + CH_3\cdot$	CO_2	0.14	0.36	-	-
	$CH_3\cdot$	0.40	0.10	-	-
	Sum	0.54	0.46	0.72	0.28
$CO_2 + CD_3\cdot$	CO_2	0.14	0.36	-	-
	$CD_3\cdot$	0.33	0.17	-	-
	Sum	0.47	0.53	0.67	0.33

in the present experiments product rotational and vibrational excitation cannot be resolved, so only the total internal energy will be considered.

Using equations (3-3) – (3-5), the energy partitioning predicted by the impulse model at 355 nm can be calculated. Here the value of KE_{MAX} is used as E_{avl} since eKE is nearly zero at this wavelength. The results of this calculation are listed in Table 3-2, where $f_T = E_T/E_{avl}$, and $f_{int} = E_{int}/E_{avl}$, with comparisons to the experimental values $f_T = \langle E_T \rangle/E_{avl}$ and $f_{int} = \langle E_{int} \rangle/E_{avl}$. The results in Table 3-2 illustrate that in addition to the higher density of internal energy states in the $CD_3\cdot$ product, the isotopic shift in the impulsive partitioning of momentum also causes the shift of the $P(E_T)$ peak to a lower value for $CD_3CO_2^-$ in Figure 5. The pure impulsive model is seen to overestimate the internal energy compared with the experimental results, indicating that the spectator bonds are not entirely "soft". This is not surprising for the relatively high frequency C-H and C-D vibrations. This model also does not account for vibrational excitation in the nascent $CH_3CO_2\cdot$ induced by Franck-Condon photodetachment.

3.3.4 Competition Between Photodetachment and Ionic Photodissociation

Up to this point, only the DPD mechanism has been discussed. However, it is also important to consider another possible reaction path: photodissociation into one neutral and one anion, followed by either autodetachment or photodetachment of the secondary anion by a second photon.

The reaction: $CH_3CO_2^- + h\nu \rightarrow CO_2^- + CH_3\cdot \rightarrow CO_2 + CH_3\cdot + e^-$ is not energetically possible because CO_2^- is ≈ 0.60 eV higher than CO_2 in the energy diagram.[43,52] As shown in Figure 3-7, $E_T = E_{h\nu} - D°(CH_3\text{-}CO_2^-)$. At $E_{h\nu}$ = 3.49 eV, this would require E_T to be smaller than 0.33 eV, which conflicts with the fact that in Figure 3-5(a), $P(E_T)$ begins to rise rapidly above 0.30 eV.

The other reaction path: $CH_3CO_2^- + h\nu \rightarrow CH_3\cdot^- + CO_2 \rightarrow CH_3\cdot + CO_2 + e^-$, needs more careful inspection. The methyl radical, $CH_3\cdot$ has a small EA = 0.08 ± 0.03 eV measured by Ellison, *et al.* [44] Wenthold and Squires studied the collision-induced dissociation (CID) of $CH_3CO_2^-$ and reported the dissociation energy, $D°[CH_3^-\text{-}CO_2]$, of 2.50 ± 0.11 eV.[42] The energetics reported in Figure 3-7 show the result for the upper limit to the bond dissociation energy $D_0[CH_3^-\text{-}CO_2]$ found in the present experiment is 2.48 ± 0.05 eV, consistent with the result of Wenthold and Squires. These energetics show that the photodissociation into $CH_3\cdot^-$ is energetically possible, however, the observed P(eKE) spectra are definitely not consistent with photodetachment of $CH_3\cdot^-$ by a second photon, as very high energy electrons would be produced. In addition, the progressions in the photoelectron spectra [44] recorded by Ellison *et al*. are not observed in our spectra, further evidence against the photodetachment of $CH_3\cdot^-$ by the second photon. If the photodissociation/autodetachment process was occurring, a significant difference

between the photoelectron spectra of the stable radical and dissociation products would also be expected, inconsistent with the experimental results. Finally, an autodetachment lifetime of 9-12 ns for vibrationally excited $CH_3\cdot^-$ was reported by Mitchell *et al* [53]. This relatively long lifetime and the internal energy distribution in the $CH_3\cdot^-$ photofragments would be expected to yield a broad eKE distribution in the present fast-beam experimental setup, not the near-threshold P(eKE) spectra obtained at 355 nm. In summary, ionic photodissociation is ruled out as an effectively competing channel in these experiments.

3.4 Conclusion

The DPD of $CH_3CO_2^-$ and $CD_3CO_2^-$ has been investigated at 355 nm and 257 nm. At 355 nm, a near-threshold photoelectron spectrum shows two nearly degenerate states of $CH_3CO_2\cdot$ (or $CD_3CO_2\cdot$) with an energy spacing of 0.023 eV and an upper limit to the adiabatic EA $\leq 3.47 \pm 0.01$ eV.[54] Tentative evidence for two other states of $CH_3CO_2\cdot$, 3.68 and 3.88 eV higher than the ground state of $CH_3CO_2^-$, was also observed at 257 nm. Following photodetachment, both the dissociation channel $CH_3\cdot/CD_3\cdot + CO_2$ and stable radicals ($CH_3CO_2\cdot/CD_3CO_2\cdot$ or $\cdot CH_2CO_2H/\cdot CD_2CO_2D$) were observed, with a branching ratio $\approx$ 9:1. The similarity of the photoelectron spectra for stable and dissociative products indicates that instead of direct DPD on a repulsive potential energy surface, the nascent $CH_3CO_2\cdot$ radical undergoes a subsequent yet rapid dissociation. It is proposed that the intermediate state interacts with two or more potential energy surfaces leading to rapid dissociation and the formation of long-lived radicals, respectively. The translational energy release observed in these experiments is large, with $\langle E_T \rangle / E_{avl} = 0.72$ for CO_2 +

CH_3· and $<E_T>/E_{avl} = 0.67$ for CO_2 + CD_3· at 355 nm. High-level *ab initio* calculations are needed for a more complete understanding of the energetics and dynamics of the prototypical yet complicated acetyloxyl radical.

References

1 E. A. Lissi, G. Massiff, and A. E. Villa, J. Chem. Soc. Faraday Trans. 1 **69**, 346 (1973).

2 B. Wang, H. Hou, and Y. Gu, J. Phys. Chem. A **103**, 8021 (1999).

3 Z. Zhou, X. Cheng, X. Zhou, and H. Fu, Chem. Phys. Lett. **353**, 281 (2002).

4 J. March, *Advanced Organic Chemistry: Reactions, Mechanisms, and Structure*, 4th ed. (John Wiley & Sons, New York, 1992).

5 L. Herk, M. Feld, and M. Szwarc, J. Am. Chem. Soc. **83**, 2998 (1961).

6 C. Walling, *Free Radicals in Solution*. (John Wiley & Sons, Inc., New York, 1957).

7 M. Levy and M. Szwarc, J. Am. Chem. Soc. **76**, 5981 (1954).

8 H. J. Shine and J. R. Slagle, J. Am. Chem. Soc. **81**, 6309 (1959).

9 L. Herk and M. Szwarc, J. Am. Chem. Soc. **82**, 3558 (1960).

10 H. J. Shine, J. A. Waters, and D. M. Hoffman, J. Am. Chem. Soc. **85**, 3613 (1962).

11 J. C. Martin and E. H. Drew, J. Am. Chem. Soc. **83**, 1232 (1961).

12 J. C. Martin, J. W. Taylor, and E. H. Drew, J. Am. Chem. Soc. **89**, 129 (1967).

13 P. S. Skell and D. D. May, J. Am. Chem. Soc. **105**, 3999 (1983).

14 W. Braun, L. Rajbenbach, and F. R. Eirich, J. Phys. Chem. **66**, 1591 (1962).

15 L. Jaffe, E. J. Prosen, and M. Szwarc, J. Chem. Phys. **27**, 416 (1957).

[16] J. L. Holmes, F. P. Lossing, and P. M. Mayer, J. Am. Chem. Soc. **113**, 9723 (1991).

[17] R. Yamdagni and P. Kebarle, Ber. Bunsenges. Phys. Chem. **78**, 181 (1974).

[18] S. Tsuda and W. H. Hamill, in *Advances in Mass Spectrometry*, edited by W. L. Mead (The Institute of Petroleum, London, 1966), Vol. III, pp. 249.

[19] M. V. Muftakhov, Y. V. Vasil'ev, and V. A. Mazunov, Rapid Commun. Mass Spectrom. **13**, 1104 (1999).

[20] W. E. Wentworth, E. chen, and J. C. Steelhammer, J. Phys. Chem. **72**, 2671 (1968).

[21] C.-F. Ding, X.-B. Wang, and L.-S. Wang, J. Phys. Chem. A **102**, 8633 (1998).

[22] O. Kikuchi, K. Utsumi, and K. Suzuki, Bull. Chem. Soc. Jpn. **50**, 1339 (1977).

[23] S. D. Peyerimhoff, P. S. Skell, D. D. May, and R. J. Buenker, J. Am. Chem. Soc. **104**, 4515 (1982).

[24] E. Sicilia, F. P. D. Maio, and N. Russo, J. Phys. Chem. **97**, 528 (1993).

[25] A. Rauk, D. Yu, and D. A. Armstrong, J. Am. Chem. Soc. **116**, 8222 (1994).

[26] D. Yu, A. Rauk, and D. A. Armstrong, J. Chem. Soc. Perkin Trans. 2, 2207 (1994).

[27] M. Kieninger, O. N. Ventura, and S. Suhai, Int. J. Quant. Chem. **70**, 253 (1998).

[28] E. H. Kim, S. E. Bradforth, D. W. Arnold, R. B. Metz, and D. M. Neumark, J. Chem. Phys. **103**, 7801 (1995).

[29] T. G. Clements and R. E. Continetti, J. Chem. Phys. **115**, 5345 (2001).

[30] R. E. Continetti, Int. Rev. Phys. Chem. **17**, 227 (1998).

[31] H.-J. Deyerl, L. S. Alconcel, and R. E. Continetti, J. Phys. Chem. A **105**, 552 (2001).

[32] L. S. Alconcel, H.-J. Deyerl, M. DeClue, and R. E. Continetti, J. Am. Chem. Soc. **123**, 3125 (2001).

[33] J. A. Davies, J. E. LeClaire, R. E. Continetti, and C. C. Hayden, J. Chem. Phys. **111**, 1 (1999).

[34] M. S. Bowen and R. E. Continetti, J. Phys. Chem. A **108**, 7827 (2004).

[35] C. R. Sherwood and R. E. Continetti, Chem. Phys. Lett. **258**, 171 (1996).

[36] M. N. R. Ashfold, I. R. Lambert, D. H. Mordaunt, G. P. Morley, and C. M. Western, J. Phys. Chem. **96**, 2938 (1992).

[37] D. J. Gendron and J. W. Hepburn, J. Chem. Phys. **109**, 7205 (1998).

[38] R. N. Zare, Mol. Photochem. **4**, 1 (1972).

[39] K. A. Hanold, M. C. Garner, and R. E. Continetti, Phys. Rev. Lett. **77**, 3335 (1996).

[40] *NIST Chemistry WebBook, NIST Standard Reference Database Number 69 (http://webbook.nist.gov/chemistry/)*, edited by W. G. Mallard (National Institute of Standards and Technology, Gaithersberg, MD, 2003).

[41] J. J. Grabowski and X. Cheng, J. Am. Chem. Soc. **111**, 3106 (1989).

[42] P. G. Wenthold and R. R. Squires, J. Am. Chem. Soc. **116**, 11890 (1994).

[43] R. N. Compton, P. W. Reinhardt, and C. D. Cooper, J. Chem. Phys. **63**, 3821 (1975).

[44] G. B. Ellison, P. C. Engelking, and W. C. Lineberger, J. Am. Chem. Soc. **100**, 2556 (1978).

[45] *Tables of molecular vibrational frequencies*, edited by T. Shimanouchi (National Bureau of Standards, Washington, 1972).

[46] M. C. R. Symons, J. Am. Chem. Soc. **87**, 1833 (1983).

[47] J. Wormhoudt and K. E. McCurdy, Chem. Phys. Lett. **156**, 47 (1989).

[48] T. J. Sears, J. M. Frye, V. Spirko, and W. P. Kraemer, J. Chem. Phys. **90**, 2125 (1989).

[49] G. Herzberg, *Molecular Spectra and Molecular Structure Vol. II Infrared and raman Spectra of Polyatomic Molecules*. (Krieger Publishing, Malabar, Florida, 1991).

[50] G. E. Busch and K. R. Wilson, J. Chem. Phys. **56**, 3626 (1972).

[51] K. A. Trentelman, S. H. Kable, D. B. Moss, and P. L. Houston, J. Chem. Phys. **91**, 7498 (1989).

[52] M. Knapp, O. Echt, D. Kreisle, T. D. Mark, and E. Recknagel, Chem. Phys. Lett. **126**, 225 (1986).

[53] S. E. Mitchell, P. M. Conklin, and J. W. Farley, J. Chem. Phys. **118**, 11017 (2003).

[54] Note: Wang and co-workers recently re-measured the EA of CH_3CO_2 by photodetachment of acetate anion cooled to 77 K in a Paul trap, reporting an EA of 3.25 ± 0.01 eV. [X. B. Wang, H. K. Woo, L. S. Wang, B. Minofar, and P. Jungwirth, J. Phys. Chem. A **110**, 5047 (2006)].

Chapter Acknowledgement

This chapter, in full, is a reproduction of the material as it appears in Z. Lu and R.E. Continetti, "Dynamics of the Acetyloxyl Radical Studied by Dissociative Photodetachment of the Acetate Anion," J. Phys. Chem. A **108**, 9962-9969 (2004). The dissertation author was the investigator for this paper.

Chapter 4

Dynamics on the HOCO Potential Energy Surface Studied by Dissociative Photodetachment of $HOCO^-$ and $DOCO^-$

The hydroxyl formyl (HOCO) free radical is an important intermediate in the bimolecular reaction between the hydroxyl radical and carbon monoxide, OH + CO → H + CO_2. Over the last three decades, this reaction has been the focus of intense interest as a result of its importance in determining the CO/CO_2 balance in combustion and atmospheric chemistry,[1] and the role it plays in the release of heat during hydrocarbon combustion.[2] Extensive experimental and theoretical studies have sought to characterize the reaction kinetics and dynamics as well as the structure of the HOCO radical, making this system a benchmark four-atom reaction. In the present work, the dynamics on the HOCO potential energy surface was studied by preparing the HOCO free radical, its deuterated form DOCO and the atomic and molecular dissociation products H/D + CO_2 and OH/OD + CO by the dissociative photodetachment (DPD) of $HOCO^-$ and $DOCO^-$.

Previous theoretical efforts on this system concentrated on construction of an accurate potential energy surface (PES) for the ground electronic state (X^2A') of the HOCO complex that governs the OH + CO → H + CO_2 reaction. McLean and Ellinger reported *ab initio* predictions for the two planar isomers, *trans*- and *cis*- HOCO.[3,4] Several groups have studied the HOCO PES at different levels of *ab initio* and density functional theory (DFT) calculations. Some of these studies have focused particularly on the stationary points along the OH + CO reaction path.[5,6] The first global PES for the H +

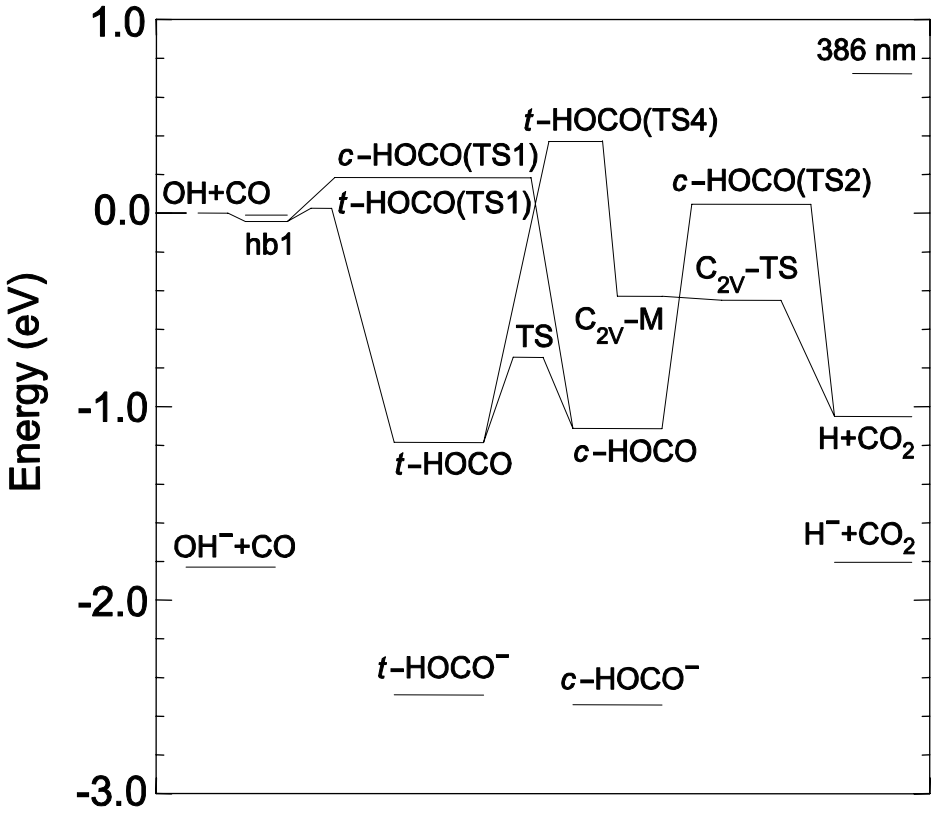

Figure 4-1: Energy diagram for the OH + CO ↔ HOCO* → H + CO_2 reaction and DPD of $HOCO^-$. All energies are in eV and corrected by ZPEs, the ground states of OH + CO are selected as reference. Energetics of OH^- + CO, as well as anionic and neutral HOCO minima are from Ref. 7; The EA of the H atom, 0.754 eV,[8] was used to determine the stability of H^- + CO_2; the energies of other species here are from Ref. 9. The photon energy here is in reference to *trans*-$HOCO^-$.

CO_2 reaction was presented by Schatz *et al.* in 1987, using singly and doubly excited configuration interaction (SDCI) calculations and a many-body expansion fit.[10] This surface has been improved several times over the following years.[9,11-13] A number of other attempts to develop partial or full-dimensional HOCO PESs have been made using a variety of different methods.[14-16] Most recently, a new high-level *ab initio* CASSCF/MRCI calculation with all 17 valence electrons and 13 valence orbitals included in the active space was performed by Wang and coworkers, reporting a calculated heat of reaction of –24.1 kcal/mol at 0K for OH + CO → H + CO_2.[17] They also used these high-level reference calculations to assess new DFT approaches to calculate this PES.

The energetics of the HOCO system obtained from several recent high-level quantum calculations are summarized in Figure 4-1 and Table 4-1, with the zero point energy (ZPE) corrected OH + CO products chosen as the reference. Although these theoretical predictions depend greatly on different calculation levels, it is well accepted that the *trans*-HOCO conformer is slightly lower in energy than *cis*-HOCO, with an isomerization barrier (TS in Figure 4-1) estimated to be ~ 0.35 eV higher than *trans*-HOCO.[9,13,16,17] In the reaction of OH + CO, *trans*-HOCO is initially formed via a transition state (*t*-HOCO TS1) that is nearly isoenergetic with the OH + CO asymptote (see Table 1),[9,16,17] then converts into the *cis*-HOCO conformer. The saddle point (*c*-HOCO TS2) separating the *cis*-HOCO complex and the reaction exit channel H + CO_2 is characterized by a high imaginary frequency (2053i cm^{-1})[9] that is consistent with several predictions claiming that H + CO_2 products are formed by tunneling through the TS2 barrier.[6,14,18] In addition, two hydrogen bonded complexes OH···CO (hb1) and OH···OC

Table 4-1: Theoretical prediction of relative energies for HOCO system (eV)[a)]

	CCF[b]	DFF[c]	FDF[d]	LTSH[e]	YMS[f]	VHK[g]	SLHW[h]
OH + CO	0.00	0.00	0.00	0.00	0.00 (-0.06)	0.00	0.00
t-HOCO (TS1)					0.03 (-0.05)	0.04	-0.03
c-HOCO(TS1)					0.18 (0.11)	0.17	0.14
OHCO (hb1)					-0.04 (-0.12)	-0.01	-0.04
OHOC (hb2)					-0.01 (-0.08)	0.01	-0.01
t-HOCO (min)	-1.19	-1.10	-1.12	-1.31	-1.10 (-1.19)	-1.06	-1.00
c-*t*-HOCO (TS)			-0.87	-0.96	-0.75 (-0.83)	-0.73	-0.64
c-HOCO (min)	-1.11		-0.99	-1.21	-1.03 (-1.12)	-0.92	-0.92
c-H···OCO (TS2)				0.07	0.05 (0.03)	0.05	0.11
t-HOCO (TS4)				0.34	0.37 (0.33)	0.40	0.49
C_{2v}-HCO_2 (min)			-0.49	-0.63	-0.43 (-0.51)	-0.46	-0.47
C_{2v}-HCO_2 (TS)				-0.42	-0.45 (-0.47)	-0.44	-0.47
H···OCO (vdw)					-1.07 (-1.07)	-1.07	
H + CO_2					-1.07 (-1.07)	-1.07	-1.05
t-$HOCO^-$	-2.49	-2.46					
c-$HOCO^-$	-2.54	-2.52					
AEA *t*-HOCO	1.30	1.36					
AEA *c*-HOCO	1.43						

[a)] All energies have been corrected by ZPEs, OH + CO is used as reference, *t*- stands for *trans*- and *c*- stands for *cis*-; [b)] CCF: Clements, Continetti, and Francisco, Ref. 7, the reference for the OH + CO asymptote was determined by the calculated energetics of OH^- + CO in Ref. 7 and the EA(OH) = 1.8277 eV;[19] [c)] DFF: Dixon, Feller, and Francisco, Ref. 20; [d)] FDF: Feller, Dixon, and Francisco.[21] Note that $\Delta_f H^0$(OH) = 8.85 ± 0.07 kcal/mol [22] and a calculated $\Delta_f H^0$(CO) = -27.0 kcal/mol [21] was used to obtain the reference OH + CO asymptote in both DFF and FDF; [e)] LTSH: Lakin, Troya, Schatz, and Harding, Ref. 13; [f)] YMS: Yu, Muckerman, and Sears, Ref. 9, in parentheses, energetics of species involved in the OD + CO → D + CO_2 reaction; [g)] VHK: Valero, van Hemert, and Kroes, Ref. 16; [h)] SLHW: Song, Li, Hou, and Wang, Ref. 17.

(hb2) exist along the entrance channel OH + CO before the formation of *t*-HOCO TS1, which may play important roles in the abnormal temperature and pressure dependences of the reaction rate coefficients.[23,24] A less favorable reaction path involves *trans*-HOCO converting to the C_{2v} symmetry H·CO_2 conformer over a high barrier (TS4) with subsequent dissociation into H + CO_2.[9,11,12,17]

To evaluate these surfaces, one has to compare the theoretical predictions with experimental results. The HOCO radical and its deuterated form DOCO have been observed in cryogenic matrices[25-27] and the gas-phase[28-35], and their rotational[29-34] and vibrational frequencies[25-27] have been reported and can be directly compared with calculated values. Lester and coworkers reported spectroscopic evidence for the OH···CO complex in the OH + CO entrance channel.[24,36,37] Additionally, significant experimental and theoretical efforts have been carried out to study the pressure and temperature dependences of the rate coefficient of the OH + CO reaction, providing evidence for a deep HOCO well and a high barrier leading to the formation of H + CO_2.[6,18,38-45] The OH + CO [46-49] and H + CO_2 [50-54] collisions have been studied by various experimental techniques as well, yielding cross sections and internal energy distributions in reaction products. These experimental results can be compared with theoretical predictions based on *ab initio* PESs and classical/quasi-classical trajectory theories[11-13,23,55,56] or quantum dynamics calculations [55-62].

However, there remains a lack of detailed and direct measurement of the global HOCO PES. For instance, it is difficult to measure the depth of the HOCO potential well accurately. Early attempts were made to obtain a heat of formation of the HOCO radical by measuring the appearance potential of $C_2H_5^+$ from electron impact of $C_2H_5CO_2H$ or

CH_3^+ from CH_3CO_2H,[63,64] reporting $\Delta_f H^0$ to be -39 kcal/mol and -58 ± 4 kcal/mol respectively. Ruscic *et al.* obtained $\Delta_f H^0 = -52.5 \pm 0.6$ kcal/mol directly by photoionization of the HOCO radical.[28] Later this value was revised to be $\Delta_f H^0 \geq -45.8$ ± 0.7 kcal/mol using the same technique,[65] yielding a HOCO well depth less than 1.20 eV relative to the OH + CO asymptote. In addition, the role of a tunneling mechanism for production of H + CO_2 has been debated in different studies,[6,18,38-42,47] and a direct measurement of the height of the various transition states on this PES has yet to be completed.

Recently the dynamics and PES of the HOCO free radical were studied by Clements *et al.* using dissociative photodetachment (DPD) of the anion precursor $HOCO^-$.[7] Using photoelectron-photofragment coincidence (PPC) spectroscopy, three product channels after the photodetachment of $HOCO^-$ with 4.80 eV (258 nm) photons were reported:

$$HOCO^- + h\nu \rightarrow HOCO + e^- \quad (4\text{-}1)$$

$$HOCO^- + h\nu \rightarrow OH + CO + e^- \quad (4\text{-}2)$$

$$HOCO^- + h\nu \rightarrow H + CO_2 + e^- \quad (4\text{-}3)$$

While the majority of photodetachment products are stable HOCO radicals, unimolecular dissociation into H + CO_2 and OH + CO fragments, as well as the evidence for direct DPD on a repulsive excited electronic state yielding ground state OH + CO + e^-, were observed.

The DPD studies are based on the discovery and characterization of a stable, bound $HOCO^-$ anion precursor. The first experimental evidence for this species was

reported in flowing afterglow experiments studying the hydroxide-transfer reaction of H_3O^- + CO and indicated the presence of a negative ion with m/e = 45 that was determined not to be the more stable formate anion, HCO_2^-.[66] Interpretation of the DPD experiments was aided by high-level *ab initio* calculations on $HOCO^-$ and HOCO by Clements *et al.*[7] The adiabatic electron affinities (AEAs) of the two HOCO isomers were predicted to be 1.43 eV (*cis*-) and 1.30 eV (*trans*-) respectively from CCSD(T) calculations [Clements, Continetti and Francisco (CCF), see Table 4-1], which agrees well with the DPD measurements.[7] The same calculation predicted a deeper neutral HOCO well compared with most of the other calculations listed in Table 4-1, except for the LTSH (Lakin, Troya, Schatz, and Harding) results. Dixon *et al.* recently predicted an AEA for *trans*-HOCO to be 1.36 eV as well as the energy of the *cis* anion [see DFF (Dixon, Feller, and Francisco) results in Table 4-1].[20] These authors reported energetics of both *cis*- and *trans*-HOCO radicals using a slightly different theoretical approach elsewhere [see FDF (Feller, Dixon, and Francisco) results in Table 4-1],[21] with a 0.02 eV difference seen between the depth of the *trans*-HOCO well reported in the DFF [20] and FDF results[21]. Therefore, an accurate prediction for the AEA of the *cis* conformer is not available in the recent work of Dixon and coworkers. In addition, the anion stability relative to the OH + CO asymptote predicted by CCF and DFF only differs by 0.03 eV and 0.02 eV for the *trans*- and *cis*-$HOCO^-$ isomers, respectively (see Table 4-1). Thus, we will continue to use the consistent level of theory for both anions and neutrals reported by CCF.

The previous DPD study provided important experimental information on the HOCO PES. However, there are several questions remaining unanswered, in particular,

the role played by tunneling in the dissociation to H + CO_2, the observation of a significant fraction of the OH + CO + e^- products at total kinetic energies beyond the calculated energetic maximum, and a detailed comparison of the product branching ratios with statistical and quantum dynamical predictions. To achieve a better understanding of the reaction mechanisms and energetics of this system, in the current work we compare the DPD dynamics of the deuterated anion $DOCO^-$ with $HOCO^-$ at a photodetachment wavelength of 386 nm ($E_{h\nu}$ = 3.21 eV). The use of a longer wavelength in this study removes potential contributions from excited electronic states of HOCO and provides improved photoelectron kinetic energy resolution. Following a brief review of the experimental technique, the photoelectron spectra corresponding to channel (1) and the PPC spectra arising from the DPD channels (2) and (3) for both isotopologs will be presented, as well as the branching ratios for the three neutral product channels. The observed isotope effects and inferred DPD mechanisms will be discussed in detail and compared with recent theoretical predictions by Zhang *et al*.[67]

4.1 Experiment

The fast-ion-beam PPC spectrometer employed in the present study is capable of measuring angle-resolved photoelectron and photofragment kinetic energies from a single DPD event in coincidence, allowing a direct probe of the dissociation dynamics on the neutral PES after photodetachment.[68] The experimental approach is similar to the previous DPD study by Clements *et al.*[7] with the exception that a new multiparticle photofragment imaging detector was used in this study and the photoelectron spectra were solely recorded by an imaging detector. Therefore only a brief review of

experimental method will be presented here. In the final measurements reported here, the $HOCO^-$ anion (m/e = 45) was created using electron impact on a 1 kHz pulsed supersonic expansion of 7% CO, 6% N_2O, 17% CH_4, and 70% N_2. For the $DOCO^-$ experiments, CD_4 (99%, Cambridge Isotope Laboratory) instead of CH_4 was used in the precursor gas mixture. Here N_2 was used to dilute the gas mixture and assist the collisional cooling in supersonic expansion. An alternative experiment without N_2 showed no observable difference, ruling out the involvement of $OH^-(N_2)$ species (m/e = 45) in the present study. A plausible mechanism for the generation of the $HOCO^-$ anion involves electron impact on the N_2O/CH_4 mixture forming OH^- followed by the association of OH^- with CO to form $HOCO^-$ in the free-jet expansion. The nozzle-skimmer distance used in these experiments was 1.5 – 2.0 cm, and an interesting observation was made that $HOCO^-$ was formed most effectively when the electron beam was closer to the skimmer aperture. Thus, the condensation of neutrals into clusters followed by electron impact on those clusters may play an important role in the production of $HOCO^-$. After passing into a differentially pumped chamber, the anions were accelerated to 10 keV and mass selected by time-of-flight before being intercepted by a linearly polarized laser. The second harmonic (386 nm, E_{hv} = 3.21 eV) of a pulsed Ti:Sapphire laser (Clark-MXR CPA-2000, 1.8 ps FWHM, ~1 x 10^{10} W/cm^2) was used for photodetachment.

The full 4π sr solid angle of photoelectrons was collected by a space focusing electron optics assembly.[69,70] The time- and position-sensitive photoelectron detector allows the measurement of three-dimensional (3D) photoelectron velocities and is positioned parallel to the plane of the ion and laser beams. The photoelectron kinetic energy (eKE) resolution can be improved by discarding events with significant

photoelectron velocity components perpendicular to the plane of the electron detector. The resulting photoelectron intensity distribution in these equatorially sliced photoelectron spectra is corrected based on the cylindrical symmetry about the electric vector of the laser when the laser polarization is along the ion beam and parallel to the face of the electron detector.[71] The photoelectron kinetic energy (eKE) resolution is $\Delta E/E \sim 13\%$ determined by photodetachment of OH^- at 386 nm (eKE = 1.38 eV).

Undetached anions were deflected out of the fast beam, while the neutral products impinged on a time- and position-sensitive detector which consists of a stack of microchannel plates and a fast-delay-line anode.[72] Stable neutral products (HOCO radicals) arrive at the detector at a time and position determined by the velocity vector distribution that characterizes the parent $HOCO^-$ ion packet prior to photodetachment. In the case of DPD, the time-of-arrival of two coincident photofragments has to differ by more than a ~ 17 ns dead time of the detector. The mass ratio of the coincident photofragments ($H + CO_2$ or $OH + CO$) and the center of mass (CM) kinetic energy release were determined by conservation of linear momentum using the time- and position-of-arrival information.[73,74] One has to be cautious about the large false coincidence rate in the DPD process of $HOCO^-$ as the majority neutral products are stable HOCO free radicals and the kinetic energy release among dissociation fragments is small. An additional gating on the photofragment mass spectra was applied in the data analysis procedure, reducing the false coincidence contribution to the data significantly. As a result of the large difference in masses for the $H + CO_2$ product channel, a large fraction of the H atom products miss the detector even at a beam energy of 10 keV, so the detector acceptance function (DAF), as well as the low detection efficiency for H atoms

with microchannel-plate detectors,[75] plays an important role in the detection of this product channel. A Monte Carlo simulation has been used to calculate the DAF of the present spectrometer under these experimental conditions and correct the intensity distributions in the two dissociation product channels.[76] The DPD of O_4^- at 532 nm was used to calibrate the neutral particle detector, yielding a resolution of $\Delta E_T/E_T \sim 9\%$.

4.2 Results

In accord with the previous DPD study using 4.80 eV photons, three neutral product channels were observed after the photodetachment of $HOCO^-$ or $DOCO^-$ at 3.21 eV. In this section, the experimental results for $H/D + CO_2 + e^-$, $OH/OD + CO + e^-$ and $HOCO/DOCO + e^-$ channels will be presented separately, including the PPC spectra for both DPD channels and photoelectron spectra for the stable HOCO/DOCO channel.

4.2.1 $H/D + CO_2 + e^-$ Channel

The PPC spectra, $P(eKE, E_T)$, for the $H + CO_2 + e^-$ and $D + CO_2 + e^-$ channels resulting from the DPD of $HOCO^-$ and $DOCO^-$ respectively, are shown in Figure 4-2. The PPC spectrum is a two-dimensional (2D) histogram where the intensity of each point represents the probability for observation of an event with a specific partitioning of kinetic energy between the photoelectron (eKE) and the recoil of the neutral photofragments (E_T) in the center-of-mass (CM) frame. The photoelectron spectrum P(eKE) displayed on the left side and the photofragment translational energy spectrum $P(E_T)$ on the bottom of the coincidence spectrum are generated by integrating over the complementary variable in the 2D spectrum. As mentioned in the experimental section,

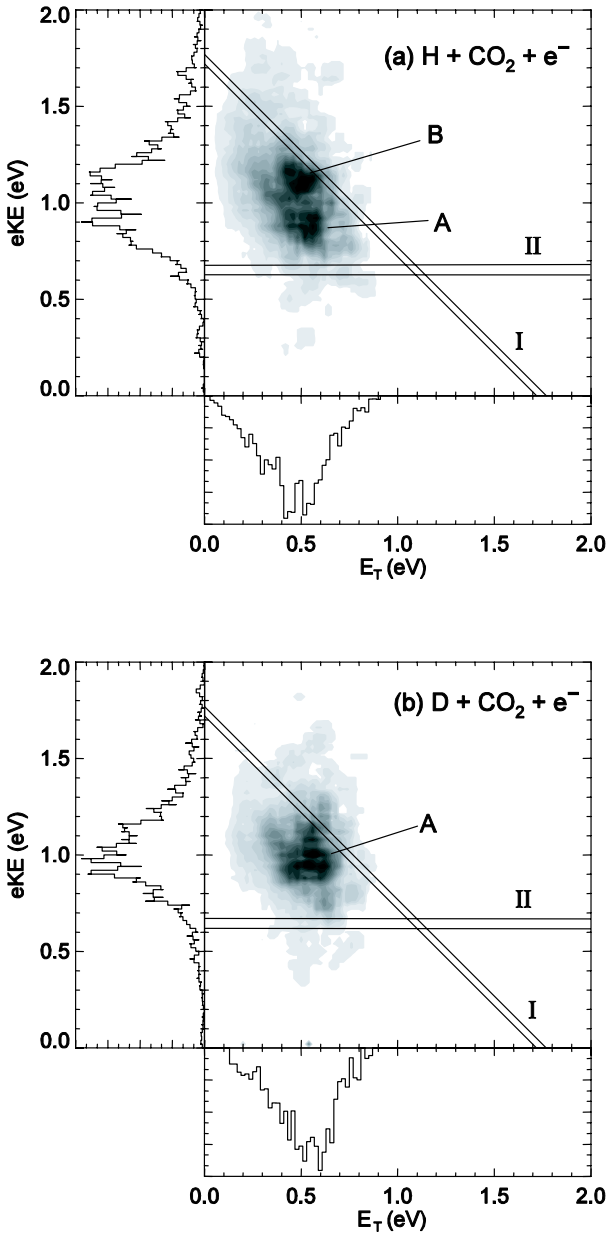

Figure 4-2: Photoelectron-photofragment kinetic energy correlation spectra, P(eKE, E_T) for (a) $HOCO^- + h\nu \rightarrow H + CO_2 + e^-$ and (b) $DOCO^- + h\nu \rightarrow D + CO_2 + e^-$ at $E_{h\nu}$ = 3.21 eV. In both (a) and (b) The diagonal lines I correspond to the theoretically predicted maximum kinetic energy release (KE_{max}) [7] for production of ground state $H + CO_2 + e^-$ from ground state *trans*- and *cis*-$HOCO^-$. Horizontal lines II represent the predicted eKE for nascent HOCO radicals with the same energy as the *c*-HOCO TS2 barrier in Figure 4-1, assuming the parent anions are vibrationally "cold", as discussed in the text.

only a small fraction of H products can be detected, making it necessary to DAF-correct the raw coincidence spectra, N(eKE, E_T), to generate the final P(eKE, E_T) in Figure 4-2. The coincidence spectra presented here are truncated at E_T = 0.025 eV. This is necessary because the DAF around E_T = 0 rapidly approaches zero due to the dead time of the neutral particle detector and false coincidences from stable HOCO radicals increase when E_T is close to zero. As a result, the DAF corrected spectra are accompanied by an artificially high intensity at very small E_T. The equatorial slicing of photoelectron velocities is not used in the PPC spectra. Therefore the P(eKE, E_T) distributions presented here provide a complete kinematic description of the DPD process.

The two closely spaced diagonal lines I in Figure 4-2 are theoretical predictions for KE_{max}, the maximum kinetic energy release for all products (eKE + E_T) in the DPD process $HOCO^- + h\nu \rightarrow H + CO_2 + e^-$ at $E_{h\nu}$ = 3.21 eV. The two predicted KE_{max} values, 1.72 eV for *cis*-$HOCO^-$ and 1.77 eV for *trans*-$HOCO^-$, are determined in the manner described by Clements *et al.*[7]. In the present experiments, there is no clear way to determine the relative population of these predicted isomers in the parent ion beam. Since no theoretical calculations on $DOCO^-$ are available, the KE_{max} values calculated for DPD of $HOCO^-$ are also used in Figure 4-2(b), showing the energetic limits qualitatively. More events extend beyond KE_{max} in $D + CO_2 + e^-$ than in $H + CO_2 + e^-$, because the deuterated experiment was carried out at a higher signal counting rate to minimize the consumption of the isotopic gas mixture, leading to a larger contribution of false coincidences.

Isotope effects in the DPD channel of $HOCO^- + h\nu \rightarrow H + CO_2 + e^-$ can be examined by comparing Figure 4-2(a) and 2(b). The photoelectron kinetic energy

spectrum correlated with the H + CO_2 neutral product channel has a relatively broad distribution and a peak at ~ 1.1 eV, while the P(eKE) distribution in the D + CO_2 + e^- channel is obviously narrower, with a peak ~ 1.0 eV. In the P(E_T) spectrum for H + CO_2 neutral fragments, in addition to the two features at 0.43 and 0.52 eV, some evidence for a progression in the product CO_2 bending mode (~0.08 eV) [77] is observed. This progression is similar to the previous observation in a study of the DPD of HCO_2^-, the formate anion isomer of $HOCO^-$.[78] It should be noted, however, that the formate anion has an EA ~ 3.49 eV,[79] and as a result has a very different photoelectron spectrum that cannot contribute to the present observations given a photon energy of 3.21 eV. Figure 4-2(b) shows that a similar P(E_T) spectrum was observed for the D + CO_2 neutral products from DPD of $DOCO^-$, with the two major peaks shifted to 0.49 and 0.56 eV, respectively.

The horizontal line set II at eKE = 0.67 eV (*trans*-$HOCO^-$) and 0.62 eV (*cis*-$HOCO^-$) in Figure 4-2 shows the dissociation barrier *c*-HOCO TS2 into H + CO_2 products as predicted by *ab initio* calculations of TS2 (Ref. 9) and the ground state anions.[7] It is evident that nearly all of the eKE distribution is at higher energies than this limit, implying that dissociation into H + CO_2 occurs *below* the calculated TS2 barrier using the assumption that the parent $HOCO^-$ anions have no internal excitation prior to photodetachment. This and other aspects of these spectra will be addressed further in section 4.3.

4.2.2 OH/OD + CO + e^- Channel

DPD of $HOCO^-$ into OH + CO + e^- was also observed. Figure 4-3 shows the PPC spectra, P(eKE, E_T), for DPD of (a) $HOCO^-$ + hν → OH + CO + e^-, and (b) $DOCO^-$ + hν

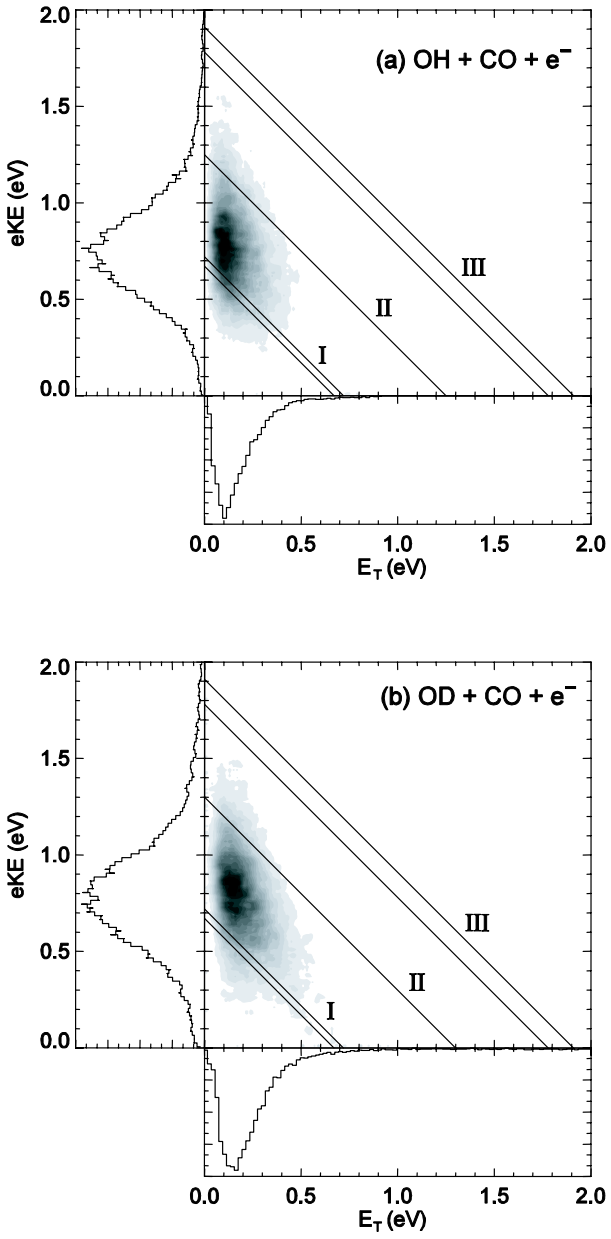

Figure 4-3: Photoelectron-photofragment kinetic energy correlation spectra, P(eKE, E_T) for (a) $HOCO^- + h\nu \rightarrow OH + CO + e^-$ and (b) $DOCO^- + h\nu \rightarrow OD + CO + e^-$ at $E_{h\nu} = 3.21$ eV. In both (a) and (b), the diagonal lines I correspond to the theoretical predictions of KE_{max} for the production of ground state OH + CO + e^- from the vibrationally "cold" *trans*- and *cis*-$HOCO^-$ anions, respectively.[7] The diagonal line II corresponds to the experimental value of KE_{max}. The diagonal lines III represent the predicted maximum available energy for photodetachment of ground state *trans*- and *cis*-*H*OCO^- to the bottom of the corresponding HOCO well.[7]

→ OD + CO + e^-. The calculated energetic limitations, KE_{max} (0.72 eV for *trans*-$HOCO^-$ and 0.67 eV for *cis*-$HOCO^-$), [7] are marked by diagonal lines I. As Figure 4-3 shows, most of the OH + CO + e^- events have a total kinetic energy (KE_{total} = eKE + E_T) larger than the theoretical value of KE_{max}. The line set II in Figure 4-3 shows the experimental KE_{max} values, ~ 1.25 eV for OH + CO + e^- and ~ 1.30 eV for OD + CO + e^- respectively, which are determined from the contour at 15% of peak and represented the estimated level of false coincidences. Such significant disagreement between the absolute theoretical energy limits and the experimental results was not observed in the H + CO_2 + e^- DPD channel, although this discrepancy is similar to the observation that the H + CO_2 + e^- channel appears to occur below the *c*-HOCO TS2 barrier on the PES. To compare the current work with the previous DPD study of $HOCO^-$ at E_{hv} = 4.80 eV, the maximum available energies (1.78 eV for *cis*- and 1.91 eV for *trans*-$HOCO^-$) predicted for photodetachment from the ground state of $HOCO^-$ to the bottom of the neutral HOCO well (CCF calculation) (Ref. 7) are also shown on Figure 4-3 by lines III.

The isotope effects on the OH + CO + e^- channel are not as obvious as those observed in H + CO_2 + e^-. A Gaussian fit to the overall profile in the P(eKE) spectra correlated with the OH + CO and OD + CO neutral products yields peaks of 0.73 and 0.76 eV, respectively. However, the most intense part of the PPC spectrum for OD + CO + e^- [Figure 4-3(b)] definitely is displaced farther from line set I toward higher eKE compared with the PPC spectrum for OH + CO + e^- [Figure 4-3(a)]. In the P(eKE) spectra for OH + CO + e^-, three barely resolved peaks are seen to be spaced by 0.08 ~ 0.09 eV from each other, in agreement with the predicted C-O′ stretching frequency in $HOCO^-$ (663 cm^{-1} for *trans*- and 741 cm^{-1} for *cis*-$HOCO^-$) (Ref. 7) where O′ represents

the O atom connecting the C and H atoms. Evidence for at least two of these three peaks is also observed with a shift to higher eKE in the P(eKE) distribution for OD + CO + e^-. The shapes of $P(E_T)$ for the OH + CO and OD + CO channels are very similar, with peaks at 0.12 and 0.15 eV, respectively.

4.2.3 Stable HOCO + e^- Channel

As discussed in the introduction, the photodetachment of $HOCO^-$ not only leads to the two DPD channels OH + CO + e^- and H + CO_2 + e^-, but predominantly yields the stable HOCO free radical. Figure 4-4(a) shows the overall photoelectron spectrum, P(eKE), recorded in coincidence with either one or two neutral particles from the photodetachment of $HOCO^-$. This spectrum contains contributions from both stable and dissociative photodetachment, including dissociative events where only one of the atomic or molecular products is detected. The P(eKE) peaks in Figure 4-4(a), at 1.18 eV for $HOCO^-$ and 1.22 eV for $DOCO^-$ respectively, are at significantly higher eKEs compared to either of the DPD channels, H/D + CO_2 + e^- and OH/OD + CO + e^-. As discussed by Clements *et al.*, this is consistent with the production of stable HOCO/DOCO radicals.[7]

An analysis of the P(eKE) distributions coincident with only stable HOCO radicals was carried out by including only photoelectrons detected in coincidence with a single neutral particle. In addition, for any neutral particle taken into account as a stable HOCO radical, the reconstructed 3D position-of-arrival at the detector was required to fall within a small ($r \leq 1$ mm) spherical region centered on the parent ion beam. This effectively reduces false coincidence contributions to the stable HOCO spectrum from DPD events where only one particle, which in general recoils out of this spherical region,

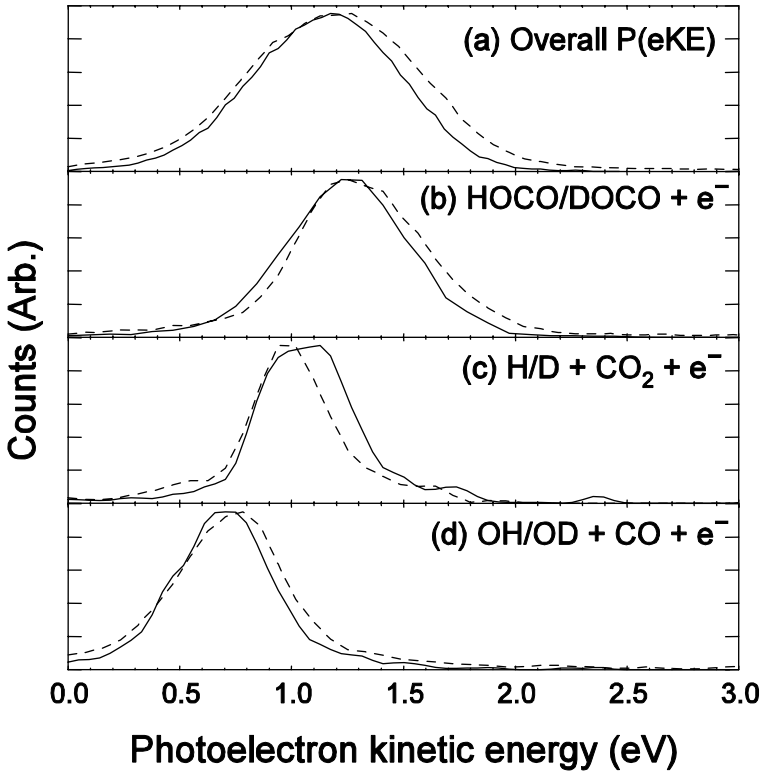

Figure 4-4: Photoelectron kinetic energy spectra P(eKE) from photodetachment of $HOCO^-$ (solid lines) and $DOCO^-$ (dashed lines): (a) overall P(eKE) observed in experiment; (b) P(eKE) spectra in coincidence with stable HOCO/DOCO; (c) P(eKE) in coincidence with H/D + CO_2; (d) P(eKE) in coincidence with OH/OD + CO.

is detected. False coincidence contributions for the H/D + CO_2 channel will remain the largest, however, given the low detection efficiency for the H/D atoms and the fact that the recoil of CO_2 out of the ion beam is small. The resulting P(eKE) spectra shown in Figure 4(b), are shifted to higher eKE, with the peaks at 1.29 eV for stable HOCO + e^- and 1.32 eV for stable DOCO + e^-. The eKE spectra from H/D + CO_2 + e^- and OH/OD + CO + e^- are also summarized in Figures 4(c) and (d), showing that distinct yet overlapping eKE spectra are observed for the three competing neutral product channels.

4.3 Discussion

The DPD of $HOCO^-$ and its deuterated form allows a direct examination of theoretical predictions of the energetics and dynamics of the HOCO free radical and the potential energy surface governing the OH + CO → H + CO_2 reaction. In this section, first the theoretical studies of this system will be used to examine the mechanisms responsible for the observations presented here. Special attention will be paid to the potential role of vibrationally excited anions in both of the DPD channels and the tunneling mechanism in the H/D + CO_2 channel. The isotope effects observed in the P(eKE, E_T) coincidence spectra for $HOCO^-/DOCO^-$ will be discussed as well. Finally, the branching ratios for the three neutral product channels after the photodetachment of $HOCO^-/DOCO^-$ will be compared with the theoretical predictions from the most recent six-dimensional quantum wavepacket dynamics calculations.[67]

Only the ground electronic state of the HOCO radical can be accessed by photodetachment of the $HOCO^-$ anion at $E_{h\nu}$ = 3.21 eV.[7] Although all of the energy minima and saddle points shown on Fig. 1 are energetically allowed, the region of the PES where nascent HOCO radicals can be produced is restricted by the Franck-Condon overlap determined by the structure of the parent anion. The HOCO radicals with the highest energy on the PES can be expected to lead to OH + CO + e^- products, in competition with the more thermodynamically favorable dissociation channel leading to H + CO_2 + e^-. Those nascent HOCO intermediates possessing the lowest energy (highest eKE) are trapped inside the deep potential well and form stable free radicals.

As mentioned in the section 4.2.1, with the assumption that all the anions before photodetachment are in the vibrational ground state, nearly all of the H + CO_2 + e^-

products will be formed below the *c*-HOCO TS2 barrier, but have enough energy to surmount the H·CO_2 barrier connecting the C_{2v} H·CO_2 local minimum to H + CO_2 products. As noted before, the P(E_T) distributions for H + CO_2 are found to be similar to those obtained from the DPD study of HCO_2^-,[78] making it necessary to examine the possibility that HOCO intermediates dissociate into H + CO_2 over the H·CO_2 barrier, instead of passing through the most favorable reaction path involving *c*-HOCO TS2 expected for a parent $HOCO^-$ anion.

DPD of the HCO_2^- anion can be ruled out because the 3.21 eV photon energy used in these experiments is less than the 3.49 eV required to photodetach HCO_2^-.[79] Forming the C_{2v} H·CO_2 conformer via *trans*-HOCO (the expected route) is not likely either, as this isomerization involves a high calculated barrier TS4, inconsistent with the observed photoelectron spectra which show that all the HOCO intermediates are produced with internal energies below TS4. Therefore the involvement of the H·CO_2 barrier in H + CO_2 dissociation can be ruled out assuming the parent anions are vibrationally "cold".

If the anions were vibrationally excited, it would require 1.2 eV vibrational excitation in *trans*-$HOCO^-$ to overcome the TS4 barrier and yield the P(eKE) spectrum seen in this experiment, or 1.5 eV excitation in HCO_2^- to produce a P(eKE) peak at 1.1 eV. The first case is impossible since *trans*-$HOCO^-$ would dissociate into OH^- + CO or H^- + CO_2 with such high excitation (see Figure 4-1).[7] For the second case regarding HCO_2^-, even if the anions can be thermally excited by 1.5 eV, the low-lying excited electronic states of HCO_2 radical would be involved on the neutral PES generated by the photodetachment, and as a result a significantly different P(eKE) spectrum from Fig. 4(c)

would be expected.[78,79] Thus, the H·CO_2 barrier is not likely to play a role in the production of H + CO_2 in this experiment.

A second explanation is that H + CO_2 products are formed by tunneling through the *c*-HOCO TS2 barrier. Several previous studies have suggested that the production of H + CO_2 by tunneling may play an important role in the OH + CO reaction.[6,14,18,43] However, the tunneling effect cannot explain why the other DPD channel OH + CO + e^- is observed beyond the maximum energetic limits dictated by the available thermochemical data and theoretical predictions. Assuming that the theoretical calculations are correct, this disagreement can only be explained by the existence of either vibrationally excited $HOCO^-$ or other, unknown, anion isomers or excited electronic states with energies higher than the theoretically predicted *cis*- and *trans*-$HOCO^-$ isomers. Examination of the experimental KE_{max} in the OH + CO + e^- channel [line II in Figure 4-3(a)] shows that if this unknown anion isomer exists, its stability relative to OH + CO + e^- will be roughly -2.0 eV, only ~ 0.2 eV below the OH^- + CO reactants. Therefore the potential involvement of weakly bonded (OH^-)CO species in the $HOCO^-$ beam must also be considered. However, as noted in the earlier study by Clements *et al.*, the photoelectron angular distribution (PAD) for $HOCO^-$ peaks parallel to the laser electric vector. This is inconsistent with a weakly perturbed OH^- species as the PAD of OH^- is perpendicular to the laser polarization.[80] There is no theoretical evidence for the other anion isomer conformers such as $HOOC^-$ or $OHCO^-$ to date, although they cannot be completely ruled out.

Clements *et al.* proposed that either false coincidences with stable HOCO radicals or vibrationally excited $HOCO^-$ must be responsible for the significant discrepancy

between the experimental and theoretical KE_{max} in the OH + CO + e^- channel. The longer wavelength used for photodetachment in the present work allows a more accurate measurement of the photoelectron spectra, and more effective discrimination against false coincidences with additional mass-gating. The most likely mechanism for the observed spectra, therefore, is the presence of vibrationally excited $HOCO^-$ in the ion beam. The evidence of hot bands in parent ions has been observed in a previous experiment studying the photodetachment of $CH_3CO_2^-$ at 355 nm. An unresolved long tail in the near-threshold region of eKE spectrum[81] was later proved to be the mixing of vibrational progressions of OCO bending in CH_3CO_2 radical and hot bands of $CH_3CO_2^-$ by a photodetachment study of low-temperature $CH_3CO_2^-$.[82] The influence of hot bands may be more severe in the present study. As noted in the experimental section, when generating $HOCO^-$, a relatively long nozzle-skimmer distance was used, with electron impact localized near the skimmer aperture. Thus, collisional cooling of nascent $HOCO^-$ may not be effective in the limited expansion remaining. In another experiment studying the near-threshold photodetachment of $HOCO^-$ using 1.60 eV photons, evidence was seen in the photoelectron spectra for hot bands of ~ 0.3 eV relative to the theoretical predictions of the EA for $HOCO^-$.[83] This further supports the production of a vibrationally excited, and very possibly non-thermal, distribution of $HOCO^-$ and $DOCO^-$ anions in the source. This could explain the observation of the OH + CO + e^- channel above the theoretically predicted energetic limits for KE_{max} by DPD of these vibrationally "hot" $HOCO^-$. The experimental KE_{max} in OH + CO + e^- is approximately 0.5 eV higher than the theoretical value, indicating excitation of some of the parent anions by several quanta of C-O′ stretching, which may preferentially lead to the C-O′ bond breaking upon

photodetachment and enhance the production of OH + CO. The tentative observation of a progression in the C-O′ stretch of $HOCO^-$ in the P(eKE) spectra for the OH + CO + e^- channel mentioned in the section 4.2.2 further supports this mechanism.

The existence of vibrationally excited parent anions in the production of OH + CO + e^- is also crucial in explaining the isotope effect observed in Figure 4-3(b). In $DOCO^-$, the density of vibrational states is larger than in $HOCO^-$, so more vibrational excitation might be expected. Therefore, the shift in the P(eKE) of Figure 4-3(b) to higher eKE is likely to arise from the increased population of vibrationally excited states in $DOCO^-$ and small isotopic shifts in the EA. The significant decrease of the O′-H stretching frequency [9] in the neutral radical upon deuteration will also contribute to the observed isotope shift in P(eKE) of Figure 4-3(b), since the isotope shift of the vibrational frequencies in the anion is expected to be smaller due to the more anharmonic anionic PES. A detailed examination of this explanation requires extensive *ab initio* calculations for vibrational frequencies and ZPEs on a global PES of $HOCO^-$ and $DOCO^-$, beyond the scope of the present study. On the other hand, little isotope effect was observed in the $P(E_T)$ distributions for the recoil of OD + CO neutral products, consistent with a predicted simultaneous reduction of ZPEs and O-D stretching frequencies when OH and HOCO are deuterated.[9]

It should be noted that although the experimental KE_{max} (line II) in Figure 4-3(a) is ~ 0.5 eV higher than the predicted value, the discrepancy between the theoretical KE_{max} and the most intense feature in the P(eKE, E_T) spectra of Figure 4-3(a) is less than 0.3 eV. Assuming a subset of the $HOCO^-$ anions are vibrationally excited by ~ 0.3 eV, the horizontal line set II representing the *c*-HOCO TS2 in Figure 4-2(a) will be raised by

the same amount, separating the two resolved structures annotated by 'A' and 'B' in the $H + CO_2 + e^-$ P(eKE, E_T) spectrum of Figure 4-2(a). This raises the possibility that vibrationally excited $HOCO^-$ anions also play a role in the apparent production of $H + CO_2 + e^-$ below the *c*-HOCO TS2 barrier. The $H + CO_2 + e^-$ products may be formed by two different mechanisms simultaneously: (1) DPD of vibrationally excited $HOCO^-$ produces nascent HOCO radicals above the dissociation barrier, followed by rapid unimolecular dissociation into $H + CO_2$ [feature A in Fig. 2(a)]; and (2) nascent HOCO radicals formed by the photodetachment of $HOCO^-$ with less vibrational excitation that tunnel through the *c*-HOCO TS2 barrier to form $H + CO_2$ [feature B in Figure 4-2(a)]. Assuming this mechanism, the spectrum in Figure 4-2(b) indicates that in the case of $DOCO^-$, the vibrationally excited anions play a more important role in $D + CO_2$ formation (feature A dominates) while the probability of tunneling is reduced greatly in the case of the D atom (feature B essentially disappears). An immediate result of this explanation for the isotope effect is that most $D + CO_2$ fragments are formed by passing over the *c*-HOCO TS2 barrier, yielding a narrower eKE spectrum and a shift in the P(E_T) distribution to higher E_T compared with the $H + CO_2 + e^-$ channel that includes a significant tunneling contribution.

An alternative mechanism is that the $H + CO_2 + e^-$ channel is solely produced by passing over the *c*-HOCO TS2 barrier during DPD of vibrationally excited $HOCO^-$ and there is no tunneling effect. This is less likely as it conflicts with the evidence for the tunneling mechanism from the measurement of the product branching ratios which will be discussed in detail below. In addition, this mechanism could not explain why feature (A) at eKE = ~0.9 eV and feature (B) at eKE = ~1.1 eV in the $H + CO_2 + e^-$ channel

merge into one narrower peak at eKE = ~1.0 eV in the D + CO_2 + e^- channel. Another possibility, mentioned earlier, that C_{2v} H·CO_2 is involved in the formation of either feature (A) or (B) can also be neglected even in the presence of anions with vibrational excitation up to ~0.3 eV, as this is not sufficient to overcome the TS4 barrier leading to the formation of C_{2v} H·CO_2. Therefore the only reasonable explanation is that upon deuterium substitution, feature (B) disappears as the tunneling mechanism is closed, while feature (A) formed by photodetachment of vibrationally excited anions shifts to higher eKE as observed in the other two channels forming OD + CO + e^- and DOCO + e^-.

The branching ratios for the three competing neutral product channels, stable HOCO, H + CO_2 and OH + CO, can help understand the reaction mechanisms discussed above. The most reliable approach to obtaining the branching ratios is to reproduce the overall P(eKE) spectra in Figure 4-4(a) by fitting the three channel-resolved eKE distributions determined in the PPC experiment, as shown in Figure 4-5. The branching ratios estimated by the eKE fitting in $HOCO^-$ and $DOCO^-$ measurements are listed in Table 4-2, along with the results from a previous DPD study of $HOCO^-$ at 258 nm and the recent calculations.

In general, both experiment and theory show that the majority of the neutral products in the DPD process of $HOCO^-$/$DOCO^-$ are stable HOCO or DOCO radicals, qualitatively consistent with the deep potential energy well of HOCO. Comparison of the H + CO_2 + e^- and D + CO_2 + e^- channels at E_{hv} = 3.21 eV shows a significant isotope effect as the branching ratio of this channel decreases by half in the deuterated measurement, consistent with a role for tunneling in this DPD channel as discussed above. An interesting observation is that the reduction of D + CO_2 fragments is accompanied by

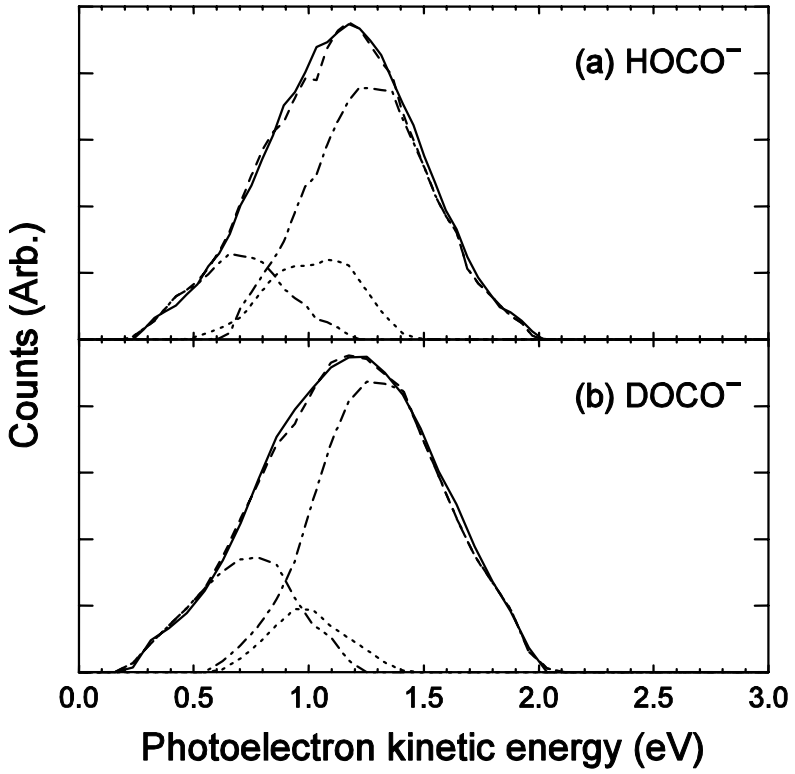

Figure 4-5: The fitting of overall P(eKE) distributions (solid line) by the three channel-resolved P(eKE) spectra shown in Figure 4-4. The dashed line represents the fitting result. The dash-dotted lines represent P(eKE) spectra in coincidence with stable HOCO/DOCO, with the dotted lines for the H/D + CO_2 and dot-dot-dashed lines for the OH/OD + CO channels. The areas of the three channel-resolved P(eKE) distributions are used to calculate relative branching ratios in the DPD of (a) $HOCO^-$ and (b) $DOCO^-$ at $E_{h\nu}$ = 3.21 eV.

Table 4-2: Branching ratios in DPD of $HOCO^-$

	stable HOCO	H + CO_2	OH + CO
258nm[a]	0.81	0.06	0.13
386nm[b]	0.67	0.16	0.17
386nm ($DOCO^-$)[b]	0.70	0.09	0.21
Theory (*trans*)[c]	0.86	0.03	0.11
Theory (*cis*)[b]	0.89	0.02	0.09

a) Ref. 7; b) The uncertainties of branching ratio are estimated to be ~10% of the listed value for the H/D + CO_2 and OH/OD + CO channels; c) 6D wavepacket calculations, Ref. 67.

an increase in the production of both stable DOCO and OD + CO. This can be explained by the predicted isotope effect on the HOCO PES. As calculated by Yu *et al.*, the ZPE of the OD + CO dissociation limit decreases by 0.06 eV compared with OH + CO, while the tunneling barrier *c*-HOCO TS2 is only reduced by 0.02 eV upon deuterium substitution (see Table 4-1).[9] As a result, on the DOCO PES, the OD + CO ground state is 0.09 eV lower than the TS2 barrier. Thus the excess nascent DOCO radicals arising from the elimination of tunneling would not only be trapped in the DOCO well, but also dissociate into ground state OD + CO, causing a simultaneous increase in the branching ratios of both OD + CO and stable DOCO.

Recently, Zhang *et al.* calculated branching ratios resulting from the DPD of $HOCO^-$ using six-dimensional quantum wavepacket dynamics on the LTSH surface.[67] The results are summarized in Table 4-2 for comparison with the experimental results. The theoretical work of Zhang *et al.* predicted that only 2-3% of neutral products are H +

CO_2, which differs significantly from the experimental values, 16% for H + CO_2 in DPD of $HOCO^-$ and 9% for D + CO_2 in DPD of $DOCO^-$. The theoretical branching ratio for OH + CO is also smaller than the experimental result. Consequently, the theoretical results predict that the stable HOCO product is more dominant. There are a number of potential explanations for these disagreements between theory and experiment. Based on the discussion above, the possible role played by vibrationally hot anions in the production of OH + CO and H + CO_2 products is neglected in these calculations. It was also found that the calculations effectively predict no tunneling leading to H + CO_2 products. This may be a consequence of the LTSH PES used in the wavepacket calculation not being sufficiently accurate in the critical region around the TS2 barrier separating *cis*-HOCO from H + CO_2 products.[13] In fact, as discussed by Zhang *et al.*,[67] although the energy of the *c*-HOCO TS2 on the LTSH surface is similar to that obtained from other high level *ab initio* calculations,[9] the LTSH surface predicts a thicker barrier, reducing the tunneling probability.[9,13] It should be noted as well that the LTSH surface was not optimized near the stationary points in the HOCO well, and in fact had to be significantly re-scaled to obtain a realistic Franck-Condon region.[7,67] Zhang *et al.* also carried out RRKM calculations on the branching ratios, yielding a ratio of 1:1.2 for OH + CO : H + CO_2. This is close to the ratio of 1.1:1 we found in the present E_{hv} = 3.21 eV DPD experiments on $HOCO^-$, but very different from the 2:1 ratio obtained in CCF's measurement using 4.80 eV photons.[7] The discrepancy between the two measurements at different photon energies is likely to be a result of the improved eKE resolution using a lower photon energy and the reduction of false coincidences by additional mass gating on the photofragment channels. It is clear that in spite of the impressive full-dimensional

calculations of Zhang *et al.*, a complete understanding of the DPD dynamics observed in these experiments will require more theoretical work. Accurate simulation of a DPD experiment requires fully characterized anion and neutral surfaces. In the case of the present experiments, the potential existence of vibrationally excited anions makes characterization of the anion surface even more important. A faithful representation of the present experimental results, including vibrationally excited $HOCO^-$, would require a reliable anion PES for *trans*- and *cis*-$HOCO^-$ in a range up to the OH^- + CO dissociation limit.

Zhang *et al.*'s wavepacket calculations also predicted energy distributions for the DPD of $HOCO^-$. In their results, the P(eKE) spectra for H + CO_2 + e^- channel shift ~0.5 eV to higher eKE from the experimental data. This is not surprising as vibrationally excited $HOCO^-$ anions were not taken into account and negligible tunneling was found in their work. Owing to the approach used by Zhang *et al.*, no prediction of the $P(E_T)$ for the H + CO_2 product channel was obtained. On the other hand, the theoretical $P(E_T)$ distributions for OH + CO products are consistent with the experiment, implying that the DPD of the ground state and vibrationally excited $HOCO^-$ produces nascent neutral HOCO radicals with very similar dissociation dynamics, possibly a result of significant vibrational adiabaticity on the neutral dissociation surface. Due to the limited Franck-Condon region predicted by the LTSH PES for neutral HOCO and the harmonic anion surface in Zhang *et al.*'s calculation, the DPD events they predicted mostly occur from the long tail extending towards the high energy side of the spectral density (Figigure 3 in Ref. 67). Therefore, a significant effect on the two DPD channels is expected if a more

realistic Franck-Condon region, including vibrationally excited anions on an anharmonic surface, becomes available.

4.4 Conclusion

Photoelectron-photofragment coincidence spectroscopy was employed to study the DPD dynamics of $HOCO^-$ and $DOCO^-$ at $E_{h\nu}$ = 3.21 eV, providing a useful method to probe the dynamics of the OH + CO $\rightarrow$ HOCO* $\rightarrow$ H + CO_2 reaction on the ground state potential energy surface. The dominant neutral product formed by photodetachment was found to be stable HOCO/DOCO free radicals trapped in a deep potential well, accompanied by two dissociation channels leading to H/D + CO_2 and OH/OD + CO products. It is suggested that both OH + CO and OD + CO products are formed by the DPD of vibrationally excited $HOCO^-/DOCO^-$. H + CO_2 products are produced by either the tunneling mechanism at total energies below the predicted dissociation barrier *c*-HOCO TS2 or unimolecular dissociation of nascent HOCO radicals above the *c*-HOCO TS2, formed by DPD of vibrationally excited $HOCO^-$. As a result, two resolved structures are observed in the PPC spectrum for H + CO_2 + e^-. Tunneling is reduced significantly in the $DOCO^-$ + hν $\rightarrow$ D + CO_2 + e^- DPD process and the vibrationally excited $DOCO^-$ anions become the major source of D + CO_2 products. The results presented in this study provide evidence in favor of the tunneling mechanism suggested by some of the previous kinetics studies on the OH + CO $\rightarrow$ H + CO_2 reaction at low temperature.[6,14,18,43] The proposed DPD mechanism is also supported by the product branching ratios. The recent quantum wavepacket dynamics predictions of Zhang *et al.* illustrate that full-dimensionality calculations on this four-atom system are now possible,

and can capture essential elements of the experimental results. More extensive calculations, however, are necessary for a detailed evaluation of the DPD mechanisms suggested by this study. In particular, accurate *ab initio* calculations to construct a complete anharmonic potential energy surface of $HOCO^-$ up to the OH^- + CO dissociation limit, as well as the stationary points for $DOCO^-$, are needed. In addition, the LTSH surface used in the simulations has known problems with the stationary points at the bottom of the HOCO well, so an improved neutral surface is also required. From an experimental perspective, a primary goal should be the elimination of any hot band contributions in the parent anions. A temperature-controlled ion trap for anion accumulation and cooling may be the best approach to solving this problem, as illustrated in a number of studies by Wang and co-workers.[82] Near-threshold photodetachment studies of $HOCO^-$ and $DOCO^-$ at a photon energy of 1.6 eV, characterizing the bottom of the HOCO well, will also be reported in the near future.[83]

References

1 T. Rockmann, C. A. M. Brenninkmeijer, G. Saueressig, P. Bergamaschi, J. N. Crowley, H. Fischer, and P. J. Crutzen, Science **281**, 544 (1998).

2 J. A. Miller, R. J. Kee, and C. K. Westbrook, Ann. Rev. Phys. Chem. **41**, 345 (1990).

3 A. D. McLean and Y. Ellinger, Chem. Phys. Lett. **98**, 453 (1983).

4 A. D. McLean and Y. Ellinger, Chem. Phys. **94**, 25 (1985).

5 T. V. Duncan and C. E. Miller, J. Chem. Phys. **113**, 5138 (2000).

[6] R. S. Zhu, E. G. W. Diau, M. C. Lin, and A. M. Mebel, J. Phys. Chem. A **105**, 11249 (2001).

[7] T. G. Clements, R. E. Continetti, and J. S. Franciso, J. Chem. Phys. **117**, 6478 (2002).

[8] K. R. Lykke, K. K. Murray, and W. C. Lineberger, Phys.Rev. A **43**, 6104 (1991).

[9] H.-G. Yu, J. T. Muckerman, and T. J. Sears, Chem. Phys. Lett. **349**, 547 (2001).

[10] G. C. Schatz, M. S. Fitzcharles, and L. B. Harding, Faraday Discuss. Chem. Soc. **84**, 359 (1987).

[11] K. Kudla, G. C. Schatz, and A. F. Wagner, J. Chem. Phys. **95**, 1635 (1991).

[12] K. S. Bradley and G. C. Schatz, J. Chem. Phys. **106**, 8464 (1997).

[13] M. J. Lakin, D. Troya, G. C. Schatz, and L. B. Harding, J. Chem. Phys. **119**, 5848 (2003).

[14] M. Aoyagi and S. Kato, J. Chem. Phys. **88**, 6409 (1988).

[15] Y. M. Li and J. S. Francisco, J. Chem. Phys. **113**, 7963 (2000).

[16] R. Valero, M. C. v. Hemert, and G.-J. Kroes, Chem. Phys. Lett. **393**, 236 (2004).

[17] X. Song, J. Li, H. Hou, and B. Wang, J. Chem. Phys. **125**, 094301 (2006).

[18] M. J. Frost, P. Sharkey, and I. W. M. Smith, J. Phys. Chem. **97**, 12254 (1993).

[19] J. R. Smith, J. B. Kim, and W. C. Lineberger, Phys.Rev. A **55**, 2036 (1997).

[20] D. A. Dixon, D. Feller, and J. S. Francisco, J. Phys. Chem. A **107**, 186 (2003).

[21] D. Feller, D. A. Dixon, and J. S. Francisco, J. Phys. Chem. A **107**, 1604 (2003).

[22] B. Ruscic, A. F. Wagner, L. B. Harding, R. L. Asher, D. Feller, D. A. Dixon, K. A. Peterson, Y. Song, X. M. Qian, C. Y. Ng, J. B. Liu, and W. W. Chen, J. Phys. Chem. A **106**, 2727 (2002).

[23] K. Kudla, A. G. Koures, L. B. Harding, and G. C. Schatz, J. Chem. Phys. **96**, 7465 (1992).

[24] M. I. Lester, B. V. Pond, M. D. Marshall, D. T. Anderson, L. B. Harding, and A. F. Wagner, Faraday Discuss. **118**, 373 (2001).

[25] D. E. Milligan and M. E. Jacox, J. Chem. Phys. **54**, 927 (1971).

[26] M. E. Jacox, J. Chem. Phys. **88**, 4598 (1988).

[27] D. Forney, M. E. Jacox, and W. E. Thompson, J. Chem. Phys. **119**, 10814 (2003).

[28] B. Ruscic, M. Schwarz, and J. Berkowitz, J. Chem. Phys. **91**, 6780 (1989).

[29] H. E. Radford, W. Wei, and T. J. Sears, J. Chem. Phys. **97**, 3989 (1992).

[30] T. J. Sears, W. M. Fawzy, and P. M. Johnson, J. Chem. Phys. **97**, 3996 (1992).

[31] T. J. Sears, H. E. Radford, and M. A. Moore, J. Chem. Phys. **98**, 6624 (1993).

[32] H. E. Radford, M. A. Moore, T. J. Sears, J. Grussdorf, J. Nolte, and F. Temps, J. Mol. Spectrosc. **165**, 137 (1994).

[33] J. T. Petty and C. B. Moore, J. Mol. Spectrosc. **161**, 149 (1993).

[34] J. T. Petty and C. B. Moore, J. Chem. Phys. **99**, 47 (1993).

[35] A. Miyoshi, H. Matsui, and N. Washida, J. Chem. Phys. **100**, 3532 (1994).

[36] M. E. Greenslade, M. Tsiouris, R. T. Bonn, and M. I. Lester, Chem. Phys. Lett. **354**, 203 (2002).

[37] M. D. Marshall, B. V. Pond, and M. I. Lester, J. Chem. Phys. **118**, 1196 (2003).

[38] M. J. Frost, P. Sharkey, and I. W. M. Smith, Faraday Discuss. **91**, 305 (1991).

[39] D. Fulle, H. F. Hamann, H. Hippler, and J. Troe, J. Chem. Phys. **105**, 983 (1996).

[40] D. M. Golden, G. P. Smith, A. B. McEwen, C. L. Yu, B. Eiteneer, M. Frenklach, G. L. Vaghjiani, A. R. Ravishankara, and F. P. Tully, J. Phys. Chem. A **102**, 8598 (1998).

[41] J. P. Senosiain, C. B. Musgrave, and D. M. Golden, Int. J. Chem. Kinet. **35**, 464 (2003).

[42] J. P. Senosiain, S. J. Klippenstein, and J. A. Miller, Proc. Combust. Inst. **30**, 945 (2005).

[43] W. C. Chen and R. A. Marcus, J. Chem. Phys. **123**, 094307 (2005).

[44] G. Paraskevopoulos and R. S. Irwin, J. Chem. Phys. **80**, 259 (1984).

[45] G. Paraskevopoulos and R. S. Irwin, Chem. Phys. Lett. **93**, 138 (1982).

[46] D. M. Sonnenfroh, R. G. Macdonald, and K. Liu, J. Chem. Phys. **94**, 6508 (1991).

[47] M. Alagia, N. Balucani, P. Casavecchia, D. Stranges, and G. G. Volpi, J. Chem. Phys. **98**, 8341 (1993).

[48] M. C. van Beek, K. Schreel, and J. J. ter Meulen, J. Chem. Phys. **109**, 1302 (1998).

[49] C. Y. Shi, L. Ren, and F. A. Kong, Chemphyschem **7**, 820 (2006).

[50] N. F. Scherer, C. Sipes, R. B. Bernstein, and A. H. Zewail, J. Chem. Phys. **92**, 5239 (1990).

[51] S. K. Shin, C. Wittig, and W. A. Goddard, J. Phys. Chem. **95**, 8048 (1991).

[52] S. I. Ionov, G. A. Brucker, C. Jaques, L. Valachovic, and C. Wittig, J. Chem. Phys. **99**, 6553 (1993).

[53] G. W. Flynn and R. E. Weston, J. Phys. Chem. **97**, 8116 (1993).

[54] M. Brouard, I. Burak, D. W. Hughes, K. S. Kalogerakis, J. P. Simons, and V. Stavros, J. Chem. Phys. **113**, 3173 (2000).

[55] D. C. Clary and G. C. Schatz, J. Chem. Phys. **99**, 4578 (1993).

[56] D. M. Medvedev, S. K. Gray, E. M. Goldfield, M. J. Lakin, D. Troya, and G. C. Schatz, J. Chem. Phys. **120**, 1231 (2004).

[57] E. M. Goldfield, S. K. Gray, and G. C. Schatz, J. Chem. Phys. **102**, 8807 (1995).

[58] D. H. Zhang and J. Z. H. Zhang, J. Chem. Phys. **103**, 6512 (1995).

[59] F. N. Dzegilenko and J. M. Bowman, J. Chem. Phys. **105**, 2280 (1996).

[60] H. G. Yu and J. T. Muckerman, J. Chem. Phys. **117**, 11139 (2002).

[61] D. A. McCormack and G. J. Kroes, Chem. Phys. Lett. **373**, 648 (2003).

[62] R. Valero, D. A. McCormack, and G. J. Kroes, J. Chem. Phys. **120**, 4263 (2004).

[63] R. R. Bernecker and F. A. Long, J. Phys. Chem. **65**, 1565 (1961).

[64] M. A. Haney and J. L. Franklin, Trans. Faraday Soc. **65**, 1794 (1969).

[65] B. Ruscic and M. Litorja, Chem. Phys. Lett. **316**, 45 (2000).

[66] T. M. Miller, A. A. Viggiano, A. E. S. Miller, R. A. Morris, M. Henchman, J. F. Paulson, and J. M. Vandoren, J. Chem. Phys. **100**, 5706 (1994).

[67] S. Zhang, D. M. Medvedev, E. M. Goldfield, and S. K. Gray, J. Chem. Phys. **125**, 164312 (2006).

[68] R. E. Continetti, Int. Rev. Phys. Chem. **17**, 227 (1998).

[69] J. A. Davies, J. E. LeClaire, R. E. Continetti, and C. C. Hayden, J. Chem. Phys. **111**, 1 (1999).

[70] J. A. Davies, R. E. Continetti, D. W. Chandler, and C. C. Hayden, Phys. Rev. Lett. **84**, 5983 (2000).

[71] M. S. Bowen and R. E. Continetti, J. Phys. Chem. A **108**, 7827 (2004).

[72] M. S. Bowen, M. Becucci, and R. E. Continetti, J. Phys. Chem. A **109**, 11781 (2005).

[73] D. P. DeBruijn and J. Los, Rev. Sci. Instrum. **53**, 1020 (1982).

[74] R. E. Continetti, D. R. Cyr, D. L. Osborn, D. J. Leahy, and D. M. Neumark, J. Chem. Phys. **99**, 2616 (1993).

[75] B. L. Peko and T. M. Stephen, Nucl. Instrum. Methods Phys. Res. B **171**, 597 (2000).

[76] T. G. Clements, Ph. D. thesis, University of California, San Diego, 2002.

[77] G. Herzberg, *Molecular spectra and molecular structure II. Infrared and raman spectra of polyatomic molecules*. (Krieger Publishing, Malabar, Florida, 1991).

[78] T. G. Clements and R. E. Continetti, J. Chem. Phys. **115**, 5345 (2001).

[79] E. H. Kim, S. E. Bradforth, D. W. Arnold, R. B. Metz, and D. M. Neumark, J. Chem. Phys. **103**, 7801 (1995).

[80] J. B. Kim, P. G. Wenthold, and W. C. Lineberger, J. Chem. Phys. **108**, 830 (1998).

[81] Z. Lu and R. E. Continetti, J. Phys. Chem. A **108**, 9962 (2004).

[82] X. B. Wang, H. K. Woo, L. S. Wang, B. Minofar, and P. Jungwirth, J. Phys. Chem. A **110**, 5047 (2006).

[83] Z. Lu and R. E. Continetti, Phys. Rev. Lett., In press (2007).

Chapter Acknowledgement

This chapter, in full, is a reproduction of the material as it appears in Z. Lu, Q. Hu, J.E. Oakman and R.E. Continetti, "Dynamics on the HOCO potential energy surface studied by dissociative photodetachment of $HOCO^-$ and $DOCO^-$," J. Chem. Phys. **126**, 194305-1 − 11 (2007). Copyright 2007 American Institute of Physics. The dissertation author was the investigator for this paper.

Chapter 5

Alignment of a Molecular Anion via a Shape Resonance in Near-Threshold Photodetachment

Molecular orientation and alignment have long been recognized as key factors determining the probability of bimolecular, molecule-surface, and molecule-electromagnetic field interactions. In the past few decades, the control of molecular alignment has been a major research focus, with the ultimate goal of manipulation of chemical reactivity.[1,2] However, previous studies generally focused on neutral molecules, with few experimental efforts that target negative ions. This chapter illustrates the alignment of a molecular anion via a shape resonance in near-threshold photodetachment for the first time. The phenomenon reported here may prove to be general for molecular anions in which the dominant photodetachment channel above threshold produces free electrons with non-zero angular momentum. The work should be of general interest as it may open new avenues for the study of electron-neutral interactions and the manipulation of chemically important transient neutral species produced by the photodetachment of anion precursors.[3]

Several approaches have been applied to the alignment and orientation of neutral molecules. A hexapole (Ref. 4) or strong homogeneous electrostatic field (Ref. 5) can create oriented molecules with large dipole moments. Recently, alignment of general classes of molecules has been reported using a strong laser field on the induced dipole moment.[6,7] An alternative laser control approach utilizes resonant optical transitions with polarized light.[8] Since the transition dipoles in the molecular frame (MF) have specified

directions, an anisotropic excited-state molecular ensemble can be generated by the interaction with electromagnetic radiation, leaving the remaining ground-state molecules with an anisotropic distribution as well. Although this type of alignment is not as strong as that achieved by the non-resonant strong laser field, it only requires moderately intense laser pulses and has the advantage of quantum-state-selectivity. As a result, it has been widely applied in the study of photoionization dynamics and rotational wave packet revival.[9-13] The application of this technique to the alignment of molecular anions, however, has seen limited success owing to the paucity of bound excited states in anions. In this chapter, we demonstrate a novel approach to align a molecular anion through a shape resonance near the photodetachment threshold.

In the atomic approximation for photodetachment, the effective potential between a photoelectron and the molecular core can be approximated by a radial form: $V_{eff}(r) = V(r) + l(l+1)\hbar^2 / 2\mu r^2$;[14] where the first term, *V(r)*, represents the weak electron-neutral attractive potential, the second term describes a centrifugal barrier, l is the angular momentum quantum number for the photoelectron partial wave, and μ is the reduced mass. Unlike the dominant Coulomb attraction between the departing electron and cation core in the photoionization of neutral molecules, *V(r)* in anion photodetachment decays faster than r^{-2} when r increases. Consequently, when low energy photoelectrons are produced in near-threshold photodetachment, *s*-wave photoelectrons ($l = 0$) dominate, while electrons with $l > 0$ are trapped by the centrifugal barrier, forming a temporary anion with the excess electron weakly bound to the neutral core. The lifetime of such a shape resonance can vary from ~10^{-15} to ~10^{-10} s.[15] In a molecular anion, V_{eff} is expected to depend on the MF instead of being a purely central

potential. Therefore with a short-pulsed laser or two laser pulses, the alignment of a molecular anion can be realized through a shape resonance with an excitation photon near the photodetachment threshold, and be detected by photodetachment of the temporary anion using a second photon and measuring the resulting laboratory-frame (LF) PAD.

This approach was applied in the present study to align a polyatomic anion, $HOCO^-$. Previously the one-photon detachment of $HOCO^-$ at $E_{h\nu}$ = 4.80 eV and 3.21 eV has been used to probe the potential energy surface of the bimolecular reaction OH + CO ↔ HOCO → H + CO_2.[16,17] Two planar isomers were reported for both the anionic and neutral HOCO, with a*b initio* calculations predicting adiabatic electron affinities (AEA) of 1.30 and 1.43 eV for *trans*- and *cis*-HOCO, respectively.[16] In the current work, the energy-resolved PAD from one and two-photon detachment of $HOCO^-$ at $E_{h\nu}$ = 1.60 eV was obtained, showing evidence for the alignment of $HOCO^-$ by photoabsorption near the detachment threshold. The observed two-photon LF-PAD provides valuable insights into the photodetachment dynamics.

5.1 Experiment

The experimental details have been described elsewhere,[16,17] and will only be briefly reviewed here. The $HOCO^-$ anions were generated in a supersonic expansion of a gas mixture (7% CO, 6% N_2O, 17% CH_4, and 70% N_2) crossed by a 1 keV electron beam. The anion beam was then accelerated to 10 keV, and mass selected by time-of-flight. The $HOCO^-$ (*m/e* = 45) beam was crossed by the fundamental (772 nm, $E_{h\nu}$ = 1.60 eV) of a Ti:Sapphire laser (Clark-MXR CPA-2000, 1.8 ps FWHM, 1 kHz). The laser power density in the photon-ion interaction volume was estimated to be ~ 6 x 10^{10} W/cm^2.

Photoelectrons ejected over the 4π sr solid angle were collected by a space focusing electron optics assembly (Ref. 11) and recorded on an event-by-event basis with a time- and position-sensitive detector parallel to the plane of the ion and laser beams, yielding angle-resolved photoelectron kinetic energy (eKE) distributions. The electron detector was calibrated by photodetachment of O^- at E_{hv} = 1.60 eV (eKE = 0.14 eV, FWHM = 0.06 eV). The neutral fragments produced by photodetachment were registered by another time- and position-sensitive detector, allowing coincidence studies of the dissociative photodetachment that will not be considered further in this chapter.

5.2 Results and Discussions

Figure 5-1(a) shows the angle-integrated P(eKE) spectrum. Two narrow peaks (I) at 0.01 eV and (II) at 0.09 eV, along with a broad peak (III) ranging from ~0.4 eV to ~1.9 eV are observed. A comparison between peak (III) and the P(eKE) obtained in a previous study at E_{hv} = 3.21 eV shows great similarity.[17] Noting the maximum eKE in the one-photon detachment at E_{hv} = 1.60 eV should be 0.30 eV for *trans*- and 0.17 eV for *cis*-$HOCO^-$ using previously calculated AEAs,[16,17] the energetic photoelectrons in peak (III) can only result from two-photon detachment of $HOCO^-$. This was further verified by reducing the laser power by ~60%. Assuming no competition between one- and two-photon processes, the signal intensities I_{1hv} and I_{2hv} are proportional to the first and second order of the laser power, respectively, so the intensity ratio I_{2hv}/I_{1hv} is also expected to drop by 60%. In this experiment, the intensity of peak (III) compared to the

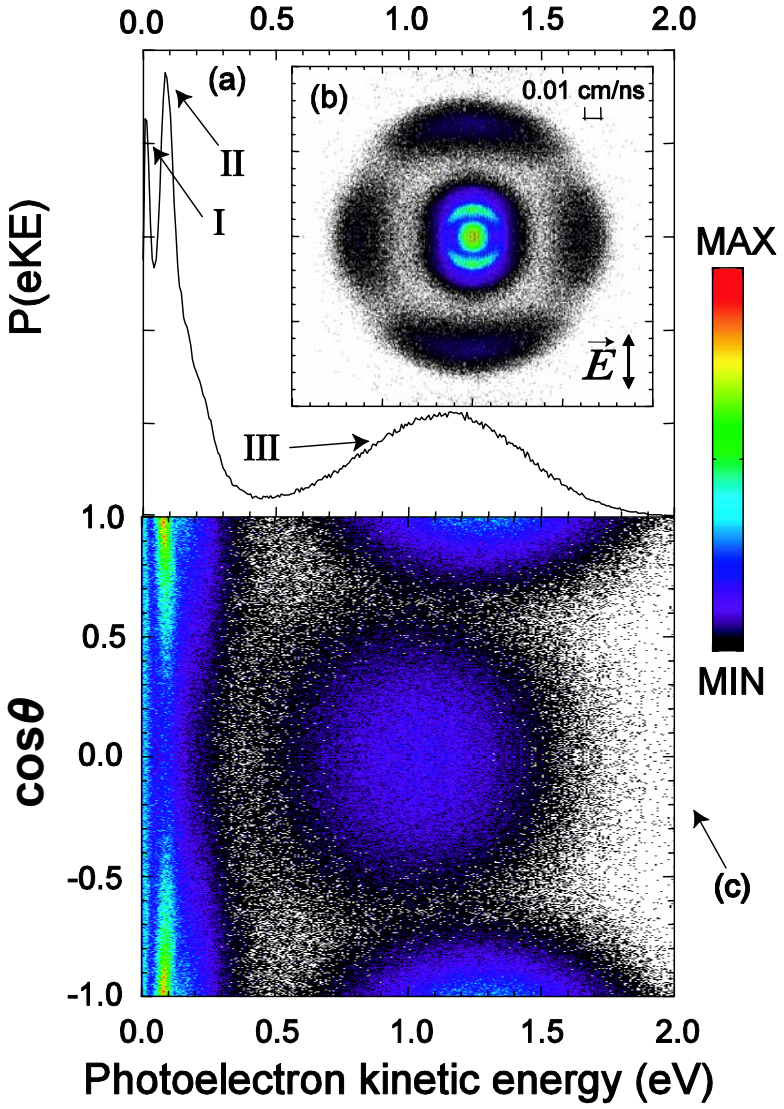

Figure 5-1: (a) The angle-integrated P(eKE) spectrum of photodetachment of $HOCO^-$ at $E_{h\nu}$ = 1.6 eV. The peaks (I) and (II) correspond to the one-photon signals and peaks (III) corresponds to the two-photon signal. (b) The projection of 3D Photoelectron velocities on the 2D electron detector, with the laser $\vec{E}$ vector along the ordinate. (c) The eKE-resolved PAD plotted in P(eKE, cosθ), where θ is the electron recoil angle referenced to the laser $\vec{E}$ vector parallel to the direction of ion beam propagation.

sum of peaks (I) and (II) dropped by over 70%, consistent with the two-photon process "bleaching" the one-photon signal. The fine structure resolved in the near-threshold one-photon detachment [Peaks (I) and (II)] may originate from the coexistence of *cis*- and *trans*-$HOCO^-$ in the ion beam or O-C-O bending vibrations in HOCO. A significant portion of the one-photon signal is seen to extend to ~0.4 eV, possibly a result of the uncertainty of the predicted AEA values and the presence of vibrationally excited $HOCO^-$ in the parent ion beam as discussed in a previous study,[17] though the rotational temperature of the $HOCO^-$ is expected to be low.

The photodetachment dynamics are revealed by the LF-PAD. Figure 5-1(b) shows the projection of the measured 3D photoelectron velocities on the 2D electron detector, with the laser $\vec{E}$ vector along the ordinate. The isotropic "disc" at the center of the image corresponds to peak (I) in Figure 5-1(a), consistent with the *s*-wave photoelectrons expected to dominate in near-threshold anion photodetachment.[18] The two lobes next to the center show that the electrons in peak (II) are ejected along the laser $\vec{E}$ vector, consistent with dominant *p*-wave photodetachment above threshold, as seen previously at higher photon energies.[16,17] The unique four-fold outer ring corresponds to the two-photon signals. Unlike in the one-photon detachment at E_{hv} = 3.21 eV,[17] photoelectrons generated by absorbing two 1.60 eV photons have both parallel and perpendicular LF-PAD components. The eKE-dependence of the LF-PAD can be viewed in a 2D histogram P(eKE, cosθ) as shown in Figure 5-1(c), where the intensity of each point represents the number of events corresponding to a certain eKE and the cosine of the electron recoil angle θ relative to the laser $\vec{E}$ vector. In the two-photon signal, the photoelectrons with the

perpendicular PAD have a P(eKE) peak around 1.0 eV, shifted away from those with the parallel PAD peaking at ~1.2 eV.

A more quantitative understanding of the two-photon photodetachment dynamics can be achieved by fitting the eKE-resolved LF-PAD to the following equation:[19]

$$I(\theta, eKE) = \frac{\sigma(eKE)}{4\pi}[1 + \beta_2(eKE)P_2(\cos\theta) + \beta_4(eKE)P_4(\cos\theta)], \quad (5\text{-}1)$$

where *σ(eKE)* is the total cross section at a certain eKE, P_2 and P_4 are second- and fourth-order Legendre polynomials, β_2 and β_4 represent energy-dependent anisotropy parameters. When β_2 and β_4 are zero, only *s*-wave photodetachment occurs and an isotropic PAD is observed. In the case of interfering *s*- and *d*-waves,[20] β_2 and β_4 are restricted by:

$$9\beta_2^2 - 10\beta_2\beta_4 + 30\beta_4^2 - 70\beta_4 \le 0. \quad (5\text{-}2)$$

The one-photon photodetachment can also be described by equation (5-1) with $\beta_4 = 0$ and β_2 ranging from -1 [$I(\theta, eKE) \propto \sin^2\theta$] to 2 [$I(\theta, eKE) \propto \cos^2\theta$].[21]

The β_2(eKE) and β_4(eKE) distributions are obtained by fitting the observed PAD using equation (5-1). The results are summarized in Figure 5-2. At low eKE, β_4 fluctuates around zero, consistent with one-photon photodetachment and no apparent anion polarization by the electric field of laser. When eKE ≤ 0.04 eV, β_2 is nearly zero. The β_2 values then rapidly increase to 0.9 at eKE ~ 0.09 eV, which corresponds to the peak (II) in Figure 5-1(a). There is another minimum at eKE = 0.13 eV where β_2 ~ 0.6, followed by a slow increase of β_2 to a maximum of ~ 0.9. The positive β_2 values ranging from 0 to 1 in the one-photon detachment imply a mixing of *s*- (l = 0) and *p*- (l = 1) partial wave continuum electrons in the atomic approximation, with the low-energy *p*-wave photoelectrons suppressed by the centrifugal barrier, causing β_2 ~ 0 at small eKE. The

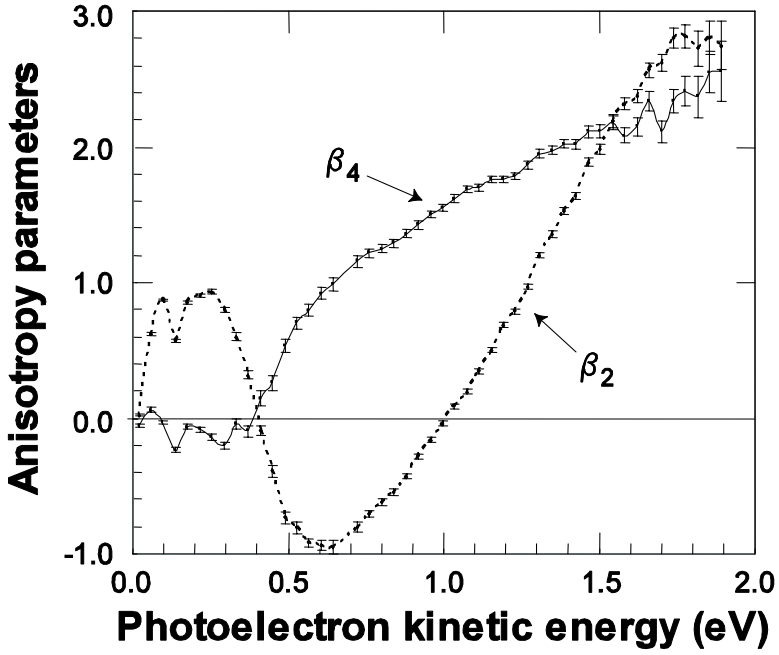

Figure 5-2: The β_2(eKE) and β_4(eKE) functions obtained by fitting the experimental LF-PAD with equation (5-1), including 1 σ error bars.

rapid increase of β_2 above eKE = 0.04 eV should be related to the height of the centrifugal barrier for l = 1. Since *p*-wave electrons may tunnel through the centrifugal barrier, it is reasonable to assign 0.04 eV as a lower limit for the height of the *p*-wave centrifugal barrier.

When the two-photon process dominates at eKE ≥ 0.40 eV, β_4 increases to an unusually large positive value for a molecular anion, indicating significant alignment of the temporary $HOCO^-$ anion. Since there is no centrifugal barrier for *s*-wave photoelectrons and a picosecond laser was used in the present study, the most likely mechanism is that when $HOCO^-$ absorbs the first photon, *s*-wave photoelectrons as well

as the fast *p*-wave photoelectrons escape the molecular core, while slow *p*-type electrons are temporarily trapped by the centrifugal barrier and detached by a second photon. This mechanism is also consistent with the observation that the increased two-photon signal comes at the expense of the one-photon signal. In the absence of absorption of a second photon during the 1.8 ps laser pulse, the temporary anion produced by the shape resonance can later decay by electron tunneling through the centrifugal barrier. Thus, the observed alignment of $HOCO^-$ presented here is assigned to a sequential two-photon process using the temporary anion formed by an $l = 1$ shape resonance as the intermediate state, and is expected to have an angular distribution proportional to $\cos^2\theta$ relative to laser $\vec{E}$ vector as suggested by the previous time-resolved photoionization experiments.[12] According to the $\Delta l = \pm 1$ atomic selection rule, photodetachment of the *p*-type electrons will result in an interference of *s*- and *d*-wave free electrons. This atomic approximation is seen to be valid in the molecular case under investigation as equation (2) holds well for the measured β_2 and β_4 values in an eKE range up to 1.7 eV, possibly because of the relatively large size of the excess electron orbital with respect to the molecular core in the temporary anion. In fact, the patterns shown in Fig. 1(c) are similar to those reported in a previous above-threshold two-photon photodetachment study of atomic H^- using a strong laser field, which solely involves mixing *s*- and *d*-partial wave photoelectrons [22]. When eKE > 1.7 eV, the experimental β_2 and β_4 no longer satisfy equation (2) as a result of larger measurement uncertainties at high eKE.

Quantitatively, the PAD in the two-photon detachment can be decomposed into photoelectron partial waves as:

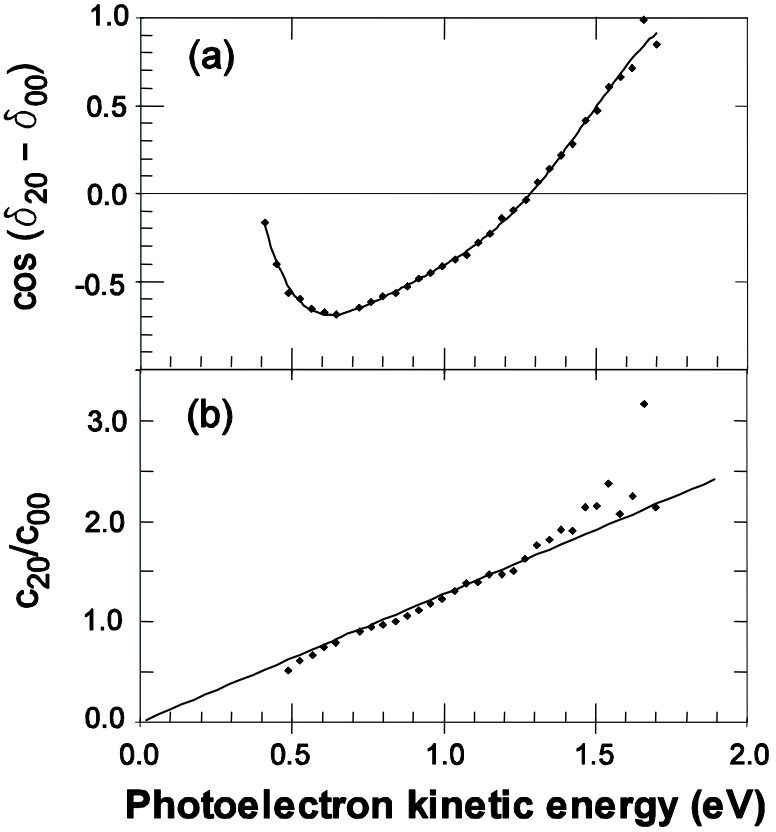

Figure 5-3: (a) Cosines of the phase shift difference, $\cos(\delta_{20} - \delta_{00})$; and (b) the ratios of the radial transition coefficients, c_{20}/c_{00} *vs.* eKE for continuum *s*- and *d*-wave photoelectrons produced in the two-photon process. The solid line in (a) is obtained by fitting the data with a sixth order polynomial. The solid line in (b) shows the linear relationship of c_{20}/c_{00} with eKE that is consistent with the Wigner threshold law for photodetachment.

$$I(\theta,\phi) \propto \left|\psi_e\right|^2, \qquad \psi_e = \sum_{lm} c_{lm} e^{i\delta_l} Y_{lm}(\theta,\phi), \tag{5-3}$$

where the coefficient c_{lm} is determined by the radial component of the dipole transition and has a non-negative real value, δ_l is a phase-shift, and $Y_{lm}(\theta,\phi)$ is the corresponding spherical harmonic.[19] With a linearly polarized laser, only m = 0 contributes, and assuming only *s*- and *d*-partial wave contributions, a ratio of c_{20}/c_{00}, as well as a phase difference $(\delta_{20}-\delta_{00})$ with an uncertain sign, can be determined for each set of β_2 and β_4 by comparing equations (5-1) and (5-3).[19,20] Figure 5-3 shows c_{20}/c_{00} and $\cos(\delta_{20}-\delta_{00})$ as functions of eKE. An interesting observation is that the experimental c_{20}/c_{00} values are linearly proportional to eKE up to ~1.3 eV, in good agreement with the Wigner law for near-threshold photodetachment: $\sigma_l = \left|c_l\right|^2 \propto (eKE)^{l+1/2}$.[18] This is consistent with the interference of *s*- and *d*-partial waves generated by photodetachment of the temporary anion supported by the l = 1 shape resonance leading to the molecular alignment implied by the eKE-dependent LF-PAD of the two-photon signal.

5.3 Conclusion

In conclusion, the two-photon detachment of $HOCO^-$ at E_{hv} = 1.60 eV shows that it is possible to use a shape resonance near the photodetachment threshold to align a molecular anion. In this study, the excitation and probe laser pulses have the same linear polarization. Further experiments using different polarization geometries or two-color pump and probe lasers may yield more insights into the photodetachment dynamics,[19]

along with direct measurements of the photofragment angular distributions to quantify the alignment. Additionally, time-resolved PAD measurements may help characterize the resonance lifetimes that play an essential role in this type of alignment, and the time-evolution of the alignment as a result of molecular rotation that tests the sensitivity of the PAD to the alignment.[12,19] This phenomenon may prove to be general for molecular anions dominated by *p*- or higher *l*-wave photodetachment above threshold.

References

1 R. N. Zare, Science **279**, 1875 (1998).

2 J. J. Larsen, I. Wendt-Larsen, and H. Stapelfeldt, Phys. Rev. Lett. **83**, 1123 (1999).

3 D. M. Neumark, J. Chem. Phys. **125**, 132303 (2006).

4 D. H. Parker and R. B. Bernstein, Annu. Rev. Phys. Chem. **40**, 561 (1989).

5 B. Friedrich and D. R. Herschbach, Nature **353**, 412 (1991).

6 B. Friedrich and D. Herschbach, Phys. Rev. Lett. **74**, 4623 (1995).

7 E. Peronne, M. D. Poulsen, C. Z. Bisgaard, H. Stapelfeldt, and T. Seideman, Phys. Rev. Lett. **91**, 043003 (2003).

8 R. C. Estler and R. N. Zare, J. Am. Chem. Soc. **100**, 1323 (1978).

9 D. J. Leahy, K. L. Reid, and R. N. Zare, J. Chem. Phys. **95**, 1757 (1991).

10 D. Townsend and K. L. Reid, J. Chem. Phys. **112**, 9783 (2000).

11 J. A. Davies, R. E. Continetti, D. W. Chandler, and C. C. Hayden, Phys. Rev. Lett. **84**, 5983 (2000).

12 M. Tsubouchi, B. J. Whitaker, L. Wang, H. Kohguchi, and T. Suzuki, Phys. Rev. Lett. **86**, 4500 (2001).

[13] O. Gessner, A. M. D. Lee, J. P. Shaffer, H. Reisler, S. V. Levchenko, A. I. Krylov, J. G. Underwood, H. Shi, A. L. L. East, D. M. Wardlaw, E. T. Chrysostom, C. C. Hayden, and A. Stolow, Science **311**, 219 (2006).

[14] J. W. Farley, Phys. Rev. A **40**, 6286 (1989).

[15] L. Sanche and G. J. Schulz, J. Chem. Phys. **58**, 479 (1973).

[16] T. G. Clements, R. E. Continetti, and J. S. Francisco, J. Chem. Phys. **117**, 6478 (2002).

[17] Z. Lu, Q. Hu, J. E. Oakman, and R. E. Continetti, J. Chem. Phys. **126**, 194305 (2007).

[18] E. P. Wigner, Phys. Rev. **73**, 1002 (1948).

[19] K. L. Reid, Annu. Rev. Phys. Chem. **54**, 397 (2003).

[20] D. A. Telnov and S. I. Chu, Phys. Rev. A **66**, 043417 (2002).

[21] J. Cooper and R. N. Zare, J. Chem. Phys. **48**, 942 (1968).

[22] R. Reichle, H. Helm, and I. Y. Kiyan, Phys. Rev. Lett. **87**, 243001 (2001).

Chapter Acknowledgement

This chapter, in full, is a reproduction of the material as it appears in Z. Lu and R.E. Continetti, "Alignment of a molecular anion via a shape resonance in near-threshold photodetachment," Phys. Rev. Lett. in press (2007). Copyright 2007 American Physical Society. The dissertation author was the investigator for this paper.

Chapter 6

Photoelectron-Photofragment Angular Correlations in Dissociative Photodetachment of $HOCO^-$

Dissociative photodetachment (DPD) of negative ions has become a unique and versatile tool for the study of the dynamics of gas-phase transient species.[1,2] In a typical DPD process, electrons are photoejected from parent anions, producing neutral transient species that can further dissociate into two or more photofragments. A coincidence measurement of the translational energy partitioning among photoelectron and photofragments from the same DPD event can yield deep insight into the dissociation dynamics on the involved potential energy surfaces (PES).[1,3] Complementary to the recording of energy partitioning, measurement of photoelectron and photofragment angular distributions is another powerful probe of the DPD dynamics.[3-5] In this chapter we extend such measurements to the $HOCO^-$ and $DOCO^-$ molecular anions used to probe the $OH + CO \rightarrow H + CO_2$ reaction.

Under the electric-dipole approximation, the photodetachment probability is dictated by:

$$I \propto \left| < \varphi_{ele} \cdot \varphi_f \left| \vec{\mu} \cdot \vec{E} \right| \varphi_i > \right|^2 = \left| \vec{M} \cdot \vec{E} \right|^2 , \tag{6-1}$$

where $\vec{\mu}$ is the dipole moment operator, $\vec{E}$ is the laser electric field, φ_{ele}, φ_f, and φ_i are the wave-functions of the free electron, the neutral products, and the parent anion, respectively, and $\vec{M} = < \varphi_{ele} \cdot \varphi_f \left| \vec{\mu} \right| \varphi_i >$ is the transition dipole moment. In general, the parent anions are isotropically distributed before interacting with photons, while the laser

polarization is spatially fixed and defines the laboratory frame (LF). The transition dipole moment has specific direction in the molecular frame (MF). As a result, based on equation (6-1), the angular distribution of the nascent neutral product in terms of the dipole transition moment is proportional to $\cos^2\chi$, in which χ is the angle between $\vec{E}$ and $\vec{M}$.[6] In addition, the transition dipole moment matrix $\vec{M}$ contains the amplitude and phase information of the photoelectron partial waves that determine the MF photoelectron angular distributions (PAD).[7] As a result, the angular distributions of outgoing electrons, molecular axes of the parent anions and neutral products, and laser polarizations are all correlated with each other.

The LF-PAD has been widely used to provide qualitative information such as the molecular symmetry and photodetachment dynamics for DPD as well as other photodetachment processes.[2,8,9] However, significant information is lost due to the averaging over the randomly oriented parent anions. Noting that there exist two or more neutral dissociation fragments in a DPD process, one approach to the problem mentioned above is to record the PAD in coincidence with the angular distribution of the neutral photofragments. By this method, one can obtain experimentally the PAD in the photofragment recoil frame (RF), which in general contains more detailed dynamics information than the LF-PAD.[10] Specifically, if the dissociation occurs immediately following the photoelectron ejection and the photofragments have an anisotropic angular distribution, the recoil angles of photofragments are directly related to the orientations of the breaking bonds at the moment of photoabsorption. In this case, measurement of the RF-PAD may help examine the interactions between the outgoing electron and the molecular core.[4,5] On the other hand, if the LF angular distribution of neutral

photofragments is relatively isotropic, the RF-PAD will also tend to be isotropic and the analysis of RF-PAD and LF photofragment angular distribution may yield important dynamics information such as the lifetime of the nascent neutral product and the orientation of transition dipole in the molecular frame. Therefore, the measurement of the angular correlations between the photoelectrons and the neutrals as well as their angular distributions with respect to the laser polarization will reveal the DPD dynamics implied by Equation (6-1).

The current study focuses on the photoelectron-photofragment angular correlations in the DPD of a polyatomic anion, $HOCO^-$. With photoelectron-photofragment coincidence (PPC) spectroscopy, the DPD of $HOCO^-$ has been used to explore the PES of OH + CO → [HOCO]* → H + CO_2,[11,12] a fundamentally important hydrocarbon combustion reaction that also regulates the OH, CO, and CO_2 concentrations in low atmosphere.[13,14] A number of previous studies have shown that along the minimum-energy OH + CO reaction path, there exists a stable HOCO intermediate followed by a high reaction barrier before forming H + CO_2,[15-17] with an exoergicity relative to OH + CO of -1.05 eV at 0K.[18] In addition, two planar isomers, the *cis*- and *trans*- conformers were predicted for both the HOCO free radical and the $HOCO^-$ anion.[11,16-18] Previous studies of the HOCO radical have been recently reviewed in detail in Reference 12.

In this laboratory, the photodetachment of $HOCO^-$ has been used to access the PES of HOCO radical at $E_{h\nu}$ = 4.80 eV and 3.21 eV, with three neutral product channels observed: [11,12]

$$HOCO^- + h\nu \rightarrow HOCO + e^-; \qquad (6\text{-}2)$$

$$HOCO^- + h\nu \rightarrow OH + CO + e^-; \quad (6\text{-}3)$$

$$HOCO^- + h\nu \rightarrow H + CO_2 + e^-. \quad (6\text{-}4)$$

The measured channel-resolved photoelectron kinetic energy (eKE) spectra and PPC spectra reveal that the dominant photodetachment channel yields the stable HOCO free radical, consistent with the prediction of a deep HOCO potential well. At $E_{h\nu}$ = 3.21 eV, PPC spectra and branching ratios for the DPD of $HOCO^-$ and its deuterated form $DOCO^-$ show evidence for a tunneling mechanism in the production of H + CO_2. Comparison of the PPC spectra with calculated energetics and dynamics calculations indicated that DPD of vibrationally excited $HOCO^-/DOCO^-$ also contribute to the production of H/D + CO_2, and is the major source of the OH/OD + CO + e^- products. [12,19]

With the adiabatic electron affinities (AEAs) of the *cis*- and *trans*-HOCO predicted to be 1.43 eV and 1.30 eV respectively,[11] the near-threshold photodetachment of $HOCO^-$ was also carried out at $E_{h\nu}$ = 1.60 eV to probe the bottom of the HOCO potential well.[20] In addition to two sharp peaks resolved near threshold, a broad peak around 1.2 eV was observed and assigned to a two-photon photodetachment process. The eKE-dependent LF-PAD revealed that the one-photon photoelectron signal is composed of mixing *s*- and *p*- partial waves, while *p*-wave photodetachment becomes more dominant at higher eKE. The two-photon photodetachment was shown to be accompanied by a unique four-fold LF-PAD, interpreted as the interfering *s*- and *d*-partial wave photoelectrons resulting from the photodetachment of an aligned temporary anion formed by the *p*-wave shape resonance near threshold. The relative amplitude and phase shift between *s*- and *d*-partial waves were obtained by a quantitative analysis of the two-

photon LF-PAD, showing good agreement with the Wigner threshold law, as reported in Ref. 20.

This chapter presents further investigation of the DPD dynamics of $HOCO^-$ and $DOCO^-$ by examination of photoelectron, photofragment angular distributions and photoelectron-photofragment angular correlations. Following a brief description of the experimental methods, the RF-PAD of both the $HOCO^- + h\nu \rightarrow OH + CO + e^-$ and $HOCO^- + h\nu \rightarrow H + CO_2 + e^-$ channels will be discussed. The LF neutral photofragment angular distribution of OH/OD + CO, from the one-photon photodetachment at $E_{h\nu}$ = 3.21 eV and two-photon process at $E_{h\nu}$ = 1.60 eV will be presented. The RF-PAD will be compared with the corresponding LF-PAD. The relationship between the RF-PAD and the OH + CO recoil angles will also be examined. These results will be used to estimate the lifetime of the HOCO free radical and the orientation of transition dipole moment. Further evidence for the alignment of $HOCO^-$ in the two-photon DPD process will also be presented.

6.1 Experiment

The experiments were carried out with a fast-ion-beam photoelectron-photofragment coincidence spectrometer which has previously been described in detail.[3,11,12,20] Therefore the experimental methods will only be briefly reviewed here. The $HOCO^-$ was formed by crossing the 1 kHz pulsed supersonic expansion of a gas mixture (7% CO, 6% N_2O, 17% CH_4, and 70% N_2) with a 1 keV electron beam. In the $DOCO^-$ experiment, CH_4 was replaced by CD_4 (99%, Cambridge Isotope Laboratory). The negative ions were then skimmed, accelerated to 10 keV, and referenced to ground

potential by a high voltage switch. The $HOCO^-$ with m/e = 45 (m/e = 46 for $DOCO^-$) was mass selected by time-of-flight (TOF) and perpendicularly intercepted by a linearly polarized laser pulse. Two wavelengths, the fundamental (772 nm, $E_{h\nu}$ = 1.60 eV, ~5 x 10^{10} W/cm^2) and second harmonic (386 nm, $E_{h\nu}$ = 3.21 eV, ~1 x 10^{10} W/cm^2) from a Ti:Sapphire laser (Clark-MXR CPA-2000, 1.8 ps FWHM, 1 kHz) were used for the photodetachment measurements. The laser was linearly polarized, with $\vec{E}$ fixed to be parallel to the ion beam propagation direction.

A space focusing electron optics assembly was applied to collect the full 4π sr solid angle of photoelectrons. [21] The three dimensional (3D) velocities of photoelectrons were measured by a time- and position-sensitive detector placed parallel to the plane of laser and ion beams, allowing a straightforward detection of the PADs. The photoelectron detector was calibrated by the photodetachment of OH^- at 386 nm and O^- at 772 nm, with ΔE (full-width-at-half-maximum (FWHM)) = 0.18 and 0.06 eV at eKE = 1.38 and 0.14 eV, respectively. To remove the detector inhomogeneity in the LF-PAD, the data were symmetrized in the dimension along the ion beam propagation by an averaging procedure: $\bar{N}(\theta_{LF}) = \frac{1}{2}[N(\theta_{LF}) + N(180^\circ - \theta_{LF})]$. Here θ_{LF} is the laboratory frame angle between the photoelectron ejection and ion beam propagation [Figure 6-1(a)].

Undetached negative ions were deflected out of the original ion beam direction by an electrostatic field and recorded by an ion detector. The neutral photofragments formed by photodetachment impinged on a time- and position-sensitive detector that is located 1.4 m away from the laser interaction region and perpendicular to the ion beam propagation. The masses and the 3D velocities in the center of mass (CM) frame for the

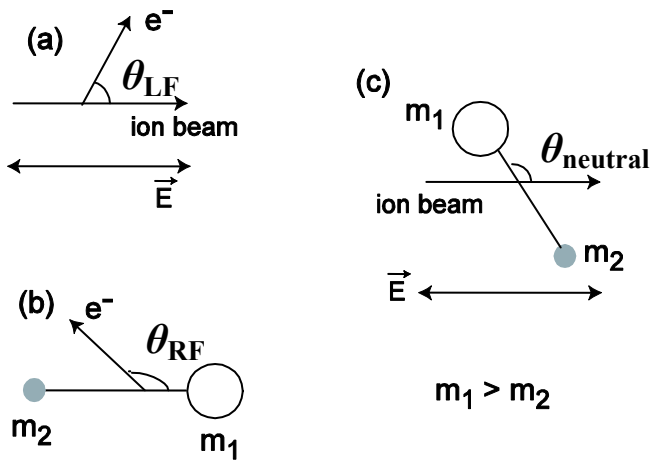

Figure 6-1: Angle definitions used in this chapter: (a) θ_{LF}, the laboratory frame (LF) photoelectron ejection angle with respect to ion beam propagation as well as the laser $\vec{E}$ vector; (b) recoil frame (RF) photoelectron ejection angle θ_{RF} with respect to neutral photofragment recoil direction, θ_{RF} = 0° when photoelectron is ejected in the same direction as the heavier neutral fragment; (c) $\theta_{neutral}$, the angle between the heavy neutral photofragment recoil and ion beam propagation.

neutral products from a given DPD channel were determined by linear momentum conservation. The calibration of the photofragment detector was carried out by the DPD of O_4^- at 532 nm, showing a translational energy resolution of $\Delta E_T/E_T \sim 9\%$ at $E_T = 0.80$ eV. The photoelectron and photofragments were recorded in an event-wise fashion in coincidence, making the measurement of the RF-PAD possible.[4,5,22] Similar to the LF-PAD, the detection inhomogeneity of the photoelectron detector was considered when analyzing the RF-PAD. A two-dimensional data array was first generated, with one dimension θ_{RF}, the angle between the photoelectron and photofragment recoil directions [Figure 6-1(b)], and the other dimension θ_{LF}. The data were then symmetrized in the θ_{LF}

dimension by $\bar{N}(\theta_{LF},\theta_{RF}) = \frac{1}{2}[N(\theta_{LF},\theta_{RF}) + N(180^{\circ} - \theta_{LF},\theta_{RF})]$, followed by the summation of $\bar{N}(\theta_{LF},\theta_{RF})$ over θ_{LF} to generate a corrected $N(\theta_{RF})$ distribution. It has to be noted that this treatment assumes full and homogeneous detection for photofragments that recoil forward and backward along the parent ion beam.

6.2 Results and Discussion

Previous studies focused on the examination of the OH + CO → [HOCO]* → H + CO_2 PES by measuring the scalar correlation of photoelectron-photofragment kinetic energy partitioning in the one-photon photodetachment of $HOCO^-$ and $DOCO^-$,[11,12] as well as the alignment of the $HOCO^-$ molecular anion through a near-threshold shape resonance by analysis of the LF-PAD in the two-photon photodetachment.[20] In this section, the dynamics of the HOCO and DOCO radical will be investigated from an alternative point of view by examination of both the LF angular distributions and the angular correlations of the photoelectron and photofragments in the recoil frame (RF). The photofragment angular distribution in the two-photon photodetachment of $HOCO^-$ will also be presented, providing further evidence for the alignment of the molecular anion through a near-threshold shape resonance.

Several different types of angles used in this chapter are defined in Figure 6-1. As mentioned in the experimental section, the LF photoelectron recoil angle θ_{LF} is chosen with respect to the direction of the ion beam and the collinear laser $\vec{E}$ vector, with $\theta_{LF} = 0$ when the electron is ejected along the fast ion beam towards the photofragment detector [Figure 6-1(a)]. The RF photoelectron recoil angle θ_{RF} is defined to be zero when the

electron is ejected in the same direction as that of the larger mass of the two neutral dissociation products (CO for OH + CO and CO_2 for the H + CO_2 channel) [Figure 6-1(b)]. Similarly, the LF neutral photofragment recoil angle $\theta_{neutral} = 0$ when the heavier photofragment recoils along the ion beam propagation [Figure 6-1(c)].

6.2.1 LF- and RF-PAD in One-Photon DPD

The LF-PAD in one photon photodetachment of isotropically distributed anions can be described by the differential cross section: [23]

$$\frac{d\sigma}{d\theta_{LF}} = \frac{\sigma_{tot}}{4\pi}[1 + \beta_2 P_2(\cos\theta_{LF})], \tag{6-5}$$

where σ_{tot} is total cross section integrated over the full 4π solid angle, β_2 is the energy-dependent anisotropy parameter, and $P_2(\cos\theta_{LF})$ is the second-order Legendre polynomial in $\cos\theta_{LF}$. The β_2 value in equation (6-5) is limited between -1 and 2. *P*-wave photodetachment leads to $\beta_2 = 2$, resulting in $\frac{d\sigma}{d\theta_{LF}} \propto \cos^2\theta_{LF}$; when $\beta_2 = 0$, an isotropic LF-PAD is observed, consistent with *s*-wave photodetachment; when $\beta_2 = -1$, $\frac{d\sigma}{d\theta_{LF}}$ is proportional to $\sin^2\theta$ as a result of interfering *s*- and *d*-photoelectron partial waves.[23]

Compared with the LF-PAD, the MF-PAD can provide richer information about the photodetachment dynamics since it describes the molecular-geometry-dependent electron scattering process: [24]

$$\frac{d^2\sigma}{d\theta d\phi} = \sum_{L=0}^{L_{\max}} \sum_{M=-L}^{L} B_{L,M} Y_{L,M}(\theta,\phi), \tag{6-6}$$

where $B_{L,M}$ is the coefficient containing the radial dipole matrix element and the relative phase of the photoelectron partial wave, and $Y_{L,M}(\theta,\phi)$ are the appropriate spherical harmonics. However, the MF-PAD can only be determined from molecules fixed-in-space. In a DPD experiment on a polyatomic molecule, the only available reference axis is the recoil frame (RF) defined by the neutral photofragment recoil direction. As a result, the ϕ term in equation (6-6) is not observable and the differential cross section for the RF-PAD can be described by:[22]

$$\frac{d\sigma}{d\theta_{RF}} = \frac{\sigma_{tot}}{4\pi}[1 + \sum_{i=1}^{i_{\max}} A_i P_i(\cos\theta_{RF})], \tag{6-7}$$

in which A_i and P_i represent the i-th order anisotropy parameter and Legendre polynomials, respectively. Specifically, the A_i values with the odd i will determine the forward-backward asymmetry in the RF-PAD if there is any.[22]

Equations (6-5) and (6-7) are used to interpret the LF- and RF-PAD's obtained from one-photon photodetachment of $HOCO^-$ and $DOCO^-$ (E_{hv} = 3.21 eV) presented in Figure 6-2. The PAD's in the two frames are plotted in the form of $N(\cos\theta_{LF})$ *vs* $\cos\theta_{LF}$ and $N(\cos\theta_{RF})$ *vs* $\cos\theta_{RF}$, respectively, to avoid the zero distributions at 0º and 180º caused by the sinθ term when integrating over the solid angle. The $N(\cos\theta)$ represents the number of events within a histogram between $\cos\theta$ and $\cos\theta + \Delta(\cos\theta)$ and is integrated over the whole eKE distribution. In Figure 6-2, the number of bins is chosen to be 32 for each histogram.

The $N(\cos\theta)$ distributions in Figure 6-2 are related to the differential photodetachment cross section $\frac{d\sigma}{d\theta}$ by the following equation:

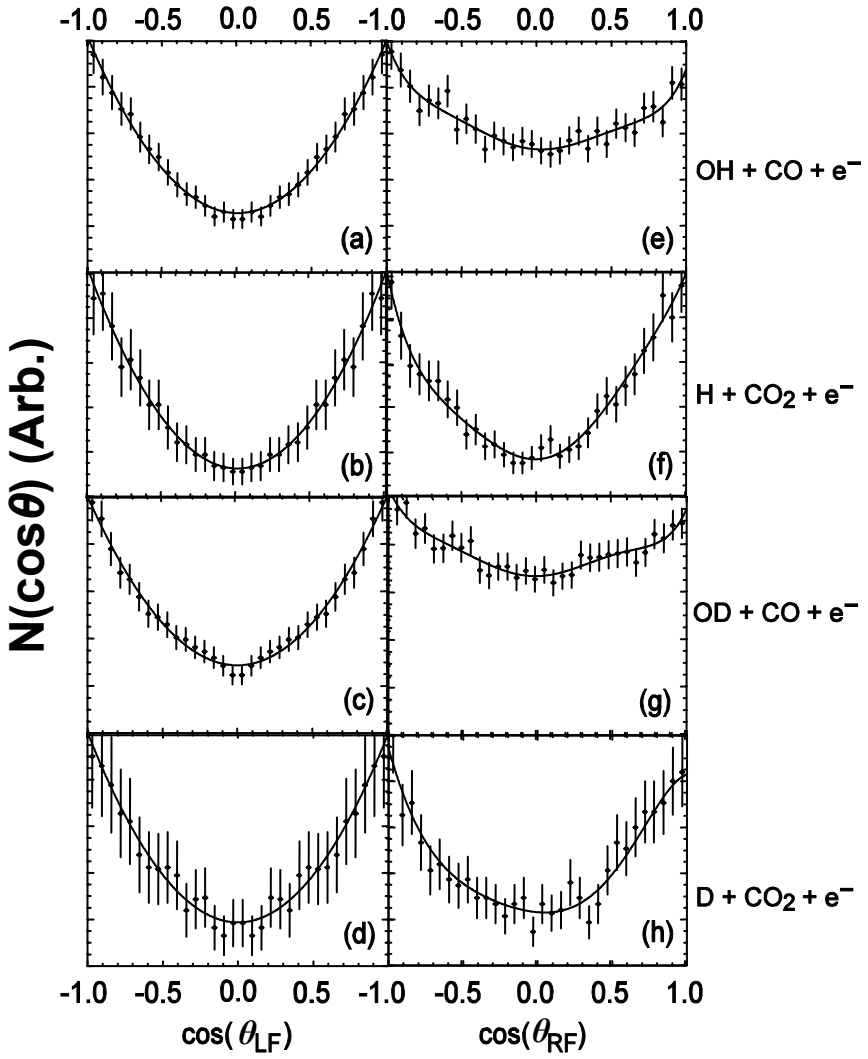

Figure 6-2: The LF- (left column) and RF-PAD (right column) of OH + CO + e^- (top row), H + CO_2 + e^- (the second row from the top), OD + CO + e^- (the third row from the top), and D + CO_2 + e^- (bottom row) from the one-photon photodetachment of $HOCO^-$ and $DOCO^-$ at E_{hv} = 3.21 eV. The scattered dots represent experimental number of events recorded within a small range of solid angles, with ± 1σ Poisson error bars. The solid lines are from fitting the experimental data using equations (6-5) and (6-8) for LF- and equations (6-7) and (6-8) for RF-PAD's.

$$N(\cos\theta) = \int_{\theta}^{\theta+\Delta\theta} \frac{d\sigma}{d\theta} \cdot \sin\theta \cdot d\theta = \int_{\cos\theta}^{\cos\theta+\Delta(\cos\theta)} \frac{d\sigma}{d\theta} d(\cos\theta) . \qquad (6\text{-}8)$$

Combining equations (6-5) and (6-8), the one-photon LF-PAD's at E_{hv} = 3.21 eV in Figure 6-2 (a) - (d) are fitted, yielding the LF photoelectron anisotropy parameter β_2 = 1.1, 1.4, 1.0 and 1.3 ± 0.1 for the DPD channels OH + CO + e^-, H + CO_2 + e^- (from the DPD of $HOCO^-$), OD + CO + e^-, and D + CO_2 + e^- (from the DPD of $DOCO^-$), respectively. The observation that $\beta_2 \geq 1.0$ for all four of the DPD channels is consistent with a dominant *p*-wave photodetachment process, causing the LF-PAD to peak parallel to the laser polarization.[23] The LF-PAD in the H/D + CO_2 + e^- channel is seen to be more anisotropic than that in the OH/OD + CO_2 + e^- channel. As the H/D + CO_2 + e^- channel corresponds to a higher eKE distribution, the observed larger β_2 value in the H/D + CO_2 + e^- channel implies a more dominant *p*-partial wave at higher eKE, consistent with the prediction of the Wigner threshold law that the larger *l*-partial waves are suppressed near the photodetachment threshold, becoming more dominant as eKE increases.[25,26] This interpretation of the superposition of *s*- and more dominant *p*-wave photodetachment above threshold agrees with the previous one-photon near-threshold photodetachment experiment of $HOCO^-$ at E_{hv} = 1.60 eV showing that zero-kinetic-energy (ZEKE) photoelectrons have a dominant *s*-wave LF-PAD.[20] As seen from the measured β_2 values, the isotopic effect in LF-PAD's is negligible with the current uncertainties, implying that the photoelectron experiences similar interactions during escape from the HOCO and DOCO neutral cores.

A prediction of the observed LF-PAD from theory requires a high-level electron-molecule scattering calculation, a challenging task for a molecular anion like $HOCO^-$. An

approximate group-theoretical treatment, limiting the continuum electron states to *s*- & *p*-waves, as presented by Sanov and coworkers is employed here to explain the observed LF-PAD qualitatively.[8]

From a symmetry perspective, a dipole-allowed photodetachment process requires the direct product of irreducible representations for the transition dipole moment and wave functions of the initial anion and final products (electron + neutral) to contain the completely symmetric irreducible representation. Previous high level *ab initio* calculations showed that both $HOCO^-$ and the ground electronic state of the HOCO free radical have A' symmetry in C_s geometry.[11,27] The direct product of the initial and final state symmetries and the transition dipole can then be described by $A'(\text{anion}) \otimes a'(\mu_{x,y}) \otimes A'(\text{radical}) \otimes \varphi_{ele}$ for the x and y components (in the plane of symmetry), and $A'(\text{anion}) \otimes a''(\mu_z) \otimes A'(\text{radical}) \otimes \varphi_{ele}$ for the z component (perpendicular to the plane of symmetry). These two direct products must contain the completely symmetric A' representation in the C_s point group. With the assumption that only *s*- and *p*-wave photodetachment is involved, it is predicted that the photoelectron wave function is isotropic (*s*-type photoelectron) or parallel to the symmetry plane (p_x, p_y-type) for the parallel dipole transition, and perpendicular to the HOCO plane (p_z-type) for the perpendicular transition. In the electric-dipole approximation, the transition dipole tends to lie along the laser electric field. As a result, the one-photon LF-PAD's for both parallel and perpendicular transitions are predicted to be parallel to the laser polarization. To determine whether the parallel or perpendicular transition occurs in the DPD of $HOCO^-$, the photoelectron-photofragment angular correlations and the LF angular distribution of neutral photofragments also have to be inspected.

Table 6-1: Anisotropy parameters for the RF-PADs from one- and two-photon DPD of $HOCO^-$ and $DOCO^-$. For OH/OD + CO + e^-, the RF-PAD anisotropy parameters are also reported as a function of the neutral photofragment recoil angles relative to the laser electric vector. The uncertainties for A_i are estimated to be ±0.1 for one-photon measurements and ±0.2 for two-photon measurements.

	$\theta_{neutral}$	A_1	A_2	A_3	A_4	A_5	A_6
One-photon, E_{hv} = 3.21 eV							
OH + CO + e^-	[0º,180 º]	-0.1	0.4	0.0	0.0	0.0	0.1
	[0º,18º] & [162º,180 º]	0.1	1.0	0.0	-0.1	-0.1	0.0
	[18º,60º] & [120º,162 º]	-0.1	0.4	0.0	0.10	0.0	0.1
	[60º,120 º]	-0.1	-0.2	0.0	0.0	0.0	0.1
OD + CO + e^-	[0º,180 º]	0.0	0.3	0.0	0.0	0.0	0.1
	[0º,25º] & [155º,180 º]	0.0	0.7	0.1	0.1	0.1	0.1
	[25º,60º] & [120º,155 º]	0.0	0.3	0.0	0.0	0.0	0.1
	[60º,120 º]	0.0	-0.3	0.0	0.0	0.1	0.0
H + CO_2 + e^-	All detected	0.3	1.4	0.2	0.2	0.2	0.2
D + CO_2 + e^-	All detected	0.2	1.1	-0.1	0.1	-0.1	0.1
Two-photon, E_{hv} = 1.60 eV							
OH + CO + e^-	[0º,180 º]	0.1	-0.1	0.0	0.4	0.0	0.0
H + CO_2 + e^-	All detected	0.5	0.2	0.3	1.4	0.1	0.1

The channel-resolved RF-PAD's produced by the one-photon photodetachment of $HOCO^-$ and $DOCO^-$ are presented by Figures 6-2 (e) – (h). Equations (6-7) and (6-8) are applied to fit the observed RF-PAD's, with $i_{max} = 6$ in equation (6-7). The resulting RF photoelectron anisotropy parameters A_i are listed in Table 6-1. It is seen that $A_2 = 0.4 \pm 0.1$ for $OH + CO + e^-$ and 0.3 ± 0.1 for $OD + CO + e^-$ channel, while the other A_i values are all equal or close to zero, showing that the RF-PAD's in this DPD channel are more isotropic compared with the corresponding LF-PAD's ($\beta_2 = 1.1$ for $OH + CO + e^-$ and 1.0 for $OD + CO + e^-$). On the other hand, the RF-PAD's in the hydrogen production channel show more significant anisotropies, with $A_2 = 1.4 \pm 0.1$ and 1.1 ± 0.1 for $H + CO_2 + e^-$ and $D + CO_2 + e^-$ channels, respectively. These two A_2 values are very close to the LF photoelectron β_2. A set of other non-zero A_i parameters are also obtained in $H/D + CO_2 + e^-$ channel as seen in Table 6-1.

6.2.2 LF Photofragment Angular Distributions

Because the neutral photofragment recoil axes are used as references in the RF-PAD, to further understand the RF-PAD's shown in Figure 6-2, the LF photofragment angular distributions obtained from the one-photon DPD of $HOCO^-/DOCO^-$ at $E_{hv} = 3.21$ eV must also be examined. Figures 6-3(a) and (b) show the OH/OD + CO LF angular distribution in a form of $N(\theta_{neutral})$ *vs.* $\theta_{neutral}$, in which $N(\theta_{neutral})$ is defined as the number of events within a small range of recoil angles from $\theta_{neutral}$ to $\theta_{neutral} + \Delta\theta_{neutral}$ and $\Delta\theta_{neutral}$ is set to be 4º here. These distributions have not been symmetrized in any way, showing that the assumption used in symmetrization of the RF-PADs is a good one.

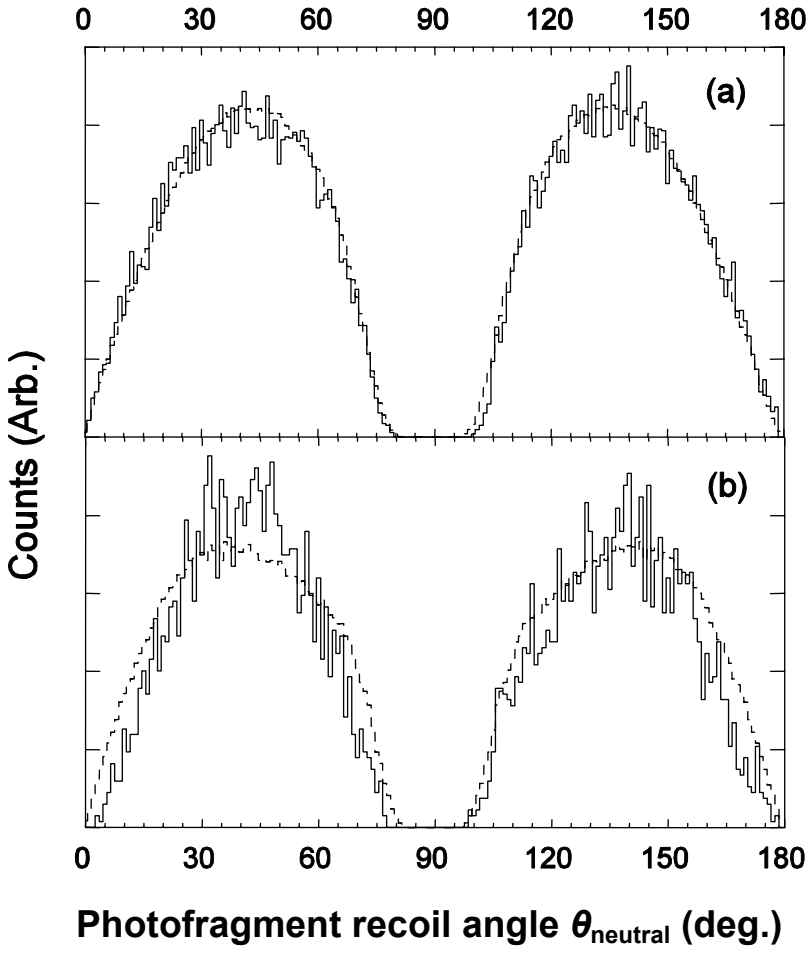

Figure 6-3: The LF photofragment angular distributions for (a) OH + CO and (b) OD + CO from the one-photon photodetachment of $HOCO^-$ and $DOCO^-$ at E_{hv} = 3.21 eV. Solid lines are experimental results. Dashed lines were obtained by the Monte Carlo simulation using equation (6-5).

The differential cross section defined by equation (6-5) is valid for the characterization of the photofragment angular distribution in LF when θ_{LF} is replaced by $\theta_{neutral}$.[28] However, the detection of neutral photofragments is more complicated than that of the photoelectrons. For example, the measurement of the two neutral dissociation products in coincidence involves consideration of the detector acceptance function

(DAF), and the detector efficiency may vary with different masses. In addition, detection of the two dissociation products is affected by the 19 ns dead time of the detector. Consequently, the experimental N($\theta_{neutral}$) curves in Figure 6-3(a) and (b) can not be simply fit by the equations (6-5) and (6-8). To faithfully model the DAF and obtain a reliable photofragment anisotropy parameter β_2, a Monte Carlo simulation incorporated with equation (6-5) was employed in the current study to reproduce the observed N($\theta_{neutral}$) distributions.[29,30] In Figure 6-3, the solid and dashed lines represent the experimental and simulated N($\theta_{neutral}$), respectively. The β_2 values of 0.8±0.1 for OH + CO and 0.6±0.1 for OD + CO are obtained, showing that the OH + CO products also recoil along the laser $\vec{E}$ vector but are more isotropic than the LF-PADs for those channels.

The observed H/D + CO_2 LF photofragment angular distributions also peak along the laser $\vec{E}$ vector and are much more anisotropic than that of the OH/OD + CO, but this is to first order a result of the very limited DAF for H/D atom detection. The kinetic energy release (KER) was found to peak around 0.5 eV for the H/D + CO_2 products at $E_{h\nu}$ = 3.21 eV.[12] Due to the large mass difference between H/D atoms and CO_2 and linear momentum conservation, only the H atoms with $\theta_{neutral} \leq$ ~17º or $\theta_{neutral} \geq$ ~161º and the D atoms with $\theta_{neutral} \leq$ ~25º or $\theta_{neutral} \geq$ ~154º can be detected, while the majority of H/D atoms recoil out of the ion beam direction and miss the photofragment detector. The Monte Carlo simulation coupled with equation (6-5) was carried out for the H/D + CO_2 products. However, the simulated angular distribution is insensitive to β_2 values ranging from -1 to 2. Therefore, the results from Monte Carlo simulations for H/D + CO_2 are not included in this chapter and no photofragment β_2 value is reported for this DPD channel.

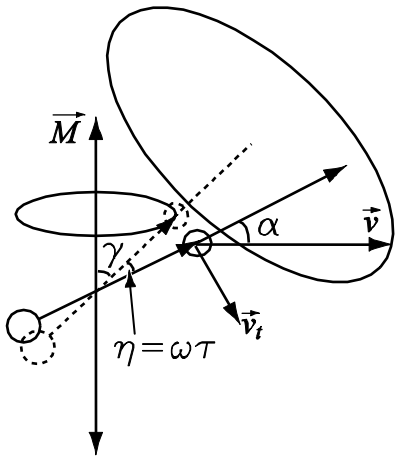

Figure 6-4: Schematic pseudodiatomic model of Busch and Wilson.[6] The included angle between the breaking bond and the transition dipole is γ. The excited molecule rotates an angle of $\eta = \omega\tau$ in the lifetime of τ. An additional deflection of the photofragment recoil direction by an angle of α is caused by the rotation in the initial state, and can be calculated by $\alpha = \sin^{-1}(v_t/v)$ where v is the photofragment recoil velocity and v_t is the tangential velocity in rotation of the initial state.

A rigorous theoretical interpretation of photofragment angular distribution requires a detailed quantum mechanical treatment, beyond the scope of current study. Instead, a classical model developed by Busch and Wilson is used to discuss the dynamics information conveyed by the observed LF angular distributions of neutral photofragment.[6] This model treats a polyatomic molecule as a pseudodiatomic case. Assuming the chemical bond breaks at a given angle γ to the transition dipole $\vec{M}$ and taking the tangential velocity v_t resulting from rotation of the parent molecule and the lifetime τ of the photoexcited state into account, the photofragment anisotropy parameter β_2 can be calculated using the equation: [6]

$$\beta_2/2 = \{[P_2(\alpha) + \eta^2 - 3\eta \sin\alpha \cos\alpha]/1 + 4\eta^2\} P_2(\cos\gamma), \quad (6\text{-}9)$$

Here $\alpha = \sin^{-1}(v_t/v)$ where v is the photofragment recoil velocity, and $\eta = \omega\tau$ where ω is the angular velocity of rotation of the photoexcited state. The definitions of the angles involved in the equations are shown in Figure 6-4.

Although first developed for photodissociation processes, equation (6-9) is also valid for the interpretation of photofragment angular distributions involved in a DPD process since the angular momentum of the photoelectron is negligible. The experimental β_2 parameters of 0.8 ± 0.1 for OH + CO and 0.6 ± 0.1 for OD + CO can be directly used in equation (6-9). To calculate the value of α, v is estimated to be 8.4×10^4 cm/sec for OH and 8.1×10^4 cm/sec for OD from the KER peak ≈ 0.1 eV in the production of OH/OD + CO.[12] The estimation of v_t is more complicated. Using the equilibrium geometry from *ab initio* calculations,[11,31] the moments of inertia of the CM of the OH/OD group in $HOCO^-/DOCO^-$ and the total moments of inertia of the anion were calculated respectively for both the *trans*- and *cis*-configurations, since the *cis*- and *trans*- isomers were indistinguishable in the parent ion beam. The fractions of the rotational energy of the CM of OH/OD over the total rotational energy of $HOCO^-/DOCO^-$ then can be estimated for all three principal axes, while the total rotational energy of the anion is taken to be ½kT for each principal axis based on the equipartition principle. A typical rotational temperature of T = 35 K in the supersonic expansion was used here because the rotational relaxation is expected to be efficient in the ion source, although vibrationally excited $HOCO^-/DOCO^-$ anions exist in the parent ion beam as discussed previously.[12] The values of v_t of OH/OD fragments were then calculated from E_{rotate} = ½m v_t^2, where

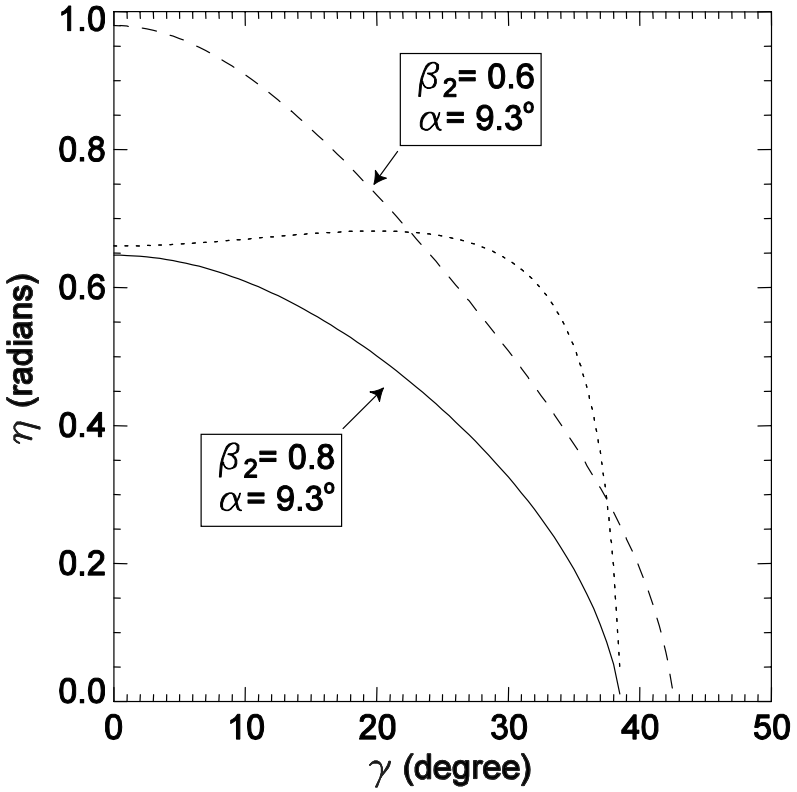

Figure 6-5: Rotation angle $\eta = \omega\tau$ as a function of γ, the angle between the breaking bond and transition dipole for OH + CO (solid line) and OD + CO (dashed line). The dotted line shows the ratio of η(OH)/η(OD) as a function of γ.

E_{rotate} is the sum of rotational energies of the CM of the OH/OD products about the three principal axes. The resulting α values are α(OH) = 9.3º in *cis*-and 9.2º in *trans*-$HOCO^-$, and α(OD) = 9.3º in *cis*-and 9.4º in *trans*-$DOCO^-$. Since the calculations presented here are only the approximations and the four obtained α values are very similar, an averaged α(OH/OD) = 9.3º was used.

With the given photofragment β_2 parameter and α angle, equation (6-9) can be used to calculate the relationship between the orientation of the transition dipole with

respect to the breaking HO-CO (DO-CO) bond and the HOCO/DOCO lifetime prior to dissociation into OH/OD + CO. The functions of η *vs.* γ for OH + CO (solid line) and OD + CO (dashed line) are plotted in Figure 6-5, showing that if the HO-CO or DO-CO bond breaks in a direction parallel to the transition dipole ($\gamma = 0^{\circ}$), the HOCO and DOCO rotate 0.7 and 1.0 radians, respectively, before dissociating into OH/OD + CO fragments. On the other hand, if the HOCO and DOCO radicals have negligible rotation before dissociation, the transition dipole is oriented at a maximum angle of ~38º to the HO-CO bond and ~42º to the DO-CO bond. As discussed above, from the LF-PAD measurement, one could not distinguish whether the dipole transition in DPD of $HOCO^-$ is parallel or perpendicular to the HOCO plane. However, based on the fact that $\gamma \leq$ ~38º, the perpendicular transition can be excluded since it requires $\gamma = 90^{\circ}$. In addition, the transition dipole can be predicted to lie within ±38º from the HO-CO bond within the HOCO plane.

Although the exact lifetime of the HOCO and DOCO radicals before dissociation into OH/OD + CO products cannot be obtained due to the uncertain γ angle, an upper limit for the lifetime for HOCO/ DOCO from $\tau = \eta/\omega$ can be estimated. An estimate for ω is once again based on the equipartition principal, $E_{rotate} = \frac{1}{2}I\omega^2 = \frac{1}{2}kT$ for each principal axis. Since an upper limit for the lifetime is desired, among the three ω values, the smallest one about the major principal axis perpendicular to the HOCO/DOCO plane, is used in this calculation. From Figure 6-5, $\eta \leq 0.7$ radians for OH + CO and 1.0 radian for OD + CO, therefore, the upper limits to the lifetime, $\tau \leq 9\times10^{-13}$ sec and 1.3×10^{-12} sec, are obtained for the HOCO and DOCO free radicals leading to OH/OD + CO formation. These upper limits are consistent with the previously reported HOCO lifetime from a

femtosecond pump-probe measurement of OH products in the photoinduced reaction of CO_2-HI van der Waals complex carried out by Wittig and coworkers although these authors estimated 50% uncertainties for their measurement,[32] but smaller than that obtained from a similar picosecond experiment conducted by Zewail and coworkers.[33]

Deuterium substitution in the HOCO radical only affects the zero point energy and vibrational and rotational energy spacing, and has no influence on the PES shape. Thus it is reasonable to assume that, on average, the OH and OD radical recoil in the same direction from CO in the molecule frame. The dotted line in Figure 6-5 represents the function of η(HOCO)/η(DOCO) *vs.* γ, indicating that HOCO has a lifetime of around 60% - 70% of that of DOCO for γ angles ranging up to ~30º. Noting that the difference of the HOCO and DOCO lifetimes originates from the β_2 parameters that differ by 0.2, this lifetime difference is likely to be smaller than that shown in Figure 6-5 owing to the uncertainty of ±0.1 for each β_2. Nevertheless, the observed deuterium effect in the lifetime may be related to the previously reported sensitivity of HOCO lifetime to different rotational or spin-orbit states in OH [($^2\Pi_{1/2}$, N) and ($^2\Pi_{3/2}$, N)] products.[32-34] Because the moment of inertia for OD is nearly the double of that for OH, the OD products in a DPD process can be more rotationally excited than OH. Therefore, the observed lifetime difference for HOCO and DOCO may correlate to the different rotational distributions in OH and OD products, consistent with the previous experiments.[32,34] A state-selective detection of OH product, such as laser induced fluorescence, coupled with the DPD experiment, would be helpful to answer this question but exceedingly difficult.

It has to be noted that the lifetime discussion here is only an estimate. Besides all the approximations mentioned above, HOCO is a polyatomic molecule that is vibrating during the dissociation. Consequently, the HO-CO bond can break at a distribution of γ angles, making equation (6-9) less suitable for the calculation of lifetime. In addition, the production of OH/OD + CO primarily results from photodetachment of vibrationally excited $HOCO^-/DOCO^-$ as discussed in the previous study.[12] So the consideration of rotational effects in the parent anion needs to be extended to excited vibrational states as well, beyond the limits of the classical model used here.

In the case of the one-photon DPD channel of H/D + CO_2 + e^- at E_{hv} = 3.21 eV, the KER peaks around 0.5 eV,[12] resulting in the recoil velocity $v = 9.7\times10^5$ cm/sec for H atom and 6.8×10^5 cm/sec for D atom, about one order of magnitude larger than those of OH/OD. Using the same procedure described above for OH/OD + CO, α = 1.4º for H atom and 1.9º for D atom are obtained. However, because the photofragment β_2 parameter was not measured for H/D + CO_2, a function of η *vs.* γ is not obtained in this DPD channel. Instead, the $\beta_2/P_2(\cos\gamma)$ is plotted as a function of η in Figure 6-6 to show how the angular distributions of H + CO_2 and OH + CO fragments can be affected by the their respective α values. The solid line in Figure 6-6 corresponds to α = 1.4º for H + CO_2, while the dashed line represents α = 1.9º for D + CO_2. To compare with the OH/OD + CO result, $\beta_2/P_2(\cos\gamma)$ *vs.* η for α = 9.3º is also plotted as the dotted line in the same figure. Figure 6-6 shows that the HOCO/DOCO radicals leading to the formation of H/D + CO_2 have larger $\beta_2/P_2(\cos\gamma)$ values than those leading to the OH/OD + CO production if they have similar average lifetimes. However, this assumption about a similar lifetime for HOCO radicals leading to OH + CO and H + CO_2 remains an open question. A crossed-

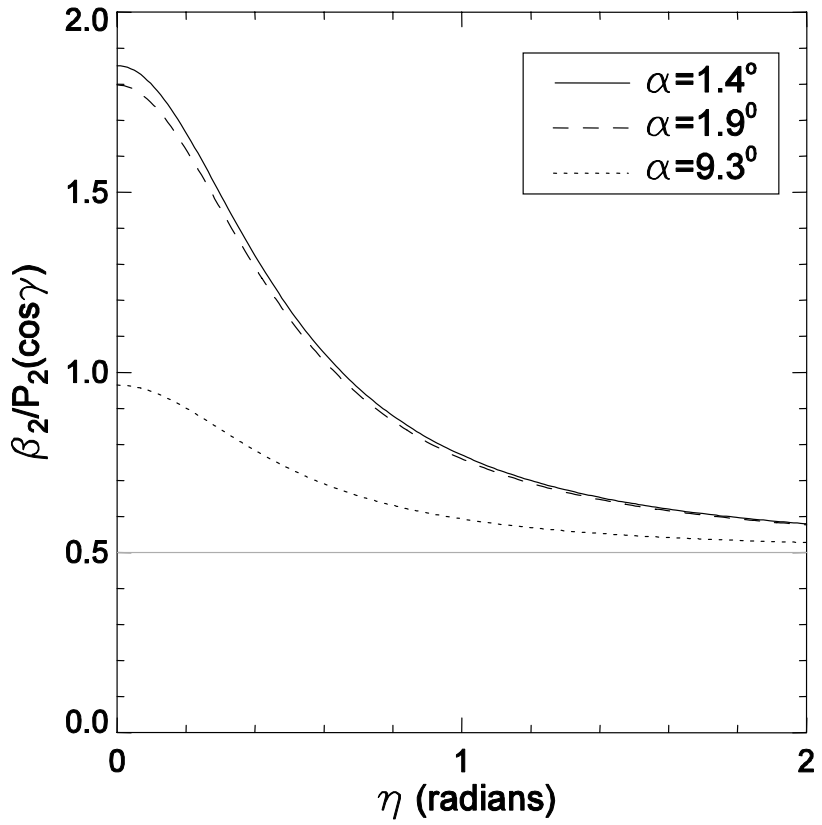

Figure 6-6: The trend of $\beta_2/P_2(\cos\gamma)$ as a function of η determined by the equation (6-6). Three α values chosen here correspond to the recoil of H + CO_2 (α = 1.4º), D + CO_2 (α = 1.9º), and OH/OD + CO (α = 9.3º), respectively.

molecular-beam experiment of OH + CO by Casavecchia and coworkers [35] yielded a consistent HOCO lifetime with the measurements from the reverse direction H + CO_2 carried out by Wittig and coworkers.[32] But it has to be pointed out that both of these experiments investigated the HOCO radical with an energy of ~0.6 eV above the OH + CO limit, and therefore significantly above the reaction barrier separating HOCO radical and H + CO_2 products when compared to the present experiments. In the current DPD experiment at E_{hv} = 3.21 eV, it has been observed that the formation of H + CO_2

fragments proceeds via two mechanisms: those HOCO radicals with energy below the transition state may tunnel through the barrier, while radicals with sufficient energy dissociate over the barrier. In the measurement of $DOCO^- + h\nu \rightarrow D + CO_2 + e^-$, on the other hand, the tunneling mechanism may be inefficient due to the heavier mass of D atom, making the unimolecular dissociation over energy barrier the dominant mechanism.[12] Therefore, it is possible that the HOCO radicals leading to $H + CO_2$ products have a longer average lifetime than those leading to OH + CO as a result of the contribution of tunneling mechanism in this channel, while the DOCO radicals leading to OD + CO and $D + CO_2$ products have similar average lifetimes.

The observed RF-PAD's in Figure 6-2 can be explained by the photofragment angular distributions discussed above. The RF-PAD's in the OH/OD + CO + e^- channel are more isotropic than the corresponding LF-PAD because the OH + CO products recoil at a relatively wide range of angles with respect to the laser $\vec{E}$ vector, as a result of the rotation during the lifetime of the HOCO/DOCO intermediate and the angle between the transition dipole and breaking HO-CO bond. The more anisotropic RF-PAD's in H/D + CO_2 + e^- channel, however, are likely to result from the small DAF of $H/D + CO_2$.

To verify this assertion, the RF-PAD of the OH/OD + CO + e^- channel with the OH/OD + CO recoil axis restricted in a range of solid angles to the laser polarization was examined, as demonstrated in Figure 6-7. The figure shows that when the OH/OD + CO recoil axis is restricted around the laser $\vec{E}$ vector [$0^o \leq \theta_{neutral} \leq 18^o$ or $162^o \leq \theta_{neutral} \leq 180^o$ for OH + CO in Figure 6-7 (a), and $0^o \leq \theta_{neutral} \leq 25^o$ or $155^o \leq \theta_{neutral} \leq 180^o$ for OD + CO in Figure 6-7(e)], a more anisotropic RF-PAD is observed to peak parallel to the

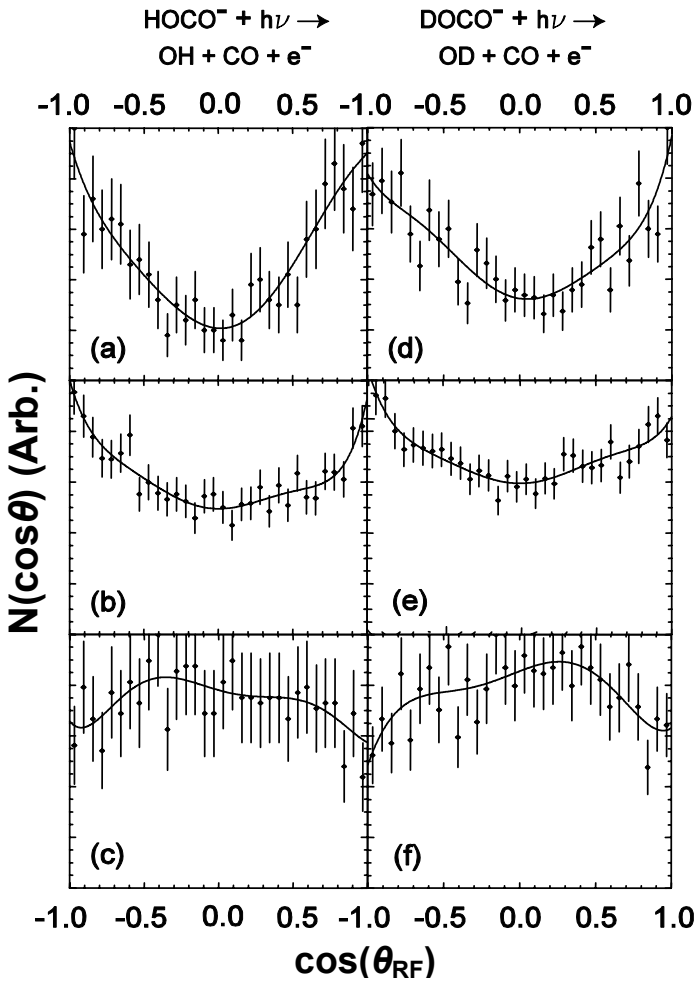

Figure 6-7: The RF-PAD in one-photon DPD channels $HOCO^- + h\nu \rightarrow OH + CO + e^-$ (left column) and $DOCO^- + h\nu \rightarrow OD + CO + e^-$ (right column) at $E_{h\nu}$ = 3.21 eV with the neutral photofragment recoil angles restricted within (a) $0^o \leq \theta_{neutral} \leq 18^o$ or $162^o \leq \theta_{neutral} \leq 180^o$; (b) $18^o \leq \theta_{neutral} \leq 60^o$ or $120^o \leq \theta_{neutral} \leq 162^o$; (d) $0^o \leq \theta_{neutral} \leq 25^o$ or $155^o \leq \theta_{neutral} \leq 180^o$; (e) $25^o \leq \theta_{neutral} \leq 60^o$ or $120^o \leq \theta_{neutral} \leq 155^o$; and (c) and (f) $60^o \leq \theta_{neutral} \leq 120^o$. The scattered dots represent experimental intensity with ± 1σ Poisson error bars. The solid lines are from fitting the experimental data using equations (6-5) and (6-8) for LF- and equations (6-7) and (6-8) for RF-PAD's.

OH/OD + CO recoil axis. Here the $\theta_{neutral}$ range is chosen to be consistent with the maximum photofragment recoil angle of 18º for H + CO_2 and 25º for D + CO_2 so that the RF-PAD's in Figure 6-7(a) and (e) can be compared with those in Figure 6-2(f) and (h). Within this $\theta_{neutral}$ range, A_2 = 1.0 ± 0.1 for OH + CO + e^-, consistent with LF photoelectron β_2 = 1.1 ± 0.1; while A_2 = 0.7 ± 0.1 for OD + CO + e^-, smaller than the corresponding LF photoelectron β_2 = 1.0 ± 0.1 and consistent with a longer lifetime for DOCO and a relatively wider angular range for photofragment recoil [0º − 25º compared with 0º − 18º chosen for OH + CO in Figure 6-7(a)]. When the OH/OD + CO recoil axis is limited to be perpendicular to the laser electric field [60º ≤ $\theta_{neutral}$ ≤ 120º, as in Figure 6-7(c) and (g)], A_2 becomes slightly negative and the RF-PAD's are more isotropic. When the OH/OD + CO recoil axis is limited in a ranged between these two extremes [18º ≤ $\theta_{neutral}$ ≤ 60º or 120º ≤ $\theta_{neutral}$ ≤ 162º for OH + CO in Figures 6-7 (b), and 25º ≤ $\theta_{neutral}$ ≤ 60º or 120º ≤ $\theta_{neutral}$ ≤ 155º for OD + CO in Figure 6-7(f)], the observed RF-PAD's are very similar with those without the limitation of OH/OD + CO recoil axis shown in Figure 6-2(e) and (g). The anisotropy parameters obtained by fitting each of the RF-PAD's in Figure 6-7 are included in Table 6-1, showing the significant dependence of RF-PAD on the photofragment recoil direction.

6.2.3 Angular Correlations in Two-Photon DPD

The photoelectron-photofragment correlations have also been investigated for two-photon photodetachment of $HOCO^-$ at E_{hv} = 1.60 eV. Our previous study has shown a co-existence of parallel and perpendicular LF-PADs in this two-photon process, interpreted to result from interfering *s*- and *d*-photoelectron partial waves mediated by a

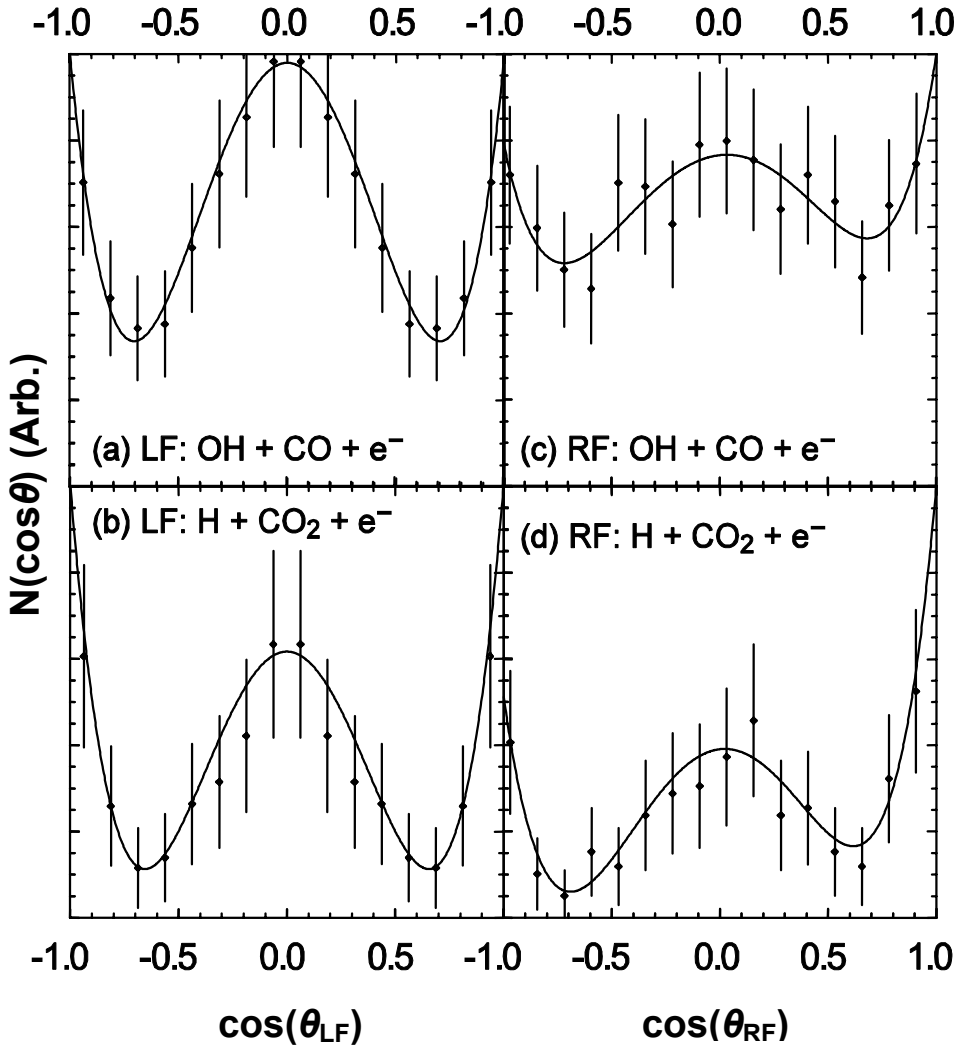

Figure 6-8: The LF- (left column) and RF-PAD (right column) of (a) and (c) $HOCO^- + h\nu \rightarrow OH + CO + e^-$, and (b) and (d) $HOCO^- + h\nu \rightarrow H + CO_2 + e^-$ at $E_{h\nu}$ = 1.60 eV. The scattered dots represent experimental intensity, with ± 1σ Poisson error bars. The solid lines are from fitting the experimental data using equations (6-8) and (6-10) for LF- and equations (6-4) and (6-5) for RF-PAD's.

near-threshold *p*-type shape resonance.[20] Figure 6-8 compares the channel-resolved LF- and RF-PAD's from the two-photon DPD processes. Equation (6-5) used for the LF-PAD

in one-photon photodetachment is not suitable for a two-photon process, a fourth-order Legendre polynomial and its corresponding anisotropy parameter must be included in the differential cross section: [36]

$$\frac{d\sigma}{d\theta_{LF}} = \frac{\sigma_{tot}}{4\pi}[1 + \beta_2 P_2(\cos\theta_{LF}) + \beta_4 P_4(\cos\theta_{LF})]. \quad (6\text{-}10)$$

Using equations (6-8) and (6-10), the LF photoelectron anisotropy parameters β_2 = -0.4 ± 0.2 and β_4 = 0.9 ± 0.2 are obtained for the OH + CO + e^- channel integrated over all eKE, indicating that the perpendicular component is more dominant. On the contrary, in the H + CO_2 + e^- channel, β_2 = 0.0 ± 0.2 and β_4 = 1.6 ± 0.2, corresponding to a more parallel component. The observed difference in the LF-PAD of these two DPD channels can simply be explained by the eKE-dependence of *s*- and *d*-photoelectron partial wave interference. The OH + CO + e^- channel yields a lower-eKE distribution than the H + CO_2 + e^- channel, and therefore corresponds to a more dominant *s*-wave component in the interference and consequently a more perpendicular feature in the LF-PAD. [20]

The RF anisotropy parameter A_i values are also obtained for these two DPD processes and listed in Table 6-1. Similar to the one-photon measurement, the RF-PAD in the OH + CO + e^- channel is more isotropic than the corresponding LF-PAD as A_2 = -0.1 ± 0.2 and A_4 = 0.4 ± 0.2, consistent with an relatively isotropic angular distribution of OH + CO recoil direction; while the RF-PAD in the H + CO_2 + e^- shows a significant anisotropy with A_2 = 0.2 ± 0.2 and A_4 = 1.4 ± 0.2, in agreement with the small solid angle of H + CO_2 products being detected.

Our previous study suggested that this strong two-photon absorption was mediated by a *p*-type shape resonance near the photodetachment threshold, leading to a

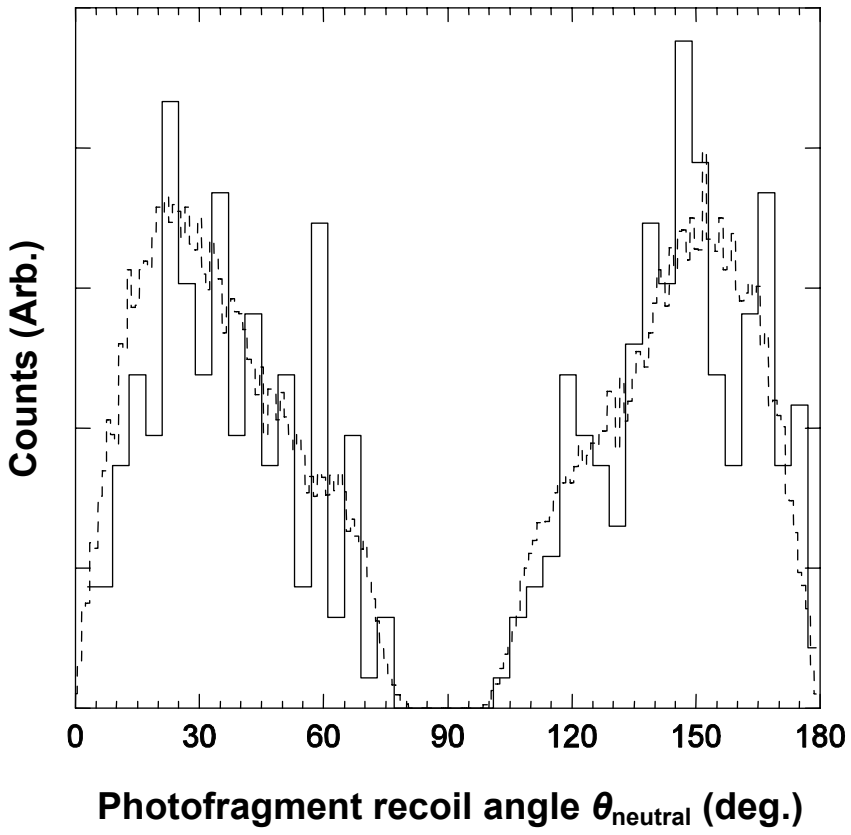

Figure 6-9: The LF photofragment angular distributions of OH + CO from the two-photon photodetachment of $HOCO^-$ at $E_{h\nu}$ = 1.60 eV. Solid lines are from experimental measurements. Dashed lines represent the Monte Carlo simulation results using equation (6-10).

significant alignment of the transient $HOCO^-$ produced by absorption of the first photon. In such a process, the low-energy *p*-partial wave outgoing electrons are temporarily trapped by a centrifugal barrier, forming a shape resonance that selects $HOCO^-$ aligned parallel with laser polarization (consistent with the parallel transition dipole discussed above). The LF angular distribution of the neutral photofragments in the two-photon DPD provides the further evidence for this phenomenon. Figure 6-9 shows the $N(\theta_{neutral})$

vs. $\theta_{neutral}$ in the LF for OH + CO obtained from the two-photon DPD of $HOCO^-$ at E_{hv} = 1.60 eV. A Monte Carlo simulation with the employment of equation (6-10) is used to fit the experimental data, showing the LF anisotropy parameters β_2 = 1.3 ± 0.2 and β_4 = 0.3 ± 0.2. Compared with Figure 6-3, the LF angular distribution of OH + CO in the two-photon process is evidently more anisotropic along the laser polarization, supported by a larger β_2 (1.3 ± 0.2 in two-photon process compared with 0.8 ± 0.1 in one-photon process) and the emergence of a positive β_4. This observation provides solid evidence for the alignment of $HOCO^-$ along the laser $\vec{E}$ vector during the two-photon photodetachment as inferred from the LF-PADs presented in Ref. 20.

6.4 Conclusion

In summary, the dynamics of the one- (E_{hv} = 3.21 eV) and two-photon (E_{hv} = 1.60 eV) DPD processes, $HOCO^- + h\nu \rightarrow OH + CO + e^-$ and $HOCO^- + h\nu \rightarrow H + CO_2 + e^-$, have been studied by a measurement of the photoelectron and photofragment energy and angular distributions in coincidence. Examination of the angular correlations among the photoelectron, photofragments, and the laser polarization reveals that the DPD of $HOCO^-$ is characterized by a transition dipole in the HOCO symmetry plane. Anisotropy parameters for the LF- and RF-PAD, as well as for the LF photofragment angular distribution of the OH + CO products, are reported. With these parameters, the relationship between the HOCO/DOCO lifetime and orientation of transition dipole has been investigated using a classical model. The upper limits of lifetime are reported to be 9×10^{-13} and 1.3×10^{-12} sec for HOCO and DOCO radicals, respectively, and have been compared with several previous measurements. In addition, the angular distribution

measurement in the two-photon DPD of $HOCO^-$ at E_{hv} = 1.60 eV supports the results of our previous study that the alignment of a molecular anion can be realized through a shape resonance near the photodetachment threshold. Future work employing a higher beam energy (up to 16 keV) to improve the DAF for H/D atoms, as well as measuring the H + CO_2 product angular distribution as a function of different laser polarizations, may help extract a reliable anisotropy parameter for H + CO_2 fragments and yield further insights into the HOCO lifetime and DPD dynamics. In addition, detailed electron-molecule scattering dynamics information is not obtained from the current RF-PAD measurement, due to the HOCO lifetime and the relatively isotropic distribution of photofragment recoil axes. One approach to this problem is to further study the two-photon DPD process using pump and probe lasers with different polarization geometries or a two-color scheme, allowing extraction of the photoelectron anisotropy parameters A_i in a frame with the molecular transition dipole spatially aligned along the pump laser polarization.[20] These experimental results accompanied by further quantum dynamics calculations should clarify in greater detail the role of the HOCO intermediate on the complicated potential energy surface that governs the fundamental OH + CO → H + CO_2 reaction.

References

1 R. E. Continetti, Annu. Rev. Phys. Chem. **52**, 165 (2001).

2 D. M. Neumark, Phys. Chem. Chem. Phys. **7**, 433 (2005).

3 R. E. Continetti, Int. Rev. Phys. Chem. **17**, 227 (1998).

[4] K. A. Hanold, M. C. Garner, and R. E. Continetti, Phys. Rev. Lett. **77**, 3335 (1996).

[5] K. A. Hanold and R. E. Continetti, Chem. Phys. **239**, 493 (1998).

[6] G. E. Busch and K. R. Wilson, J. Chem. Phys. **56**, 3638 (1972).

[7] K. L. Reid, Annu. Rev. Phys. Chem. **54**, 397 (2003).

[8] E. Surber, R. Mabbs, and A. Sanov, J. Phys. Chem. A **107**, 8215 (2003).

[9] M. S. Bowen and R. E. Continetti, J. Phys. Chem. A **108**, 7827 (2004).

[10] A. M. D. Lee, Ph.D. Thesis, Queen's University, 2007.

[11] T. G. Clements, R. E. Continetti, and J. S. Francisco, J. Chem. Phys. **117**, 6478 (2002).

[12] Z. Lu, Q. Hu, J. E. Oakman, and R. E. Continetti, J. Chem. Phys. **126**, 194305 (2007).

[13] J. A. Miller, R. J. Kee, and C. K. Westbrook, Annu. Rev. Phys. Chem. **41**, 345 (1990).

[14] T. Rockmann, C. A. M. Brenninkmeijer, G. Saueressig, P. Bergamaschi, J. N. Crowley, H. Fischer, and P. J. Crutzen, Science **281**, 544 (1998).

[15] I. W. M. Smith, Chem. Phys. Lett. **49**, 112 (1977).

[16] H. G. Yu, J. T. Muckerman, and T. J. Sears, Chem. Phys. Lett. **349**, 547 (2001).

[17] M. J. Lakin, D. Troya, G. C. Schatz, and L. B. Harding, J. Chem. Phys. **119**, 5848 (2003).

[18] X. L. Song, J. C. Li, H. Hou, and B. S. Wang, J. Chem. Phys. **125**, 094301 (2006).

[19] S. Zhang, D. M. Medvedev, E. M. Goldfield, and S. K. Gray, J. Chem. Phys. **125**, 164321 (2006).

[20] Z. Lu and R. E. Continetti, Phys. Rev. Lett., In press (2007).

[21] J. A. Davies, J. E. LeClaire, R. E. Continetti, and C. C. Hayden, J. Chem. Phys. **111**, 1 (1999).

[22] J. A. Davies, R. E. Continetti, D. W. Chandler, and C. C. Hayden, Phys. Rev. Lett. **84**, 5983 (2000).

[23] J. Cooper and R. N. Zare, J. Chem. Phys. **48**, 942 (1968).

[24] D. Dill, J. Chem. Phys. **65**, 1130 (1976).

[25] E. P. Wigner, Phys. Rev. **73**, 1002 (1948).

[26] K. J. Reed, A. H. Zimmerman, H. C. Andersen, and J. I. Brauman, J. Chem. Phys. **64**, 1368 (1976).

[27] Y. M. Li and J. S. Francisco, J. Chem. Phys. **113**, 7963 (2000).

[28] R. N. Zare, Mol. Photochem. **4**, 1 (1972).

[29] R. E. Continetti, D. R. Cyr, D. L. Osborn, D. J. Leahy, and D. M. Neumark, J. Chem. Phys. **99**, 2616 (1993).

[30] T. G. Clements, Ph.D. Thesis, University of California, San Diego, 2002.

[31] L. B. Harding, unpublished data.

[32] S. I. Ionov, G. A. Brucker, C. Jaques, L. Valachovic, and C. Wittig, J. Chem. Phys. **97**, 9486 (1992).

[33] N. F. Scherer, C. Sipes, R. B. Bernstein, and A. H. Zewail, J. Chem. Phys. **92**, 5239 (1990).

[34] M. Brouard, D. W. Hughes, K. S. Kalogerakis, and J. P. Simons, J. Chem. Phys. **112**, 4557 (2000).

[35] M. Alagia, N. Balucani, P. Casavecchia, D. Stranges, and G. G. Volpi, J. Chem. Phys. **98**, 8341 (1993).

[36] J. Cooper and R. N. Zare, in *Lectures in Theoretical Physics* (Gordon and Breach, Inc., New York, 1969), Vol. XI, pp. 317.